

GEOLOGICA ULTRAIECTINA

Mededelingen van de
Faculteit Aardwetenschappen
Universiteit Utrecht

No. 151

**DISTINCT BODY WAVE PHENOMENA
CAUSED BY MANTLE STRUCTURE**

Detection, observations and interpretations

Martin Schimmel

GEOLOGICA ULTRAIECTINA

Mededelingen van de
Faculteit Aardwetenschappen
Universiteit Utrecht

No. 151

**DISTINCT BODY WAVE PHENOMENA
CAUSED BY MANTLE STRUCTURE**

Detection, observations and interpretations

Martin Schimmel

Promotor: Prof. Dr R.K. Snieder

Co-promotor: Dr J.A.M. Paulssen

Members of the dissertation committee:

Prof. Dr D. Gubbins: Department of Geophysics,
University of Leeds, Leeds, England.

Prof. Dr B.H.W.S. de Jong: Department of Geology,
Utrecht University, Utrecht, Netherlands.

Prof. Dr J.C. Mondt: Department of Geophysics,
Utrecht University, Utrecht, Netherlands.
Shell Training Centre "Leeuwenhorst",
Noordwijkerhout, Netherlands.

Prof. Dr N.J. Vlaar: Department of Geophysics,
Utrecht University, Utrecht, Netherlands.

Dr W. Zürn: Black Forest Observatory Schiltach (BFO),
Karlsruhe University and Stuttgart University,
Wolfach, Germany.

ISBN 90-5744-009-1

DISTINCT BODY WAVE PHENOMENA CAUSED BY MANTLE STRUCTURE

Detection, Observations and Interpretations

Bepaalde ruimtegolf fenomenen
veroorzaakt door mantel structuur
Detectie, observaties en interpretaties

(met een samenvatting in het Nederlands)

PROEFSCHRIFT

TER VERKRIJGING VAN DE GRAAD VAN DOCTOR
AAN DE UNIVERSITEIT UTRECHT
OP GEZAG VAN DE RECTOR MAGNIFICUS, PROF. DR. J.A. VAN GINKEL
INGEVOLGE HET BESLUIT VAN HET COLLEGE VAN DEKANEN
IN HET OPENBAAR TE VERDEDIGEN
OP MAANDAG 9 JUNI 1997 DES NAMIDDAGS TE 12.45 UUR

DOOR

MARTIN HEINZ SALVADOR SCHIMMEL

Geboren op 5 september 1966 te Hannover

PROMOTOR: PROF. DR R.K. SNIEDER

CO-PROMOTOR: DR J.A.M. PAULSEN

The research described in this thesis has been carried out at the Department of Geophysics, Utrecht University, Budapestlaan 4, PO Box 80.021, 3508 TA Utrecht, The Netherlands. This is Geodynamics Research Institute (Utrecht University) contribution 97.004.

*No sempre és cert
que allí on acaba el mar
comença el vent,
que allí on acaba el vent
comença el bosc
hi ha un pou profund ...*

Miquel Martí i Pol (1929), Crónica de demá.

A mis padres e namorada

Contents

1	General Introduction	1
2	Steeply Reflected and Focused ScSH Precursors From the D” Region	7
2.1	Introduction	8
2.2	Data and Observations	9
2.2.1	Coherent ScS, sScS, and ScSScS Precursors	14
2.2.2	Stacks and Slowness Determination	16
2.2.3	SdS/ScSH Amplitude Ratio	18
2.3	Synthetic Modeling	19
2.3.1	The Method	19
2.3.2	The Results	21
2.4	Discussion	25
2.5	Conclusions	27
3	Noise Reduction and Detection of Weak, Coherent Signals Through Phase Weighted Stacks	29
3.1	Introduction and Motivation	30
3.2	Method	31
3.2.1	Analytic Signal and Phase Stacks	31
3.2.2	Phase Weighted Stacks	33
3.3	Application to Synthetic Data	34
3.3.1	Phase Weighted Stack Versus Linear Stack	34
3.3.2	Phase Stack Versus Other Coherency Measures	36
3.3.3	Phase Weighted Stack Versus N-th Root Stack	38
3.4	Application to Real Data	39
3.4.1	Phase Stack Versus Linear Stack	39
3.4.2	Phase Stack Versus Other Coherency Measures	41
3.4.3	Phase Weighted Stack Versus N-th Root Stack	42
3.5	Another Application: Detection of Weak P840s Phases	43
3.6	Discussion and Conclusions	46

4	Asymmetrically Reflected PP and SS Precursors: 1. Observations	47
4.1	Introduction	48
4.2	Data and Observations	50
4.2.1	Data Acquisition	50
4.2.2	PP Precursors	50
4.2.3	SS Precursors	56
4.3	Constraints on Precursor Generation	60
4.3.1	Precursor Generation and Terminology	60
4.3.2	Travel Time and Slowness	61
4.4	Discussion	62
4.5	Conclusions	64
5	Asymmetrically Reflected PP and SS Precursors: 2. A Mechanism to Generate Non-Stationary Arrivals	67
5.1	Introduction	68
5.2	Theory and Explanation	69
5.2.1	Stationary and Non-Stationary Arrivals	70
5.2.2	Travel Time Tripletions	72
5.2.3	Amplitude Functions for PP and SS Type Arrivals in a Spher- ically Symmetrical Earth	74
5.2.4	Synthetic Modeling of Stationary and Non-Stationary Arrivals	79
5.3	Discussion	81
5.3.1	Frequency-Dependent Amplitude Functions and Omitted Re- flections	81
5.3.2	Amplitudes of B- and C-Point Phases	82
5.3.3	Influence of Heterogeneities	82
5.3.4	760-km Discontinuity?	83
5.4	Conclusions	84
	Appendix: Kirchhoff-Helmholtz Reflection Seismograms and Choice of Integration Surface	85
	References	88
	Summary in English	94
	Summary in Dutch (Samenvatting in het Nederlands)	96
	Acknowledgements	98
	Curriculum Vitae	101

Chapter 1

General Introduction

Our knowledge on Earth structure is primarily based on the study of seismic wave propagation and the interpretation of different phases in seismograms. From the beginning of the 20th-century seismological research has revealed that the Earth gross structure is radially symmetric with several transitions which separate regions of different seismic properties. These transitions, say, discontinuities in seismic properties can be related to physical phase and/or compositional changes. The strongest discontinuities divide the Earth into inner and outer core, mantle and crust. The mantle occupies 82% of the total volume of the Earth while crust and core cover 2% and 16%, respectively. Especially in the last decades the increasing amount of better quality recordings of seismic motion, the growing power of computer systems, and advances in computational theories enabled the detection of lateral variations in the deep structure of the Earth. These lateral heterogeneities are signs of the dynamics of the Earth (e.g. *Montagner*, 1994) and caused by the slow cooling of the Earth. In the mantle the heat transfer occurs by convection with velocities of about few centimeters per year. Thus the observed seismic features in the mantle represent a snapshot of the evolution of the Earth and contain information about flow patterns, temperature anomalies, composition, and other phenomena. The mapping of the seismic features of the Earth occurs not without ambiguities and one of the main concerns in seismology is to increase the constraints and resolution of the Earth's structure. This thesis partly aims to find additional constraints on the structure of the Earth's mantle by advancing our understanding of non-routinely used parts of seismic recordings.

The just mentioned ambiguities mainly arise due to the irregular distribution of earthquakes, the discrete and irregularly spatial sampling of the wave field by a sparse number of seismic stations, and the complex physics of seismic wave propagation through the Earth. Due to the discrete spatial sampling of the wave field different waveform reconstructions

of the identified phases may satisfy the data and lead to uncertainties in the structural interpretations (*Wielandt, 1993*). Especially the identification and interpretation of weak phases are hampered by missing spatial coherency inherent to a sparse sampling of the wave field. As a result large parts of the seismic recordings remain unexplained and are unused for further interpretations. The study of wave propagation through assumed Earth models helps to understand the observed features in seismograms. But the modeling of seismic wave propagation through the assumed Earth models is realizable only with many simplifications. Inherent to all this, the mapped seismic features in Earth depend on the understanding of the physics and approximations which we think describe the nature of what we believe to see in the seismograms. The uncertainties can not be solved by direct inspection of the deep Earth, the deepest drilled hole reaches only about 0.17% of the Earth's radius. However, robust features can show up by comparing the results of many different approaches of global and regional studies. A case in point are surface wave studies which map heterogeneities based on overtone summation and measurements (*Nolet, 1990; Woodhouse et al., 1996*), polarization measurements (*Laske and Masters, 1996*) or scattering (*Snieder, 1996*). Results based on all these approaches are expected to merge to one model of the Earth.

Surface wave analysis and body wave travel time tomography are the prime tools to determine the long and intermediate scale structures of the Earth's crust and mantle. However, they lack the resolving power to constrain mantle discontinuities in terms of thickness, topography and impedance contrast. The study of reflected/converted body waves becomes important and complements the tomography type of studies. This thesis presents research which is related to these mostly tiny features in the seismograms. It aims to advance the understanding of non-standard mantle phases, the wave phenomena behind them and their constraints on Earth structure. The observations used are based on broad frequency band seismograms. The importance of using broad band data to constrain structure has been shown by *Paulssen [1987, 1988]*.

The study of mantle discontinuities is important to discriminate between the different types of convection (e.g. layered or not layered) and compositional models of the Earth. Some insight into the mantle composition has been gained from studies of meteorites, from upper mantle rocks which are exposed at the Earth's surface in some mountain belts, and from high pressure and temperature experiments on rocks. The seismological studies show that the mantle contains two global depth intervals which are characterized by anomalous seismic properties. These are the D" layer at the base of the mantle and the transition zone between upper and lower mantle at 410 km to 660 km depth. The D" layer is about 200 km - 300 km thick and is a thermal and chemical boundary layer above the core-mantle boundary at about 2890 km depth. It is known as a highly heterogeneous region with expected horizontal scale lengths ranging from 10 km - 10,000 km (*Lay, 1989; Loper and Lay, 1995*).

The small scale lengths are inferred to explain observations of high frequency, scattered body waves which travel through the core (e.g. *Doornbos and Vlaar, 1973; Bataille et al., 1990* as review) and the long scale length heterogeneities result from tomography type of studies (e.g. *Dziewonski, 1984; Wysession et al., 1994*). The core-mantle boundary and the Earth's surface are the two largest discontinuities in Earth and cause the D" region and lithosphere as their boundary layers. This and the continental sized heterogeneities and small scale features of the D" layer cause *Wysession [1996]* to speak in analogy to the continents at the Earth's surface of "continents of the core".

The understanding of this core-mantle boundary layer is crucial since this layer controls the heat transfer from the core into the mantle. This affects for example the magnetic field (*Gubbins, 1991*) and is one of the basic constraints on mantle dynamics. An increasing amount of seismological observations show evidence of subducted lithosphere which penetrates into the lower and lowermost mantle (e.g. *Creager and Jordan, 1986; Van der Hilst et al., 1991; Scherbaum et al., 1997*). And it is suggested that the D" region acts as a grave-yard of these slabs and possibly also as the source of mantle plumes (*Stacey and Loper, 1983*). Furthermore the D" layer is expected to be anisotropic (e.g. *Doornbos et al., 1986; Kendall and Silver, 1996*) which means that the seismic properties differ in the different directions of wave propagation. It is not yet clear whether this is a result of layering and/or mineralogical asymmetry. If the origin is mineralogical then a phase transformation of SiO₂ to a high-pressure phase (*Kingma et al., 1995*) could cause anisotropy and a world-wide discontinuity in the D" region. This may change in the presence of lateral variations in composition, thus the study of discontinuities in the D" could solve this problem. For example, *Weber [1993]* studied waves which reflect from a discontinuity in the D", but he also reports regions where he does not observe reflections. This could be explained by a spatially limited reflector or alternatively by heterogeneities or topography of a world-wide discontinuity which focuses or defocuses the wave field. It is suggested that this discontinuity could be a world-wide feature (*Nataf and Houard, 1993*), but more observations are required to establish this.

Up to now discontinuities in the D" region have been inferred from waves which sample the base of the lower mantle at grazing and near-grazing incidence. The wide angle reflections, however, are very sensitive to the velocity structure above (and below) the discontinuity which results in a trade-off in velocity and discontinuity depth. Chapter 2 of this thesis gives evidence for a seismic phase which is steeply reflected from a discontinuity in the D" layer. Such phases are better suited to investigate discontinuity depth and topography, however, they are more difficult to observe. Due to the earthquake distribution and small epicentral distances they can only be observed in a small area of the Earth. In chapter 2 we show the observations and explain why we can reject other possible interpretations. We can explain the frequency dependence, amplitudes, waveforms, intermittency and travel time of these arrivals by large scale length topography. This is established by three-dimensional synthetic modeling. It is further shown that focusing and defocusing cause intermittently

observed arrivals, even if the corresponding rays have neighboring bounce points with overlapping Fresnel zones.

The results from chapter 2 propose a depressed D" discontinuity underneath the Kermadec-Tonga region. In this region the oceanic crust and lithosphere subducts into the mantle (e.g. *Van der Hilst*, 1995; *Gubbins*, 1996) and the paper by *Van der Hilst* [1995] shows that slabs are penetrating into the lower mantle. If this manifests downflow of cold mantle material to the core-mantle boundary then its correlation with the depression suggests that the discontinuity in this region is not caused by a dense thermo-chemical boundary layer (*Olbertz and Hansen*, 1993). One might speculate that an endothermic phase transition or lateral variations in the composition could explain the observed depression underneath the Kermadec-Tonga region.

The other anomalous region is the upper mantle transition zone which is characterized by at least two world wide discontinuities at about 410 km and 660 km depth and an increased velocity gradient between both discontinuities. A 520-km discontinuity is less often observed. Pressures and temperatures in the transition zone increase from about 13-14 GPa and $1750\text{ K} \pm 100\text{ K}$ at 410 km depth to about 23-24 GPa and $1950\text{ K} \pm 100\text{ K}$ at 660 km depth (*Ranalli*, 1996). The discontinuities at these pressures and temperatures are expected to be mainly caused by phase changes of the most abundant mineral components in the mantle, such as olivine and pyroxene, to more closely-packed structures. However, it can not be ruled out that besides these isochemical transformations also compositional stratification occurs and these contributions together explain the fine structure of the transition zone. This fine structure gives rise to many observable but variable and mostly weak features in seismograms. A case in point are the bottom - and top-side reflected or converted phases from the discontinuities. The seismograms contain many different arrivals with similar amplitudes and consequently these phases can only be detected by their coherent appearance on different traces. In practice it is often difficult to identify these signals on the seismograms and to associate them uniquely with a particular arrival. Stacking methods are a common tool used to overcome these difficulties by reducing incoherent noise. However, the detection of weak and coherent signals is hampered by the fact that incoherent large amplitude signal can lead to large amplitude features in the stacks and cause ambiguous phase detection. This motivates a new coherency measure and stacking technique which are proposed in chapter 3. Complex trace analysis is used to design two simple tools which can easily be extended to different applications. In contrast to many other coherency measures the measure presented here is amplitude unbiased and used to clean stacks from incoherent noise. Its benefits are exemplified by applying it on synthetic and real data. Examples of real data show upper mantle phases which are detected by their coherency. Some of which were not detected in the linear stacks. This technique may contribute to a more unambiguous detection of seismic arrivals such as weak mantle phases and advance our understanding and interpretation of the small features in the seismograms.

Most progress in constraining the upper mantle structure, however, can be gained by increasing the density of seismic stations (*Nolet et al.*, 1994). The denser sampling of the seismic wave field would decrease the patchiness of data coverage and also permit to better understand the intermittency of upper mantle reflections/conversions, i.e. seismic visibility of discontinuities. The seismic visibility of the discontinuities depends on frequency (*Richards*, 1972) and is the reason why broad band waveform studies are important. *Paulssen* [1988] uses waveform similarities of converted and unconverted arrivals over a broad frequency range to give first unambiguous evidence for a at least locally sharp 660-km discontinuity. The 410-km discontinuity is more intermittently observed than the 660-km discontinuity and can also be sharp (e.g. *Benz and Vidale*, 1993; *Neele*, 1996). The thickness of these discontinuities could range between 4 - 15 km. The uncertainties arise due to the trade-off between thickness and transition profile of seismic properties within the considered frequency range (*Helfrich and Wood*, 1996). The variable seismic visibility of these discontinuities can be explained by topography and varying thickness as response to temperature variations in the mantle (e.g. *Neele and Snieder*, 1992; *Van der Lee et al.*, 1994; *Bina and Helfrich*, 1994; *Helfrich and Bina*, 1994) and further constrain the type of transformation.

These discontinuities affect the seismic wave field not only in terms of reflections and conversions but also cause the wave field to focus an increased amount of energy within certain epicentral distance ranges. This happens within the so called triplication zone. The wave field which turns above the discontinuity, below the discontinuity, and which is critically reflected can arrive within the same epicentral distance range due to the discontinuity and the medium properties around it. This leads to large amplitude waves, specially at the begin and end point of triplications where one of the turning waves arrives at the same time with a reflected wave. This phenomenon causes amplitude fluctuations in the wave field without the presence of lateral heterogeneities. In chapter 4 we show and discuss the observation of seismic arrivals which are related to these amplitude fluctuations. The observations are from epicentral distances which are 4 to 5 times larger than the distances to the regions where these arrivals are generated by amplitude fluctuations of the wave field at the Earth's surface. Therefore these arrivals are also called asymmetrically reflected phases. We observe such phases for compressional waves (*P*-waves) and shear waves (*S*-waves). They appear as precursors to the so-called *PP* and *SS* arrivals which reflect at the Earth's surface midway between source and receiver. Asymmetrically reflected arrivals have been observed previously for *P*-waves and were explained differently. The new observations from chapter 4 rule out that the existing generation mechanisms explain the observations and this motivates to find an alternative scenario. Chapter 5 proposes an mechanism due to the amplitude fluctuations caused by the upper mantle discontinuities. The principles of the mechanism are explained using Huygens' principle which asserts that points which are disturbed by an incoming wave act as a new set of radiating sources which generate

new waves and which interfere to a new wave. It is shown that these asymmetrically reflected phases are non-geometrical arrivals which resemble edge or point diffractions. Our considerations show that these non-geometrical phases may occur in a radially symmetric Earth, i.e. without the presence of lateral heterogeneities. However, our approach, based on high-frequency approximations and the omission of reflected and head waves, does not permit the conclusion that the observed amplitudes of these non-geometrical arrivals are indeed explained by a one-dimensional structure alone. Heterogeneities can strengthen or weaken the generation, however, without changing the idea of the proposed mechanism. Together with other arrivals these non-geometrical phases complicate the seismic coda of the first arrivals. The observation and explanation of these phases might lead to independent constraints on the regional and global properties of upper mantle discontinuities.

This section tried to introduce the study of non-standard arrivals presented in this thesis and to discuss some aspects in a more global view. Only a small selection out of many valuable contributions could be named. They all are pieces of a big puzzle which only together and with the help of other disciplines can increase our understanding of the Earth.

Chapter 2

Steeply Reflected and Focused ScSH Precursors From the D'' Region

Abstract. We present evidence for precursors to the *ScS* and *sScS* (*S_DS* and *sS_DS*) phases observed at epicentral distances smaller than 30° . These precursors are intermittently observed in broadband recordings from the six Incorporated Research Institutions for Seismology stations used (western Pacific region and South America). They appear approximately 35–50 s ahead of the *ScS* arrival on the transverse component and are independent of hypocentral depth. The observed precursors are characterized by relatively large amplitudes in the frequency band from 0.05 to 0.2 Hz. A more detailed analysis is restricted to a subsidiary data set from station SNZO (New Zealand). The coherency, frequency dependence, slowness, polarity, and polarization of the precursors are discussed. Many explanations for *S_DS* can be rejected, and we conclude that a reflector 180 km above the core-mantle boundary causes these occasionally strong precursors. The large *S_DS*/*ScS* amplitudes at low frequencies require an unrealistically large impedance contrast for a one-dimensional model. We test the possibility of focusing the *S_DS* phase by a discontinuity with topography and show that structure with scale lengths of $\sim 19^\circ$ – 25° (1200–1600 km, i.e., larger than the Fresnel zone) can account for large intermittently observed *S_DS* amplitudes with their geometrical reflection points within the same Fresnel zone. This is surprising, since it is often assumed that scale lengths smaller than the Fresnel zone must be responsible for variations within a Fresnel zone. The limited data set permits no conclusions about the global properties of this phase or its implied reflector.

Apart from minor changes this chapter has been published as: Schimmel, M. & H. Paulssen, Steeply reflected *ScS* precursors from the D'' region, *J. Geophys. Res.*, 101, 16,077–16,087, 1996.

2.1 Introduction

The core-mantle boundary (CMB) is the strongest physical and chemical discontinuity inside the Earth: The density and velocity contrasts across this boundary are larger than those at the free surface. With its expected boundary layers (see *Lay* [1989] and *Loper and Lay* [1995] for a review), it plays a major role in the theory of the Earth's dynamics and evolution. The adjacent D" region [*Bullen*, 1950], the lowermost 150-300 km of the mantle, has therefore been of particular interest to geophysicists. Many seismological studies have tried to quantify the properties of D", but the seismic models vary considerably [e.g., *Lay*, 1989]. The velocity gradients above the CMB decrease compared with the overlaying mantle and may even change sign in some regions [*Doornbos and Mondt*, 1979]. A large number of studies using a variety of approaches find evidence for lateral heterogeneities at the D" (see *Young and Lay* [1987] for a review). The observations of reflected *PcP* or *ScSH* precursors at near-grazing incidence are a case in point. (*ScSH* is used to stress that transverse-polarized *ScS* phases are considered.) All studies of *ScSH* precursors are based on near-grazing incidence phases, which are observed at distances ranging from about 70° to 95° . Early evidence of *ScSH* precursors was found by *Mitchell and Helmberger* [1973] and *Lay and Helmberger* [1983]. The latter authors used waveform and travel time information to infer a 2–3% *S*-velocity discontinuity located about 280 km above the CMB in three different regions. *Young and Lay* [1990], *Weber and Davis* [1990], *Gaherty and Lay* [1992], and *Garnero et al.* [1993], among others, found evidence for similar *S*-velocity discontinuities, while *Cormier* [1985], *Schlittenhardt et al.* [1985], and *Haddon and Buchbinder* [1987] presented alternate explanations for the observed *ScS* precursors. Among the studies that do suggest a discontinuity, the inferred depth varies by as much as 150 km for different regions [*Garnero et al.* 1993; *Kendall and Shearer*, 1994].

Near-grazing *ScS* precursors from a 2–3% *S*-velocity discontinuity can be detected owing to the critical reflection and constructive interference of reflected and refracted waves. Reflections from such a discontinuity should not be visible on individual seismograms at shorter epicentral distances and, as far as we know, no steep-angle reflected precursors from D" have been reported. In this paper, we present evidence for the existence of such precursors observed at epicentral distances less than 30° . In the following, we will refer to these precursors as *S_DS* and *sS_DS* phases. We first describe our data and observations and then investigate the effect of reflector topography on the *S_DS* phase. It is not our goal to present one (nonunique) model as a final result but to find a mechanism which explains our data as well as related observations from other studies.

2.2 Data and Observations

We collected broadband seismograms from six Incorporated Research Institutions for Seismology (IRIS) stations: CTAO (Australia), SNZO (New Zealand), MAJO (Japan), CHTO (Thailand), NNA (Peru), and LPAZ (Bolivia) for the years 1991–1994 for events with an epicentral distance $\Delta < 30^\circ$, magnitude $m_b > 5.5$, and depth $h > 120$ km. The source parameters, including location and origin time, were taken from the monthly Preliminary Determination of Epicenters (PDE) bulletins; events with aftershocks or bad quality recordings were discarded. The remaining data were corrected for instrument response and rotated to obtain transverse-displacement seismograms.

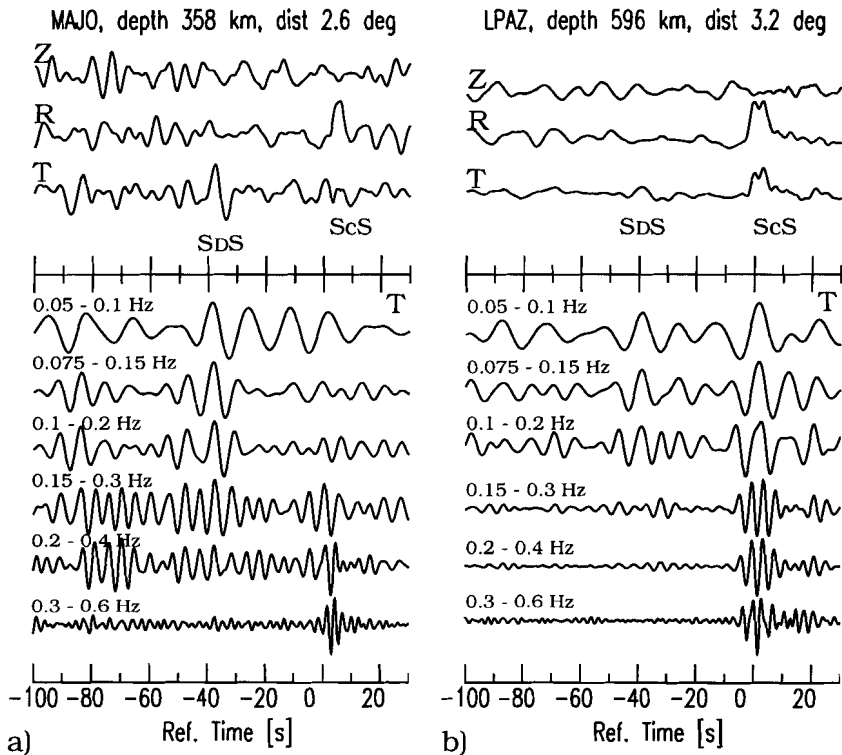


Figure 2.1. (upper panels) Three-component broadband seismograms at stations MAJO, LPAZ, CHTO, and SNZO aligned with respect to the theoretical ScS travel time. (lower panels) Transverse components band-passed at different frequencies and normalized per frequency band. A precursory signal SdS is visible at -35 to -55 s on each unfiltered transverse component. Notice the different epicentral distances and hypocentral depths (listed at the top of each figure). (This figure is continued on the following page.)

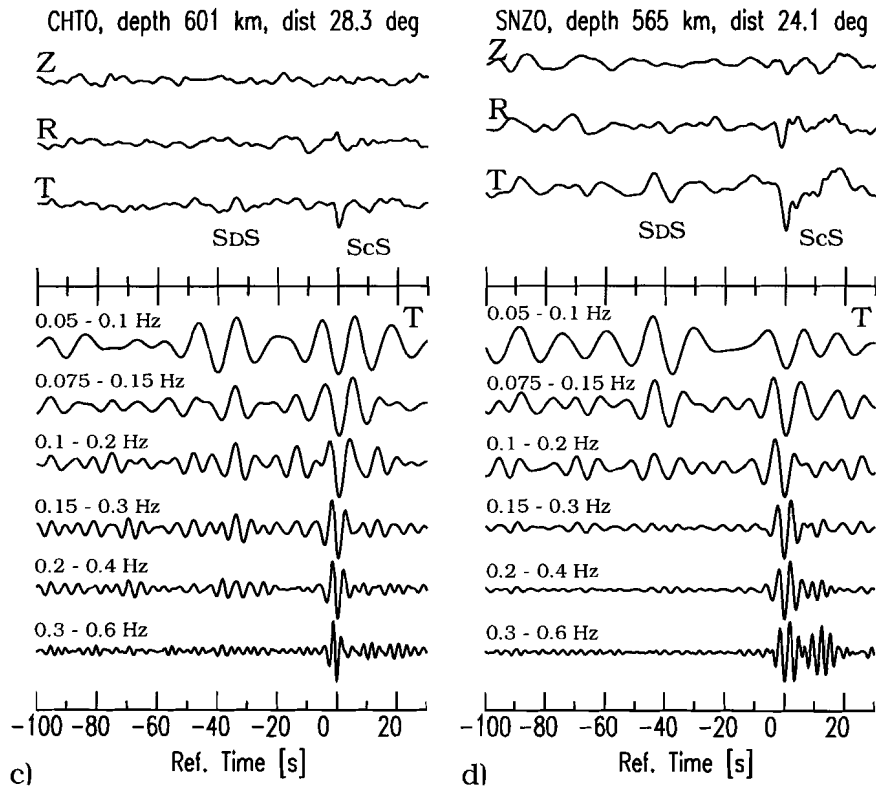


Figure 2.1. (continued)

On some seismograms, a clear *ScSH* precursor is observed on the transverse component 35–55 s before the *ScS* phase. Figure 2.1 shows four records for different events and stations. The traces have been aligned to the theoretical arrival time of the *ScS* phase at zero time. In most cases, the precursors on the transverse component are lower in frequency than *ScSH* and appear to have the opposite polarity of the *ScSH* phase.

Good quality broadband data for small epicentral distances are sparse, and the number of unambiguous data is further decreased by possible interferences with other phases, such as *sS*, *SS* and *sSS*. We discarded seismograms if these interferences could occur. Also, at distances larger than 28° , *PSS* phases are expected on the radial and vertical components which arrive close to *SdS*. We discarded the data whenever this was the case in order to avoid possibly contaminated transverse components. Our data set is greatly reduced as a result of these constraints.

Although we show here positive observations on single traces, we cannot identify the *SdS* phase on the largest part of our data owing to a high noise level. Even if subjective, *SdS* is established at about 1–10% of our recordings. A few ambiguous precursors catch attention since they are coherent with *SdS* at low frequencies, but they do not show up as a clear phase. Moreover, on some traces with good signal-to-noise ratio, we can hardly identify a precursor. A clear identification of *SdS* also requires an unambiguous *ScSH* phase. In some traces, the *ScSH* phase is quite weak or absent within a certain frequency range. The recording from MAJO (Figure 2.1a) exemplifies this. Further, the *ScSH/ScSV* amplitude ratio can be unstable. For instance, it increases from 0.5 at 0.05 Hz to 2 at about 0.5 Hz for the seismogram from LPAZ in Figure 2.1b. This might be an indicator of source and/or CMB complexity.

Most of the seismograms with a good signal-to-noise ratio and simple *ScSH* waveform were obtained for station SNZO. Figure 2.2 shows two more recordings from this station

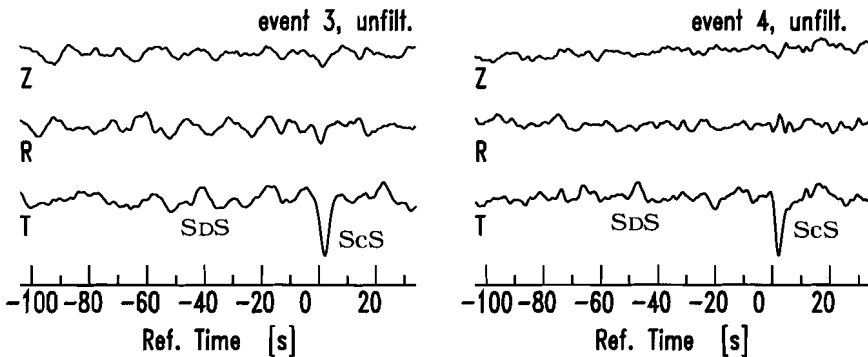


Figure 2.2. Three-component broadband seismograms at station SNZO for events 3 and 4 (see Table 2.1). *SdS* and *ScS* are clearly visible on the transverse component.

which contain a clear *ScSH* phase and a low-frequency precursor on the transverse component. Consequently, we confine our detailed analysis to data from SNZO. These comprise 37 events (Table 2.1) at epicentral distances ranging from 13° – 26° , with hypocentral depths in the range from 120 to 620 km. About 60% of the events have hypocentral depths greater than 400 km. The map depicted in Figure 2.3 shows the epicentral locations listed in Table 2.1 and their reflection points at the CMB.

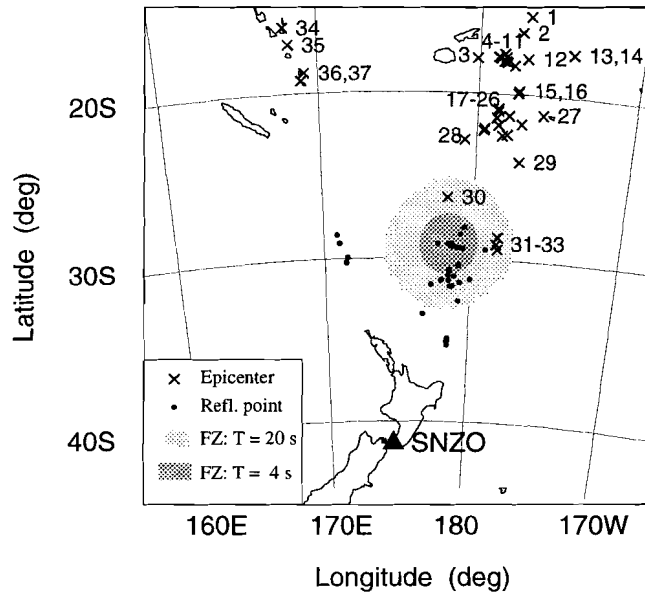


Figure 2.3. Event locations are marked by a cross and labeled with a number. The labels correspond to the event numbers of Table 2.1. Reflection points at the CMB are indicated by solid circles. The Fresnel zone at the CMB of event 6 for a period of 20 s is indicated by the light grey area. The corresponding 4-s period Fresnel zone is indicated by the dark grey area.

Table 2.1. Events Used for the Detailed Study for Station SNZO.

Event	Year	Day of Year	Longitude, ^o N	Latitude, ^o E	Depth,km	Dist, ^o
1	1993	314	-15.34	-177.03	381	26.9
2	1994	186	-16.30	-177.47	414	25.8
<u>3</u>	1993	114	-17.87	179.85	599	23.8
<u>4</u>	1994	19	-17.58	-178.50	533	24.4
<u>5</u>	1994	110	-17.80	-178.40	543	24.2
<u>6</u>	1993	106	-17.78	-178.86	565	24.1
7	1993	284	-17.85	-178.73	555	24.1
<u>8</u>	1993	80	-18.04	-178.53	589	23.9
<u>9</u>	1993	217	-18.10	-178.33	616	23.9
10	1994	68	-18.04	-178.41	563	23.9
<u>11</u>	1993	300	-18.28	-177.87	617	23.8
12	1993	92	-17.84	-177.07	362	24.4
<u>13</u>	1994	55	-17.42	-174.29	124	25.6
<u>14</u>	1994	56	-17.42	-174.27	121	25.6
15	1993	190	-19.78	-177.49	398	22.5
16	1993	91	-19.92	-177.54	406	22.3
<u>17</u>	1993	110	-20.88	-178.70	592	21.1
<u>18</u>	1994	114	-21.02	-178.69	584	21.0
19	1994	108	-21.41	-178.80	541	20.6
<u>20</u>	1993	233	-21.28	-178.02	427	20.9
21	1993	358	-21.85	-178.65	445	20.2
<u>22</u>	1994	90	-22.06	-179.53	580	19.8
23	1993	344	-22.18	-179.58	605	19.7
<u>24</u>	1992	217	-21.74	-177.21	253	20.7
25	1992	193	-22.48	-178.41	377	19.7
<u>26</u>	1992	317	-22.40	-178.10	360	19.8
27	1993	122	-21.15	-175.88	120	21.6
<u>28</u>	1993	90	-22.76	179.25	617	18.9
<u>29</u>	1993	56	-23.00	-177.22	166	18.5
<u>30</u>	1994	47	-26.27	178.27	606	15.3
31	1992	231	-28.64	-178.32	201	13.9
32	1994	139	-29.06	-178.38	258	13.5
33	1993	147	-29.36	-178.27	119	13.2
34	1994	116	-16.02	167.00	185	25.9
35	1994	124	-17.05	168.27	206	24.8
36	1994	42	-18.77	169.17	206	23.0
37	1992	285	-19.25	168.95	129	22.5

Underlined event numbers have similar ScSH waveforms and were used for the stacks of Figures 2.7 and 2.8.

2.2.1 Coherent ScS, sScS, and ScSScS Precursors

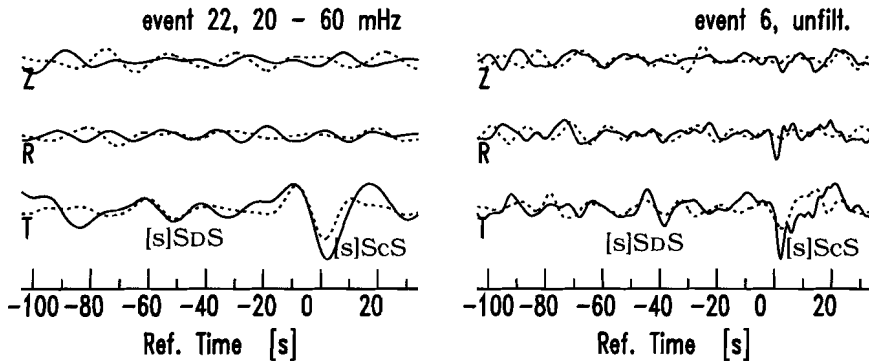


Figure 2.4. *ScS* (solid line) and *sScS* (dashed line) are aligned at 0 s and plotted on top of each other. The dashed transverse traces have been multiplied by -1.

Besides precursors to *ScS* (*SdS*), precursors to *sScS* (*sSdS*) and *ScS2* (*SdSScS* or *ScSSdS*) are sometimes observed. Figure 2.4 illustrates two examples with a low-frequency *sSdS* phase on the transverse components from events 6 and 22. The traces with the *sScSH* phase (dashed line) have been multiplied by -1 and aligned to zero time with respect to *sScS* and plotted on top of the corresponding aligned *ScS* trace (solid line). It can be seen from Figure 2.4 that the *SdS* and *sSdS* phases can be quite coherent at low frequencies. In general, it is difficult to observe *sSdS* at frequencies larger than 0.1 Hz since the traces become quite noisy, perhaps due to scattering along the three segments of the path through the uppermost mantle and crust. Coherent signal is also visible on the other components, though at different times, and this may be due to near-receiver *S*-to-*P* conversions. Here we are interested in the *SdS* phase only. Figure 2.5 shows an *ScS2* precursor which is quite similar to the *SdS* phase.

Coherent *sSdS* and *SdS* phases are also observed for the stations NNA, MAJO, and LPAZ. Figure 2.6 demonstrates a good example of coherent *ScS*, *sScS*, and *ScS2* precursors at low frequencies recorded at station NNA.

Thus we so far can conclude that (1) the existence of the precursor is independent of the take-off angle at the source which excludes near source scattering; (2) *SdS* and *sSdS* are related to *ScS* and *sScS*, which cancels the misinterpretation of another phase which would either appear before *ScS* or *sScS*; and (3) specific near-receiver scattering can likely be excluded by the similarity of the observations from different regions and distances. However, a reflector at about 180 km above the CMB can be invoked to explain the observed precursors.

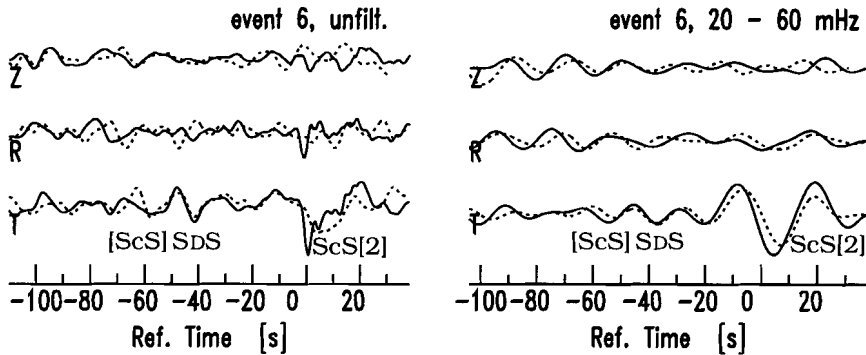


Figure 2.5. ScS (solid line) and ScSScS (dashed line) are aligned to 0 s and plotted on top of each other. The dashed traces with ScSScS have been multiplied by 3. The seismograms on the left are unfiltered and on the right are band-passed between 20 and 60 mHz.

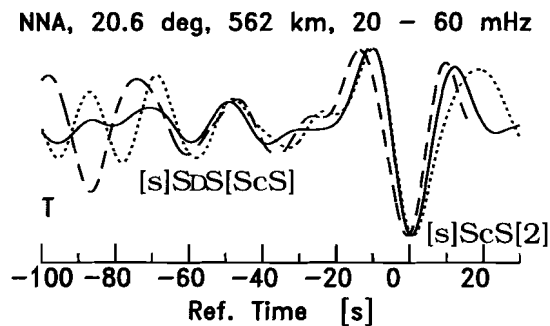
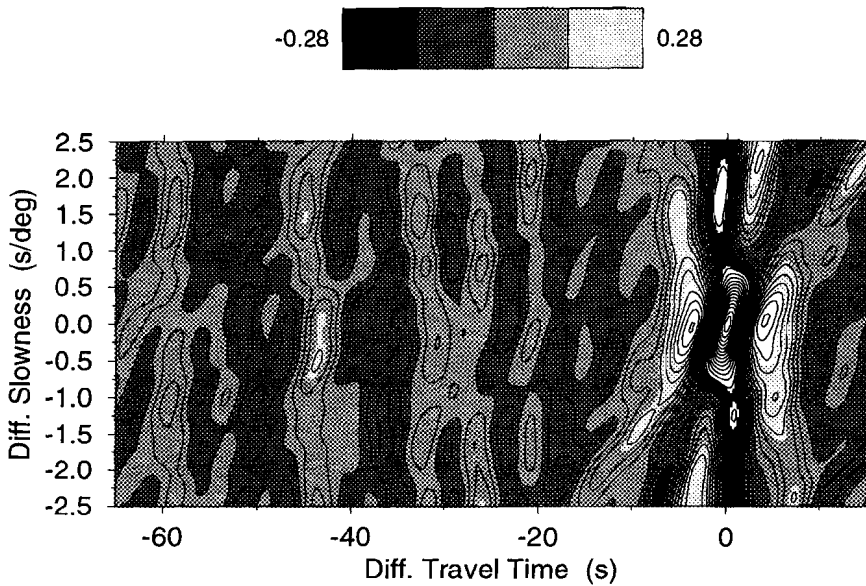


Figure 2.6. ScS (solid line), sScS (dotted line) and ScSScS (dashed line) are aligned to 0 s, band-passed between 20 and 60 mHz, and normalized. The trace with sScS has been multiplied by -1. Station is NNA (Peru), epicentral distance and hypocentral depth are 20.6° and 562 km, respectively. Precursors to all three phases are coherent at low frequencies.

2.2.2 Stacks and Slowness Determination

A reflector about 180 km above the CMB would cause a normal move-out (NMO) of the differential travel time ($t_{ScS} - t_{SbS}$) of about 6 s at a distance of 24° with a differential slowness of about 0.5 s/deg. We checked this result by performing a slant stack of 18 traces with clear and similar *ScSH* waveforms. The events used for the stack have underlined event numbers in Table 2.1. We aligned and normalized the *ScSH* phases and summed the band-passed (0.05-0.2 Hz) seismograms for different differential slownesses. The result is presented as a contour plot in Figure 2.7. The *ScSH* phase can easily be identified as the largest minimum at zero slowness and time. The precursor is clearly visible at about -43 s for a differential



*Figure 2.7. Normalized slant stack for 18 transverse seismograms. Shaded contouring ranges from -0.28 to 0.28, while the lines contour all amplitudes with a step size of 0.05. *ScSH* is visible as minimum at $\Delta t=0$ s, $\Delta p=0$ s/deg. The precursor with positive amplitude is evident at $\Delta t=-43$ s and $\Delta p \approx -0.5$ s/deg.*

slowness between 0.3 and -0.7 s/deg. Its maximum in amplitude is at about -0.5 s/deg. The timing is correct for a discontinuity at about 180 km above the CMB. However, the measured slowness is smaller than the expected value of 0.5 s/deg. This deviation can be explained by heterogeneities within the D'' region and/or topography of the reflector. For instance a reflector which dips northward with an angle of about 7° can cause the observed slowness deviation.

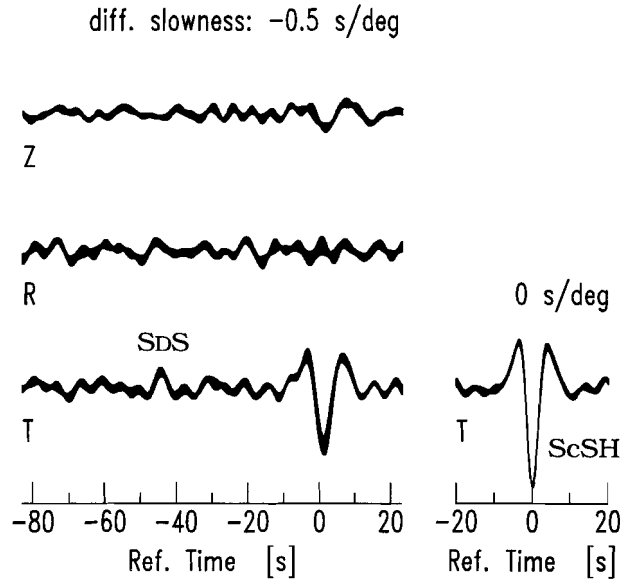


Figure 2.8. Slant-stacked seismograms for a differential slowness of -0.5 s/deg. The precursor at -43 s is mainly transversely polarized and has opposite polarity to ScSH. The one standard deviation uncertainty is indicated by the line thickness. The stacked wavelet to the right shows the ScSH signal at zero slowness.

The epicentral distances of the 18 events used range from 15.3° to 25.6° but cluster around 22° . Figure 2.8 shows stacks for each component at a slowness of -0.5 s/deg and the stacked ScSH waveforms at zero slowness. The line thickness represents the standard deviation of the stack, i.e., the 66% confidence limits, thus a thinner line indicates better-constrained amplitudes. The ScSH phase at zero slowness is a case in point; the thin lines indicate the high similarity of the ScSH signals used. The precursor is strongest on the transverse component, and the radial and vertical components show little and no visible energy, respectively.

A ScS precursor generated close to the receiver must arrive as a *P* wave in order to shorten the ScS travel time; these are ScSdP or ScSdp-type phases where “d” represents the conversion depth. Such phases lead to onsets which are expected to be strongest or at least present on the vertical component. However, both slant stacks and single traces clearly show the strongest energy on the transverse component. For similar reasons, i.e., absence of clear signals on the radial components, *Sp_{diff}S* type phases can be excluded as explanations for the precursors.

2.2.3 SdS/ScSH Amplitude Ratio

The theoretical *SH* reflection coefficient of the CMB without topography equals 1 and is independent of frequency and incidence angle, while for a realistic value of a plane discontinuity within D" (and at steep ray incidence), this is not expected to exceed 0.03. Thus the amplitude of a steep-angle reflected *SdS* phase should not be greater than the noise level. Indeed, in order to explain the large *SdS* amplitudes and their polarity with respect to *ScSH* with a reflection from a plane discontinuity in density alone entails a jump from about 5.5 to 9–10 g/cm³; the latter values are generally recognized to describe the density of the top of the outer core. Therefore a focusing mechanism is required to explain the observed *SdS* amplitudes, which greatly exceed 3% of the *ScSH* phases. Even if the *ScSH* phase was defocused, which would provide an overestimation of the *SdS* amplitude with respect to *ScSH*, this would not explain the sometimes large *SdS* signal-to-noise ratio.

Apart from the large amplitudes, we also observe frequency dependence. *SdS* appears strongest in the band from 0.05 to 0.2 Hz (see Figure 2.1). Furthermore, the observed *SdS/ScSH* amplitude ratio decreases in the frequency band from 0.1 to 0.5 Hz. The recording from station MAJO (Figure 2.1a) is an exception. The absence of a low-frequency *ScSH* could indicate structural complexity close to the CMB.

Further, almost no precursory signal is observed at frequencies larger than 0.5 Hz. Alone, this frequency dependence can be modeled by a reflection from a linear transition zone 5–15 km wide vertically. However, given the large amplitudes, frequency-dependent focusing (which might also include a frequency-dependent reflection) is more likely.

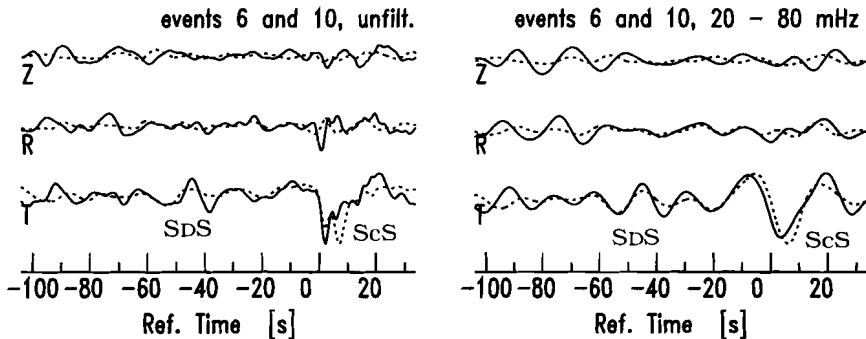


Figure 2.9. Two seismograms aligned with respect to the *ScSH* phase and plotted on top of each other. The seismograms to the left are unfiltered and to the right are band-passed. Event locations are separated by about 0.5° .

In Figure 2.9, we show traces from two different events, aligned with respect to *ScS* and plotted on top of each other. The events are separated by 0.5° , and the separation of

the geometrical reflection points is therefore approximately 0.3° . Whereas the solid trace (event 6) clearly shows a precursor at -45 s, there is less high-frequency signal evident on the other trace (event 10). As can be seen from Figure 2.1d, the precursor observed for event 6 is not visible at frequencies larger than 0.2 Hz. The Fresnel zone for a spherical reflector resembles a circle with a radius of $\sim 1.9^\circ$ for a frequency of 0.25 Hz (see Figure 2.3). Here the Fresnel zone is defined by $\Delta t \leq \frac{1}{4}T$, where T is the period and Δt is the travel time residual between rays with perturbed and geometrical bounce points. Thus events 6 and 10 show that $S_{DS}/ScSH$ amplitude ratios in the frequency band from 0.05 to 0.2 Hz may vary for different reflection points located within the same two-dimensional (2-D) Fresnel zone. These observations support the focusing model since they cannot be explained by radial one-dimensional (1-D) layering above the CMB. Frequency-dependent focusing and defocusing can occur for different reflection points within the same Fresnel zone. In other words, it looks like that station SNZO was closer to a region of focusing for event 6 than for event 10. This might explain the presence and absence of the high-frequent components of the focused wave field for the events 6 and 10.

In the presence of topography, signal from the S_{DS} precursor is also expected on the radial component. Its amplitude will depend on the source radiation pattern as well as the actual shape of topography. Indeed, some signal is visible on the radial component of the stacked records of Figure 2.8. This signal is more difficult to identify on the individual seismograms, but a hint of it might be recognized, e.g., for event 6 in Figure 2.1d. In the following we are mainly going to discuss the occasionally strong energy on the transverse component. However, any proposed model must also explain the S_{DS} energy on the radial component.

2.3 Synthetic Modeling

As established above, a focusing mechanism is necessary to explain large S_{DS} amplitudes and the variability of the observations with a reasonable velocity and density contrast. There are many ways to focus a wave field through a three-dimensional (3-D) Earth structure, and the subject of the following section is to investigate one possibility which we find to be effective: focusing through a discontinuity with topography. This approach is further justified by observations of near-grazing ScS precursors that show a variable depth to this discontinuity [e.g., *Garnero et al.*, 1993; *Kendall and Shearer*, 1994].

2.3.1 The Method

We chose a Kirchhoff-Helmholtz -related method after *Frazer and Sen* [1985] and *Frazer* [1987] which has been successfully applied for $P_{410}P$ by *Neele and Snieder* [1992] and P_{660s} phases by *Van der Lee et al.* [1994]. It is essentially a combination of geometri-

cal acoustics and plane wave reflections with the Kirchhoff-Helmholtz formulation as its backbone. Geometrical optics are used to propagate the rays between the source, discontinuity and station, and the plane wave SH - and SV -reflection coefficients are incorporated to construct a generalized reflection coefficient. We are using the single fold representation [Frazer and Sen, 1985], which means that we integrate over just one surface. This is either the CMB or the reflector above the CMB. The final seismograms are obtained by summing both time series. Thus the ScS phase is calculated for the unperturbed medium. The geometry and the laterally homogeneous background medium ensure that the wave field does not have a caustic on the reflector, which implies that there is no singularity in the integration. However, caustics at the receiver are allowed since the Kirchhoff-Helmholtz theory treats the receiver as a second source of a second wave field. Owing to the use of plane wave reflection coefficients, the method is restricted to plane waves and a local plane interface. Consequently, the scale length of the topography has to be larger than the actual Fresnel zone.

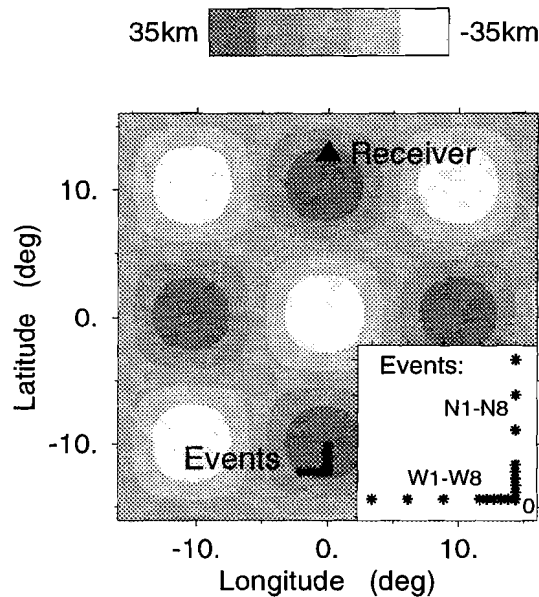


Figure 2.10. Station-event configuration projected on top of the schematically indicated egg-box like topography with scale length 20° at D'' . The enlarged event cluster is shown in the insert at the lower right. The event at the corner is labeled event 0, and its distance to the receiver is 25° . Some events have a spacing of 0.5° , others of 0.1° . Events W1 and N1 are separated by 2° from event 0.

For the synthetics, we used a station-event configuration as illustrated in Figure 2.10. The epicentral distance from event 0 (in the southeastern corner) and the receiver is 25° .

The event cluster consists of 16 more events, 8 to the west (W1–W8) and 8 to the north (N1–N8). The spacings between the hypocenters are 0.5° (W1–W4, N1–N4) and 0.1° (W5–W8, N5–N8). We used an egg-box-shaped topography schematically indicated by the shading in Figure 2.10. One of the minima of the topography is fixed at the position of the geometrical bounce point for event 0, while topography amplitude A and scale length λ are free parameters which vary the topography. A is measured from a mean depth to its extremum. Whether the wave field for a fixed station-event configuration is focused or not depends on the frequency, i.e., Fresnel zone resolution width, and the curvature of the topography, which is determined by A and λ . In other words, there exists a trade-off between A and λ for fixed frequencies, which consequently complicates distinguishing between certain models.

For our test calculations, we used a discontinuity with an S -velocity and density increase of 3%. This means that the SH -wave reflection coefficient and impedance increase are -0.03 and 6% at normal incidence. The synthetic seismograms are calculated for frequencies up to 1 Hz. The source has a spherically symmetric radiation pattern with a delta-function source. We expect focusing for scale lengths λ larger than the Fresnel zone, but not too large, because then the curvature of the topography gets too small for focusing. If the scale length is much smaller than the Fresnel zone resolution width, the effect of topography is expected to average out, but this cannot be tested by our method due to the plane wave restriction.

2.3.2 The Results

1. The most important result is that it is possible to focus the wave field of the S_{dS} phase to obtain the observed large amplitude S_{dS} phases by assuming a fairly moderate discontinuity. In the three leftmost panels of Figure 2.11, we show the results for a 3% discontinuity in S -velocity and density, with amplitude $A = 35$ km, and varying scale lengths and frequency ranges. The event 0 - station configuration (Figure 2.10) has been used for these calculations. The amplitudes at high frequency indicate strongest focusing at about $\lambda = 20^\circ\text{--}21^\circ$ ($\simeq 1200$ km). Other tests showed that decreasing the event 0 - station distance from 25° to 20° leads to amplitudes further increased by about 35%. The most important reasons for this are that (1) the SH -reflection coefficient varies as a function of incidence angle and (2) focusing depends on the configuration of event, station, and topography.

2. There exists a strong trade-off between topography amplitude (A) and scale length (λ). If A is increased, focusing is obtained for larger scale lengths, and if A is decreased, smaller scale lengths lead to focusing. Similar focused S_{dS} amplitudes for the frequency range smaller than 1 Hz are attained for scale lengths and amplitudes between $\lambda = 19^\circ$, $A = 30$ km and $\lambda = 25^\circ$, $A = 50$ km. Outside this range of topography, the focused amplitudes decrease. Two examples of lower-amplitude focusing can be found in the fourth panel of Figure 2.11. The trade-off between A and λ can be approximated by considering

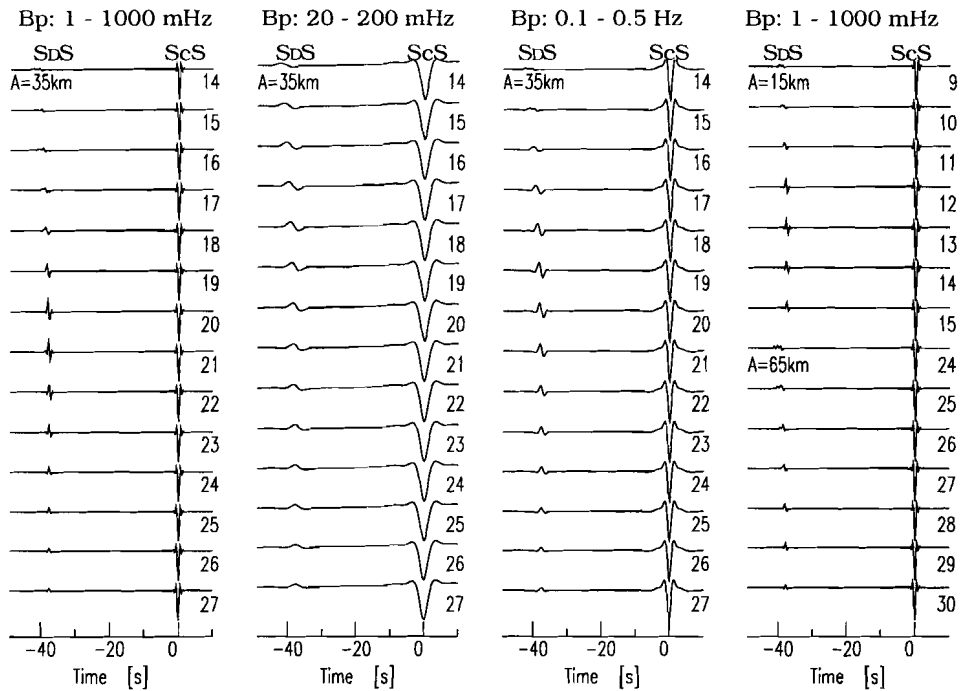


Figure 2.11. Transverse synthetic seismograms which have been calculated for the event 0 - station configuration (Figure 2.10). The number to the lower right of each trace shows the scale length λ (in degrees) used. The amplitude A was fixed to 35 km (the first three columns), 15 km (the fourth column, top 7 traces), and 65 km (the fourth column, lower 7 traces).

the theoretical focusing factor [Neele and Snieder, 1992], which is the spectral ratio of the wave fields from a perturbed and a flat reflector. Assuming that the focused amplitudes belong to one single stationary phase, the focusing factor becomes a function of A/λ^2 . This is what we approximately find from our synthetics for models which cause strong amplitude focusing.

3. In Figure 2.12, we show the seismograms for the event cluster of Figure 2.10 and demonstrate the spatial sensitivity of the focused wave field. The parameters of the topography used are $A = 35$ km and $\lambda = 20^\circ$. High-frequency reflections are only observed within a small focusing region, while low-frequency reflections occur over a wider region. It appears that within the frequency range we consider, the caustic volume decreases with increasing frequency. Here the caustic volume refers to the finite caustic for physical rays at finite frequencies [Kravtsov, 1988]. It is not expected that the caustic volume generally decreases with increasing frequencies. For instance, rays with Fresnel zones much smaller

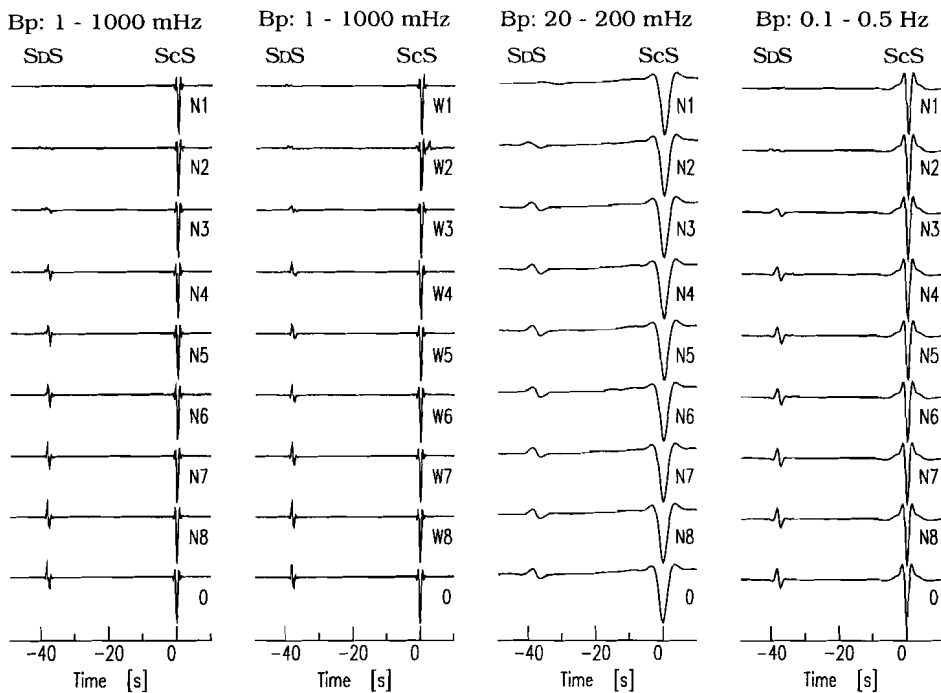


Figure 2.12. Synthetic seismograms which have been calculated for the event configuration of Figure 2.10. Topography used has an amplitude $A=35$ km and scale length $\lambda=20^\circ$. The event spacing between $N1-N2$, $N2-N3$, and $N3-N4$ ($W1-W2$, ..., analogous) is 0.5° , and all the other event locations are separated by 0.1° . The epicentral distance of event 0 to the receiver is 25° . The frequency band of the traces is indicated at the top of each panel.

than the scale length of our topography locally sample an almost plane-like reflector which does not lead to focusing. Alternatively, waves with decreasing frequencies cannot always have an increased caustic volume, since for scale lengths much smaller than the Fresnel zone, the effect of the topography on the wave field averages out to zero.

4. Figure 2.12 further shows that a variation of event position less than 2° (see $W1$ and $N1$) is enough to move out of the SdS focusing region for all frequencies. The corresponding reflection point separation is surely smaller than 1° , and Figure 2.12 therefore illustrates amplitude variations which might occur for geometrical bounce points clustered within the same 2-D Fresnel zone. A Fresnel zone with radius larger than 2° corresponds to waves with frequencies smaller than 0.25 Hz. This implies that small-scale structures are not required to explain amplitude variations within a Fresnel zone. This is mainly due to two reasons: (1) The distance from the reflector to the Earth's surface is large, which allows

the wave field to have caustics close to the receiver caused by large-scale structures at the reflector and (2) the width of these caustic volumes is small.

5. The calculated waveforms for *S_DS* have similarities to our data. The synthetic *S_DS* waveforms have opposite polarity to the *ScS* phase when no strong focusing occurs. Thus they are dominated by the impedance increase (compare with Figure 2.8). In the strong focusing region itself, the *S_DS* waveforms are more complex. They do not resemble the *ScS* waveform but look more like its negative Hilbert transform. This involves a negative reflection coefficient and the phase retardation of $\pi/2$ at a caustic. Note that these *ScS* and *S_DS* waveforms from trace 6 in Figure 2.9 approximately resemble the synthetic waveforms.

We show that focusing due to large-scale topography (1200–1600 km) of a moderate discontinuity can explain the intermittently observed large *S_DS* amplitudes. The frequency-dependent focusing depends on amplitude A and wavelength λ of the topography, vertical distance between discontinuity and receiver, the event-receiver configuration itself, and the event-receiver position relative to the topography. The small spatial sampling of the wave field and the trade-off, ambiguity, and complexity of the focusing mechanism make it difficult to further constrain the model. Indeed, we find that a *S_DS* amplitude decrease with increasing frequency (the observed frequency cut off at 0.5 Hz) can be explained by any combination of the three following circumstances: (1) The reflection coefficient is frequency dependent if the reflector is not a single first-order discontinuity. (A first-order discontinuity is a transition where the elastic parameters and/or density change discontinuously.) (2) The Fresnel zone which decreases with increasing frequency leads to a smaller sampling of the curved reflector for higher frequencies and will at one point lead to a decrease of focusing. (3) The caustic volume or focusing region gets smaller with increasing frequency. Thus any phase in the vicinity of a caustic volume will show a frequency dependence with a “fading out” of higher frequencies.

In our calculations, we considered a monochromatic sinusoidal reflector only. Structure with more scale lengths will further increase the ambiguity. For instance, assume that there is a small-scale bump superimposed on the minimum of the sinusoidally shaped reflector. If in addition the location of this bump coincides with the geometrical reflection point, then a high-frequency wave will be defocused while the low-frequency components are still focused due to the long-scale structure. We expect to observe a low-frequency precursor. Alternatively, high-frequency *S_DS* focusing could also have been suppressed by a frequency-dependent reflection coefficient and/or by having the receiver in the vicinity of the focusing zone as mentioned above.

Note that we can increase the synthetic *S_DS/ScSH* amplitude ratio even more by replacing the monochromatic sinusoidally shaped topography with a parabolic reflector which strengthens *S_DS* or by defocusing the *ScSH* phase by CMB topography. We cannot resolve all the ambiguities with the present amount of data, and we refrain from presenting a “best” model.

Last, we want to point out that our synthetic SdS phases have amplitudes on the radial component which are 60–70% of those on the transverse component. This is expected due to the smaller SV -reflection coefficient (it may even change sign) when compared with the SH -reflection coefficient for the considered slowness range. Note that the observed radial-to-transverse SdS amplitude ratio of Figure 2.8 is similar to the synthetically calculated one.

2.4 Discussion

We observe intermittent ScS and $sScS$ precursors at different stations, which we interpret to be caused by a reflector located at about 180 km above the CMB. We can rule out other possible interpretations for SdS such as near-source or near-receiver scattering. Our more detailed analysis shows the precursors for a reflector underneath the Kermadec region. The depth of the reflector is constrained by the differential travel time ($t_{ScS} - t_{SdS}$) to about 180 km. This depth estimation is based on the assumption that the lowermost 180 km can be described by a constant S -velocity of 7.26 km/s. A velocity perturbation of $\pm 5\%$ would lead to a change in depth estimation of about ± 10 km.

The large $SdS/ScSH$ amplitude ratio and the frequency dependence of the observations require frequency-dependent focusing of SdS . We tested focusing using topography, and synthetic modeling shows that realistic models can focus the wave field strongly enough to be observed. The $SdS/ScSH$ amplitude ratio from the synthetics from a monochrome sinusoidal topography reach 1/3, which is the ratio of the stacked phases from Figure 2.8. Still, we need to increase this amplitude ratio in order to explain the upper bound of $SdS/ScSH$ observed in individual traces such as presented in Figures 2.1 and 2.2. This can be done in two ways: first, by defocusing the ScS phase due to D" heterogeneities and/or CMB topography and second, by further focusing SdS . We cannot resolve this ambiguity by the presented amount of data but expect topography with dominant scale lengths on the order of 19° – 25° (that is, 1200–1600 km at the reflector) with corresponding amplitudes of 30–50 km. We showed that such topography could lead to intermittent observations of SdS .

The inferred long-scale structures further agree with the mapped ScS – S and $sScS$ – sS differential travel times by *Wyssession et al.* [1994] or the multiple-phase analysis by *Young and Lay* [1990]. *Wyssession et al.* [1994] find anomalies with dominant lateral dimensions of about 1000–2500 km or more beneath the west Pacific for the lowermost 300 km of the mantle in a study which could resolve much smaller scale lengths.

Furthermore, the depth of the reflector presented here, 180 km, is in good agreement with a ScS precursor found by *Gaherty and Lay* [1992] and *Garnero et al.* [1993] for near-grazing S waves under Eurasia and the mid-Pacific D" region, respectively. Also, SV diffracted waves around the Earth's core underneath Alaska can be best modeled by a discontinuity at a depth 180 km above the CMB [*Lay and Young*, 1991]. Our estimated topography of

30–50 km would result in a scatter in differential travel times of 2–5 s, which is consistent with observations by *Gaherty and Lay* [1992]. The intermittent observation of their 160-km precursor caused *Gaherty and Lay* [1992] to assume that its spatial extension is limited. We suspect, however, that the intermittent character of their wide-angle observations has a cause similar to the steeply reflected precursors of our study, i.e., focusing and defocusing due to topography.

A similar mechanism could also explain the clustering within a Fresnel zone of observable and unobservable precursors from the top of the D" (at approximately 300 km above the CMB). Such observations have been reported by *Weber* [1993] for broadband *SdS* and *PdP*. *Weber* [1993] finds reflector spots as small as 130 km, while reflectors as large as 1500 km have also been inferred [e.g., *Young and Lay*, 1990]. This does not contradict our suggestion of focusing, since *Young and Lay* [1990] used long-period data, while *Weber* [1993] worked with broadband data with dominant periods of 4–6 s for *SdS* and 1 s for *PdP* waves. We demonstrated that topography of large scale lengths causes highly variable short-period reflections observed in small focusing regions and more stable long-period reflections in larger focusing regions. Consequently, the top of the D" at ~ 300 km, as both studies bring out, can be explained by a global reflector, which is dominated by relatively large scale lengths. Indeed, *Nataf and Houard* [1993] proposed a global discontinuity on top of D" which, due to laterally varying properties, leads to intermittent detection.

Evidence for a *P* wave discontinuity at 160 km above the CMB, a depth similar to our *S* wave reflector, has furthermore been presented by *Wright et al.* [1985] from short-period data using different arrays and source regions. They used travel time and slowness measurements of low-angle reflected *PdP* phase underneath Indonesia, western Pacific, and mid-Pacific. On the other hand, *Neuberg and Wahr* [1991], searching for high-frequency *PdP* phases steeply reflected from one small spot between Tonga and Australia, did not see such a discontinuity. However, *H-C. Nataf* (personal communication, 1996) observed steeply reflected *PdP* phases from the top of D" underneath Alaska.

Steep incidence *ScS* reverberations were considered by *Revenaugh and Jordan* [1989]. They observed a reflector which, due to ambiguity inherent to their method, could be caused either by a rapid impedance decrease in the upper 100 km of the mantle or by an impedance increase ($R \sim -0.03$) about 170 km above the CMB. The latter possibility is consistent in polarity and depth with our observations. *Revenaugh and Jordan* [1989] used 40 mHz low-passed data, which are much less affected by focusing than the higher frequencies used here. This explains their impedance increase of about 6%, which is much less than we would find from the focused phases by assuming plane layering and higher frequencies. In a more extensive study, *Revenaugh and Jordan* [1991] gave no evidence for the discontinuity 170 km above CMB.

2.5 Conclusions

We have found intermittent observations of *ScSH* precursors recorded at small epicentral distances ($\Delta < 30^\circ$) and conclude that these are steeply reflected phases from a reflector located at about 180 km above the CMB. With evidence from synthetic seismograms for steeply reflected *S* waves, we infer that topography with scale lengths of about 1200–1600 km can explain the observed frequency-amplitude characteristics of the precursor. We do not exclude the presence of shorter scale length structure but find that (at least for steep incidence reflections) the observation of intermittent phases and the interpretation of reflector spots smaller than the Fresnel zone can be explained by long-scale topography. Owing to a limited data set, we can give no evidence for a global presence of the reflector described here. However, we believe that the D" is at least locally layered.

The frequency dependence of focusing can be understood as a combination of three processes. These are (1) the frequency-dependent size of the caustic volume, (2) the different sampling of the curved discontinuity due to the frequency-dependent Fresnel zone, and (3) a frequency-dependent reflection coefficient. The ambiguity in the interpretation and separation of these effects can probably be decreased with good spatial sampling of the focused wave field. Altogether, more broadband data and 3-D modeling for a broad frequency range are required for a better understanding of the radial structure of D".

Chapter 3

Noise Reduction and Detection of Weak, Coherent Signals through Phase Weighted Stacks

Abstract. We present a new tool for efficient incoherent noise reduction for array data employing complex trace analysis. An amplitude unbiased coherency measure is designed based on the instantaneous phase which is used to weight the samples of an ordinary, linear stack. The result is called the phase weighted stack (PWS) and is cleaned from incoherent noise. PWS thus permits detection of weak but coherent arrivals. The method presented can easily be extended to phase weighted cross-correlations or be applied in the $\tau - p$ domain. We illustrate and discuss the advantages and disadvantages of PWS in comparison to other coherency measures and present examples. We further show that our non-linear stacking technique enables us to detect a weak lower mantle P -to- S conversion from a depth of approximately 840 km on array data. Hints of a 840 km discontinuity have been reported, however such a discontinuity is not yet established due to lack of further evidence.

A slightly changed version of this chapter has been accepted for publication as: Schimmel, M. & H. Paulssen, Noise reduction and detection of weak, coherent signals through phase weighted stacks, *Geophys. J. Int.*, in press, 1997.

3.1 Introduction and Motivation

In the determination of Earth structure the identification of weak signals such as reflections or conversions from mantle discontinuities plays an important role. Their travel times, amplitudes and spatial coherencies at different frequencies are crucial for inferences about impedance contrast, thickness and topography of the discontinuity. Identifying these weak seismic phases usually requires many good-quality seismograms and a good spatial sampling of the target. In seismic exploration the target sampling, amount of data and source can be controlled during the design of the experiment. However, in global seismology we are generally restricted due to a sparse distribution of earthquakes and stations and unprecisely known source parameters. This decreases the amount of applicable techniques for signal enhancing in the usual seismological framework.

Weak phases can only be detected by their coherent appearance on different traces. Various techniques have been designed to detect coherent signals. For array data stacking techniques can be applied where the traces are summed along assumed travel time curves. These can be the normal-move-out (NMO) curves for reflected phases or just straight travel time curves for slant stacks. Assuming that the summation of seismograms is performed along the correct travel time curve, the signal is expected to sum up constructively while the surrounding noise amplitude should decrease. An important factor for the noise reduction is of course the data quality. Unfortunately, a large part of the seismogram consists of signal generated noise. Consequently, other larger and more prominent phases in the vicinity of our weak signal are considered noise. Even though they stack less coherent than our signal they can appear as large amplitude features in the stack and lead to ambiguous phase detection. Difficulties in suppressing noise using ordinary stacks was the motivation for non-linear stacking techniques such as the n -th root process by *Muirhead [1968]* and *Kanasewich et al. [1973]*. In seismology n -th root stack has been successfully applied to detect weak non-prominent phases such as *s670P* (*Richards and Wicks, 1990*) or *s920P* (*Kawakatsu and Niu, 1994*) conversions. Another motivation for non-linear stacking is to lower the threshold for event detection. For instance *Weichert [1975]* successfully used a logarithmic process similar to the n -th root processing. A number of other beamforming techniques exists. *Neele and Snieder [1991]* increased the resolution of the conventional beamforming by applying inverse theory in order to optimize the array response. *Krüger et al. [1993]* designed a double beam method which combines source and receiver array beamforming. *Zürn and Rydelek [1994]* recall the phasor-walkout method to show how coherent harmonic signals such as the eigen modes of the Earth can be detected on single time series. They use a graphical representation of the Fourier transform which reveals the random, coherent, or periodic nature of signals in a complex spectrum. Further, *Rydelek and Sacks [1989]* apply phasor-walkouts to detect periodicities in earthquake catalogs. Phasor-walkouts and the method proposed here, although very different, are based on the same principles, namely phase-coherency of complex signals.

In exploration seismology a function called semblance (*Taner and Koehler, 1969*) is widely used to detect coherent signals across an array, and semblance weighted slant stacks are used for signal detection (e.g. *Stoffa et al., 1981; Kong et al., 1985*). Here we present a similar technique, which is based on a more direct coherency measure by involving instantaneous phases. It is called a phase weighted stack and we will use the abbreviation PWS. We will show an application and discuss the PWS in comparison with the n -th root stack (*Muirhead, 1968*), energy normalized cross-correlation (*Neidell and Taner, 1971*), the coherency functional after *Gelchinsky et al. [1985]* and semblance (*Taner and Koehler, 1969*).

3.2 Method

We present a coherency measure which is explicitly independent of the amplitude and use this measure to weight the samples of the linear stack. The coherency measure is based on the instantaneous phase of the unstacked traces as will be visualized using complex trace analysis. We outline the method below.

3.2.1 Analytic Signal and Phase Stacks

In complex trace analysis an analytic signal or complex trace $S(t)$ is constructed from the seismic trace $s(t)$. This happens by ascribing the seismic trace $s(t)$ to the real part of the analytic signal and its Hilbert transform $H(s(t))$ to the imaginary part of $S(t)$. The analytic signal then takes the form $S(t) = s(t) + iH(s(t))$. The analytical signal can also be expressed with time dependent amplitude $A(t)$ and phase $\Phi(t)$.

$$S(t) = s(t) + iH(s(t)) = A(t)e^{i\Phi(t)} \quad (3.1)$$

$A(t)$ is the envelope of $s(t)$ and $\Phi(t)$ is called instantaneous phase (e.g. *Bracewell, 1965*). We visualize the analytic trace as a vector with length $A(t)$ which rotates with progressing time in the complex space around a time axis (*Taner et al., 1979*). The projection of this curve onto the surface spanned by the real axis and the time axis is our seismic trace $s(t)$.

We picture the linear or ordinary stack $1/N \sum s_j(t)$ as the real part of the sum of the analytic traces. Index j enumerates the N traces used. Figure 3.1a schematically shows the stack of two analytic traces $C(\tau) = S_1(\tau) + S_2(\tau)$ at fixed time $t = \tau$, i.e. on a sample by sample basis. Let us assume that the phase of $S_2(\tau)$ is variable, then we know $C(\tau)$ ends on the circle indicated with dashed lines. The envelope $|C(t)|$ will be maximal if both instantaneous phases $\Phi_1(\tau)$ and $\Phi_2(\tau)$ are equal. In that case the signal is coherent. The sum of incoherent signal adds to a smaller $|C(\tau)|$. $|S_1(\tau)|$ will in general differ from $|S_2(\tau)|$, and in the presence of large amplitude noise $|C(t)|$ can be larger for noise than for the coherent tiny signal. Especially the stack of small datasets is biased by this sort

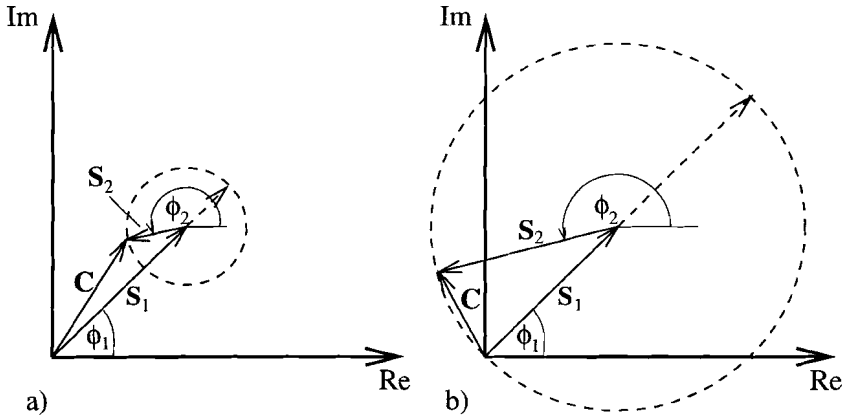


Figure 3.1. a) Visualization of the summation of two samples from analytic traces $S_1(t)$ and $S_2(t)$ in the complex plain. The sum vector C is not very sensitive to changes in the instantaneous phase Φ_2 . b) $S_1(t)$ and $S_2(t)$ are normalized on a sample by sample basis. C is now very sensitive to changes in the instantaneous phase. $|C|$, the phase stack, is a direct measure of the coherency.

of noise. We bypass this and increase the S/N ratio for $|C(t)|$ by normalizing the analytic traces $S_1(t)$ and $S_2(t)$ sample by sample. This is illustrated in Figure 3.1b and we call the following sum a *phase stack* since no amplitudes are explicitly involved:

$$c(t) = \frac{1}{N} \left| \sum_{j=1}^N e^{i\Phi_j(t)} \right| \quad (3.2)$$

where N is the number of traces used. The amplitudes of the phase stack range between 0 and 1 as a function of time. If the instantaneous phases of the signals at a certain time are coherent, then the amplitude of the phase stack equals one. Zero amplitude means that the signals summed up completely destructively. The phase stack is a measure of coherency as function of time, i.e. the effectiveness of the stack on the base of the instantaneous phase is described. The amplitudes of the seismic traces are only involved to compute the instantaneous phase. We like to mention here that the phase stack $c(t)$ can be smoothed similarly to other measures which are mainly used in seismic exploration. Hereafter the smoothed phase stack $\widetilde{c}(t)$ is obtained by averaging over a time gate centered at time t with width $2T$:

$$\widetilde{c}(t) = \frac{1}{2T+1} \sum_{\tau=t-T/2}^{t+T/2} c(\tau) \quad (3.3)$$

In equation 3.3 t , τ and T are indices rather than time variables.

3.2.2 Phase Weighted Stacks

The objective is to suppress stacked signals which are not coherent. For this purpose we involve the phase stack as coherency measure for the sum of seismic traces. The idea is to use the phase stack as a time dependent weight of the linear stack. This is easily performed by the multiplication of both terms:

$$g(t) = \frac{1}{N} \sum_{j=1}^N s_j(t) \left| \frac{1}{N} \sum_{k=1}^N e^{i\Phi_k(t)} \right|^\nu. \quad (3.4)$$

Now it becomes clear why we call this a *phase weighted stack* or just PWS. Namely, every sample of the linear stack will be weighted by the coherency of its instantaneous phases. Weak coherent signals are enhanced through the incoherent noise reduction. The phase stack acts as filter with a certain sharpness of the transition between phase similarity and dissimilarity which is controlled by the power ν . The linear stack is retrieved with $\nu = 0$. The PWS is a non-linear stack and waveform distortion is expected. However, coherent signal will not be distorted too much since the instantaneous phase is presumed to be more or less stationary on the individual traces. The strongest distortions are expected for incoherent signal. In the following we involve synthetic data to show the merits of PWS and phase stack.

3.3 Application to Synthetic Data

In subsequent sections we show the performance of PWS using synthetic data. This encompasses a qualitative comparison of PWS with the linear stack and n-th root stack (Muirhead, 1968; Kanasewich *et al.*, 1973) which is another effective non-linear stacking technique. A second important issue which is addressed in this section is the coherency measure itself. We compare the phase stack to other coherency measures which are often applied in seismic exploration.

3.3.1 Phase Weighted Stack Versus Linear Stack

In the following example we compare the abilities of the PWS and linear stack to detect coherent signals and to distinguish them from signal generated noise. Figure 3.2a shows 10 synthetic seismograms. Arrows with numbers label the distinct arrivals to simplify their naming. Arrivals 1 to 4 label the coherent signals and arrivals 5 and 6 label the signal generated noise. The same seismogram section but with superimposed noise is illustrated in Figure 3.2b. Note that it seems impossible to recognize all arrivals by eye due to relative high amplitude noise. Figures 3.2c and d demonstrate the squared phase stacks (PS), linear stacks (LS) and PWS's at zero slowness. The squared phase stack ($\nu=2$) is used to calculate the PWS. It can be regarded as the power of the phase stack which helps to increase the S/N ratio. (We like to mention here that an analytic signal with zero amplitude theoretically does not have a phase. However, numerically a phase zero is ascribed to a zero amplitude signal. Consequently phase stacks of zero amplitude traces equal one. In Figure 3.2c the phase stack deviates from one due to numerical noise in the time series of Figure 3.2a.) The phase stack of Figure 3.2c equals one for the coherent arrivals 1 and 4, and is still large for arrival 2 which interferes with arrival 3. The noise contaminated data yield a phase stack (Figure 3.2d) which indicates coherency for the same arrivals. Due to the noise they are less coherent than in Figure 3.2c but stand clearly out of the surrounding noise.

Note that from Figure 3.2b it seems to be impossible to distinguish between coherent arrival 4 and 'signal generated noise' 5 and 6. Indeed all three arrivals show up as a clear signal in the linear stack and thus might be misinterpreted as coherent arrival. However, the PWS's (bottom traces in Figures 3.2c,d) bring certainty. They are cleaned from arrivals 5, 6 and other noise. This is justified since the PWS is constructed from the linear stack by multiplication with the phase stack. Phases 5 and 6 are not coherent over the array (see Figure 3.2a) and are therefore down-weighted by the phase stack. This decision could not have been made by inspecting the noisy data themselves or the linear stack. Note that the random noise is similarly down-weighted.

Figures 3.2e and f show the contoured envelopes of the linear stacks and PWS's at different slownesses. The stacks are performed with respect to the trace at the distance of 10 deg. Both slant stacks are normalized to one and contoured for intervals 0.1. PWS

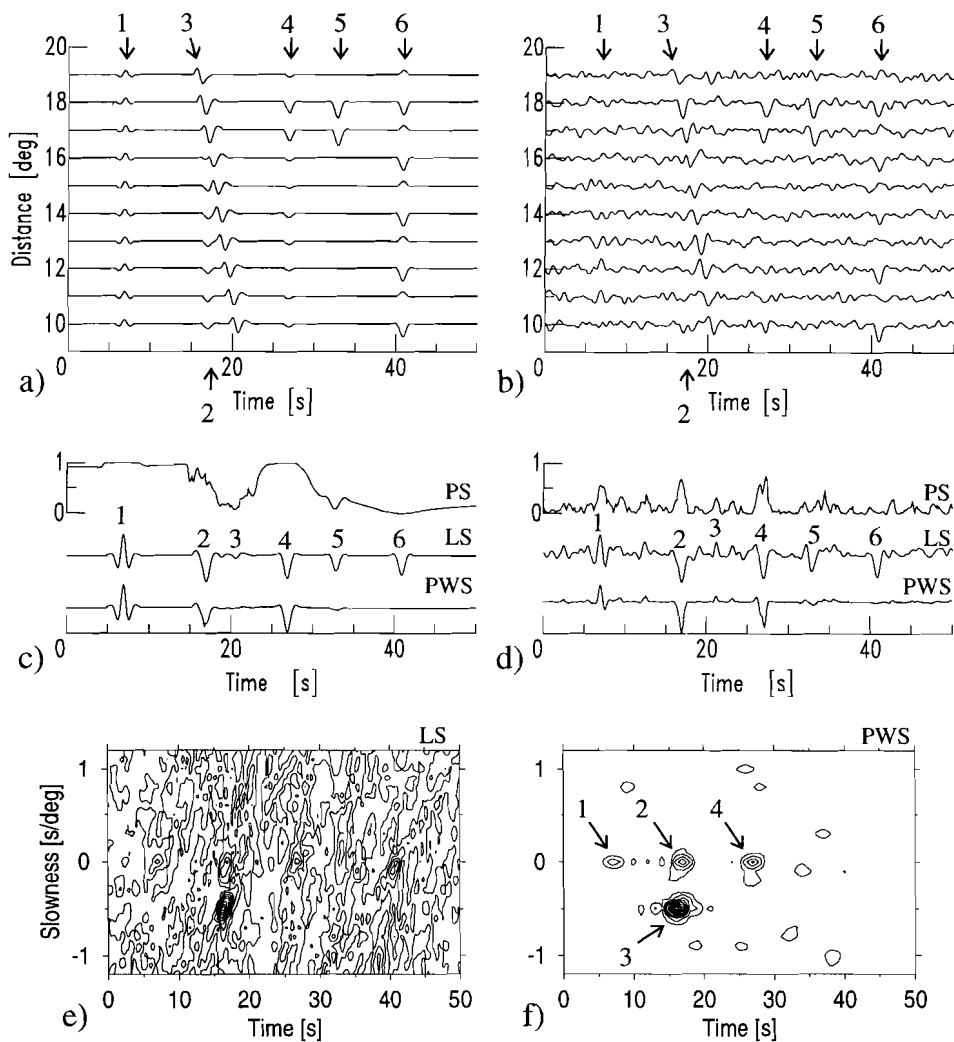


Figure 3.2. a) Synthetic seismograms with different arrivals labeled by numbers. b) Same as a) but with random noise. c) From top to bottom: squared phase stack, linear stack and PWS for the noise free seismograms. d) Same as c) but for the seismograms with noise. Figures e) and f) show normalized slant stacks of the noisy data of Figure b). The stacks are performed with respect to the trace at 10° over a slowness range of -1.2 to 1.2 s/deg. Contoured are the envelopes of the linear stacks (e) and PWS's (f) with 0.1 intervals.

enables a correct slowness and arrival time determination of all weak arrivals while the linear stack is too noisy. PWS is indeed cleaned from signal generated noise which in the linear stack might lead to misinterpretations.

3.3.2 Phase Stack Versus Other Coherency Measures

Many other coherency measures are based on the cross-correlation coefficients of real or complex traces. Some of them differ by a different normalization. For the subsequent comparison three in seismic exploration commonly used coherency measures have been selected.

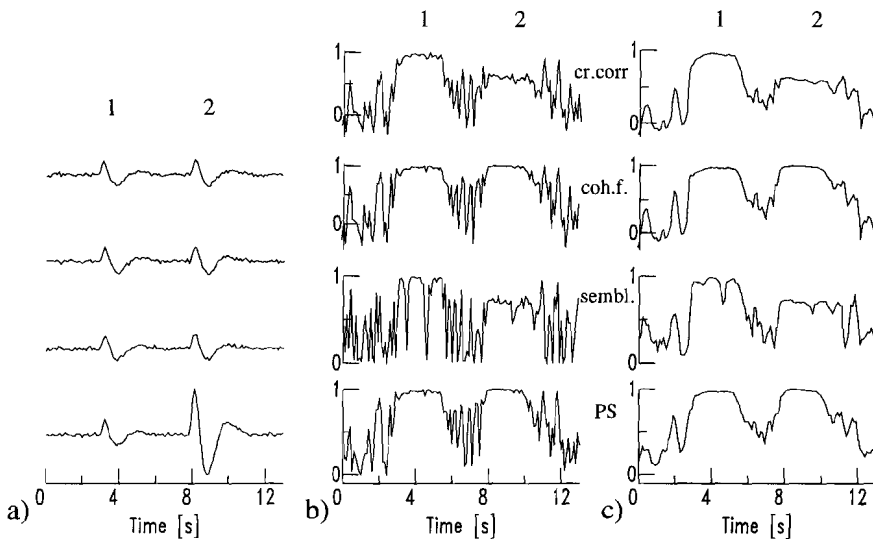


Figure 3.3. a) Synthetic time series with two arrivals each. Waveforms are all similar but the amplitude of the second signal of the last trace is multiplied by three. b) From top to bottom: cross-correlation sum, coherency functional, semblance, phase stack for data from a). c) Same as b) but smoothed with a time gate width of 0.4 s (5 samples).

Figure 3.3a shows four time series each with a wavelet at about 3 s and 8 s. Their waveforms, arrival times and amplitudes are similar except one wavelet at 8 s which is three times larger. Some small amplitude noise has been added to the traces.

First we apply the energy normalized cross-correlation sum (after eq. 10 in *Neidell and Taner* [1971] but for analytic traces) to our data. First trace in Figure 3.3b demonstrates the result. The second trace of Figure 3.3b shows the ‘coherency functional’ after *Gelchinsky et al.* [1985] (their eq. 21). This measure is normalized by the cross-correlation sum of envelopes. Note that these two measures can reach negative values. Thirdly (Figure 3.3b

third trace) we apply the semblance which is defined as an output-to-input energy ratio (*Taner and Koehler, 1969; Neidell and Taner, 1971*). The output energy is determined by the squared stack and the input energy by the stack of squared traces. The last trace in Figure 3.3b shows the squared phase stack. Square has been used since the other measures also involve the power two. Note that the squared phase stack becomes similar to the semblance which uses real traces and explicitly involves amplitudes. Semblance and phase stack range between zero and one.

In exploration seismology the coherence measurements are often smoothed by averaging over a time gate such as in equation 3.3. The influence of a 0.4 s time gate is illustrated by the traces from Figure 3.3c. Smoothing is a simple and often used filter to stabilize waveforms and simplify signal detection. Throughout this paper we further do not apply smoothing since we like to present the method in its plain form without obscuring any undesired features.

All these measures have in common that they become equal to one in case of phase and amplitude similarity, i.e. for equal instantaneous phase and envelope. This is fulfilled for the first arrival in our data in Figure 3.3a and explains the maximum values between 3 and 5 s in Figure 3.3b,c. Note that the semblance reaches zero whenever the corresponding sample of the stack has zero amplitude. This causes the high frequency character of the semblance function and justifies smoothing.

The cross-correlation sum, coherency functional and semblance are amplitude-biased coherency measures. Consequently, these measures do not depend on the waveforms alone but also on their relative amplitudes. This means that if one changes the amplitudes without modifying the waveforms then the coherence measure generally varies. The signals at ~8 - 10 s in our data from Figure 3.3a have equal instantaneous phases but varying amplitudes. The cross-correlation sum and semblance give a coherency smaller one (Figures 3.3b, c), as they penalize coherent signals with varying amplitudes. Conversely, the coherency functional and phase stack result in coherency one. Both measures perform equally well for our data. The phase stack is not sensitive to varying amplitudes since no amplitude information is involved (see eq. 3.2). The coherency functional is amplitude-unbiased only for phase coherency of all the records.

We like to mention that the measures applied to our data are based on different design philosophies. For instance penalizing signals with varying amplitude can be an advantage for certain applications. For our application we consider the phase stack (Figure 3.6d) to be the better coherency measure, since it is not biased by the signal amplitudes and thus justifies its use for weighting stacks. Specially for the detection of weak signals we should not punish these when their amplitudes vary.

3.3.3 Phase Weighted Stack Versus N-th Root Stack

Lastly we compare our stacking technique with another often used non-linear stacking technique: the so-called n -th root stack (Muirhead, 1968; Kanasewich *et al.*, 1973). We treat it here separately because, due to the nonlinearity, the results might appear similar to PWS. The n -th root stack is defined as

$$y(t) = \text{sign}(r(t))|r(t)|^n \quad (3.5)$$

where

$$r(t) = \frac{1}{N} \sum_{j=1}^N \text{sign}(s_j(t))|s_j(t)|^{\frac{1}{n}} \quad (3.6)$$

The power n is a number larger equal one. The linear stack is retrieved with $n = 1$; $n > 1$ leads to a non-linear amplification which brings out small amplitude signal more clearly. It occurs on the expense of waveform distortion (e.g. Kanasewich *et al.*, 1973) which for simple signal detection might not be of importance. In Figure 3.4 we compare the PWS

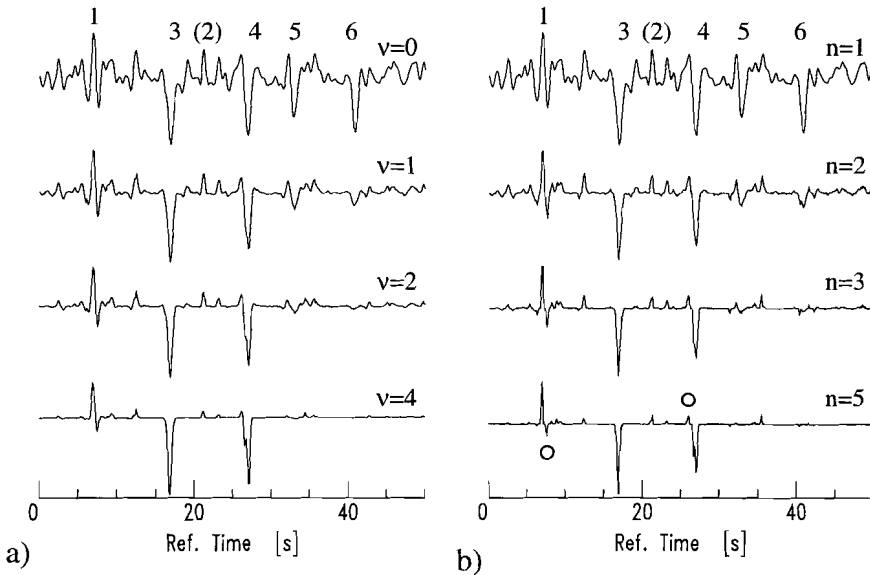


Figure 3.4. PWS (a) versus n -th root stack (b) at different power (ν and n) for data from Figure 3.2b. Uppermost stacks ($\nu = 0$, $n = 1$) equal the linear stack. Label 1, 2, and 4 mark the coherent arrivals. Open circles mark onset of spurious signals (see text).

(3.4a) with the n -th root process (3.4b) for the data of Figure 3.2b. The uppermost panel of Figure 3.4 shows the linear stacks as they are obtained by both techniques with $\nu = 0$

and $n = 1$, respectively. The labels mark the coherent signals. The other panels show the ability of both methods to enhance the coherent signals by increasing power. We observe that the waveform distortion due to non-linearity is smaller in the PWS than in the n -th root traces. The waveforms in the n -th root traces become narrower for increasing n . This waveform distortion can go even so far that spurious arrivals seem to be generated although in this example they are very small. We marked them with an open circle in Figure 3.4b. A comparison with the linear stack shows that these arrivals are in fact part of one wavelet. Strong spurious arrivals can be recognized in the real data example from section 3.4.3. Both, PWS and n -th root stack, seem to be appropriate for signal detection. However, PWS is based on a more physical background of phase coherency and permits a separation into its components, namely the linear stack and phase stack.

3.4 Application to Real Data

In the following we illustrate the performance of the stacking techniques and the coherency measures by using real data. We selected data of an earthquake which occurred 599 km underneath the Peru-Brazil border region (10.97°S , 70.78°W) on the 17th of October 1990. The 9 broadband seismograms used are recordings from the NARS-NL array (Network of Autonomously Recording Stations which was employed in The Netherlands that time (Paulssen *et al.*, 1990)). The arrivals we detect are weak and less coherent than in the synthetic case study. A qualitative comparison of the different techniques evidently points to the advantages of phase stack and PWS.

3.4.1 Phase Stack Versus Linear Stack

Data preprocessing consists of rotation of the horizontal components to obtain radial and transverse polarized records, aligning the data to zero time with respect to the P arrival and band-passing them between 0.02 and 0.2 Hz. The three components of every recording have been normalized with respect to the P phase on the Z-component. Figure 3.5a shows the P -wave coda including the pP phase at about 129s on the radial components. These traces have been summed up yielding the linear stack. Its envelope (dotted line) and phase stack (dashed line) are plotted in Figure 3.5b. From the phase stack it is obvious that there are three coherent phases (marked by a dot) in the coda of the P phase (excluding pP). However, this is not evident from the envelope of the linear stack. What is more the signal between 80 and 90 s on the linear stack might easily be misinterpreted as a coherent arrival, whereas the phase stack shows that it is not. As a result we expect them to be down-weighted in the PWS. The squared phase stack ($\nu = 2$) is used to calculate the PWS. Linear stack (dotted lines) and PWS (solid lines) for the R and Z-component are displayed in Figures 3.5c and d. The amplitude range plotted corresponds to 12% of the P wave amplitude on

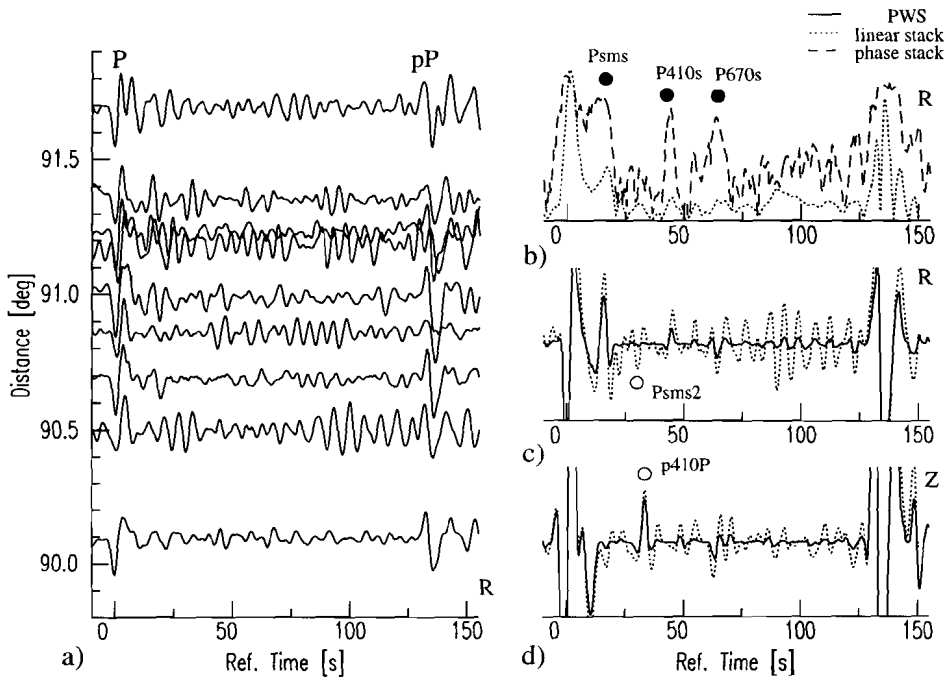


Figure 3.5. a) Radial traces recorded at NARS-NL, aligned with respect to the P-phase on the Z-component and band-passed between 0.02 to 0.2 Hz. b) Envelope of linear stack (dotted line) and phase stack (dashed line) for data presented in a). c) Linear stack (dotted line) and PWS (solid line) for R-component. Maximum amplitude plotted corresponds to 12% of the P-wave amplitude on the Z-component. d) Same as c) but Z-component.

the Z-component. Notice that the amplitudes of the PWS are smaller than or equal to the amplitudes of the linear stack since the coherency weight does not become larger than one.

The first two arrivals marked with a filled circle in Figure 3.5b can be identified as S-waves which left the source as P-waves, since there is no coherent arrival on the Z-component and since they arrive too early for a pure S-wave. The first dot labels a *Psms* phase which reverberated once in the crust as an S-wave. Its amplitude on the PWS trace is about 60% of the linear stacked amplitude. Thus the *Psms* phase experienced a 40% amplitude reduction due to incoherences. Also the first multiple reverberation *Psms2* (*Psmsms*) appears in the linear stack (open circle in Figure 3.5c), but is obviously much more incoherent since it is much stronger down-weighted in the PWS than the *Psms* arrival. The second dot in Figure 3.5b marks a P phase converted to S at the 410-km discontinuity (*P410s*). The linear stack shows the *P410s* phase and the first Moho multiple *Psms2* with similar amplitude. However, in the PWS *P410s* stands out more clearly since it sums up

more coherently. The interpretation of the third signal in Figure 3.5b is more ambiguous since there is also energy on the Z-component (Figure 3.5d). Phase weighted slant stacking showed that there is interference of two arrivals at about 66 s which are separated by more than 1 s/deg in the slowness domain. One ($P670s$) has predominant energy on the radial component, the other at larger slowness has more energy on the vertical component. Finally, the open circle in Figure 3.5d indicates a clear longitudinally polarized arrival. It could be a P -wave reverberation near the source or receiver. A possible explanation would be a $p410P$ phase, which is a near source underside reflection from the 410-km discontinuity. This signal is almost not down-weighted, thus very coherent.

Figure 3.5 shows that the detection of coherent signal is simplified due to the amplitude reduction of incoherent signal. The amplitude reduction cleaned the PWS from incoherent signal and together with the linear stack permits a more unambiguous phase detection.

3.4.2 Phase Stack Versus Other Coherency Measures

Here we apply the energy normalized cross-correlation sum (Figure 3.6a), coherency functional (3.6b), semblance (3.6c), and squared phase stack (3.6d) to the data of Figure 3.5a.

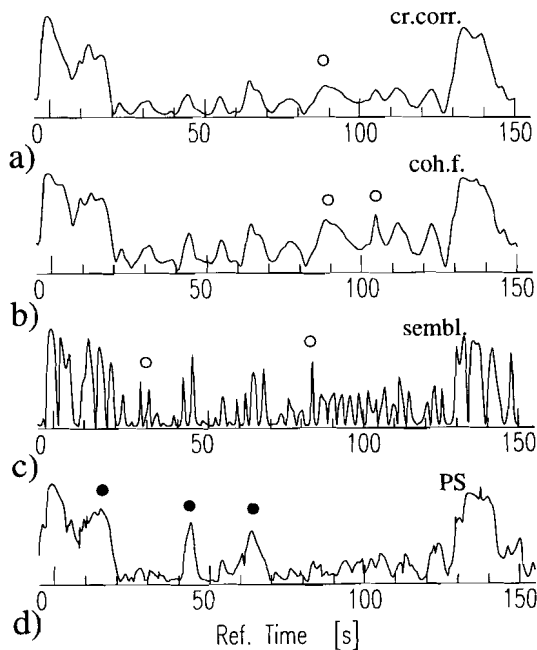


Figure 3.6. Energy normalized cross-correlation sum (a), coherency functional (b), semblance (c) and squared phase stack (d) for data from Figure 3.5a.

Figure 3.6 enables a direct qualitative comparison between the different techniques to detect weak phases. For instance, Figures 3.6a-c show many large amplitude signals. However, some of those (marked by an open circle) do not coincide with the picks of Figure 3.6d. From the phase stack we know that the coherency increases with the similarity of instantaneous phases only. This is its essential advantage since it enables to detect weak arrivals which are more coherent than the surrounding signal. The coherency measures of Figure 3.6a-c depend on the amplitudes. This dependence can obscure or feign weak coherent arrivals by assigning a coherency which is smaller than the coherency of a less phase coherent but large amplitude arrival.

Among 3.6a-c the semblance (Figure 3.6c) seems to give the best coherency measure. However, a larger variation in amplitude of the coherent arrivals would result in a much poorer semblance (see Figure 3.3). We recall that this measure is usually smoothed. However, smoothing would not improve the S/N ratio.

3.4.3 Phase Weighted Stack Versus N-th Root Stack

Now we apply the n -th root stack (Muirhead, 1968; Kanasewich *et al.*, 1973) to the data of Figure 3.5a. In Figure 3.7 PWS (3.7a) is compared with the n -th root process (3.7b).

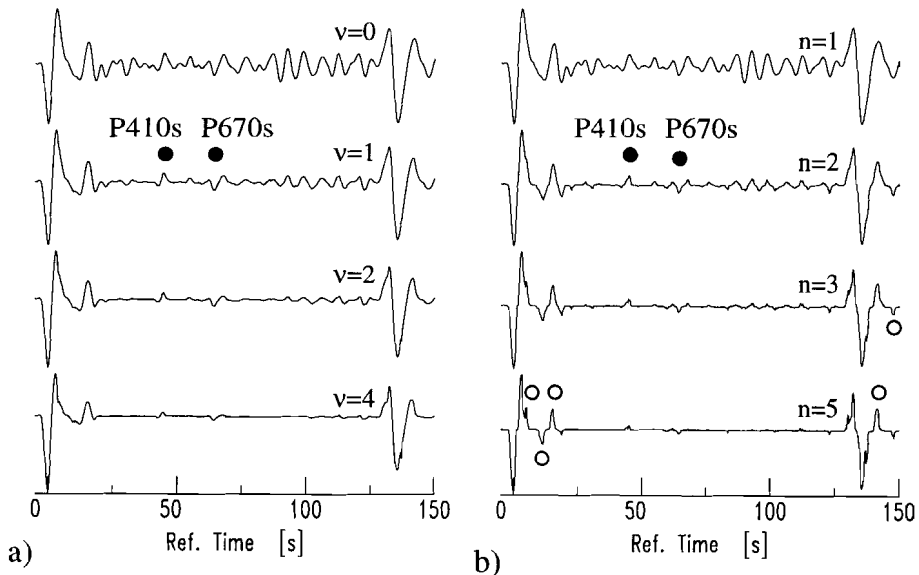


Figure 3.7. PWS (a) versus n -th root stack (b) at different power (ν and n) for data from Figure 3.5a. Uppermost stacks ($\nu = 0$, $n = 1$) equal the linear stack. Open circles mark spurious signals which feign to be independent arrivals.

The uppermost panel of Figure 3.7 shows the linear stacks as they are obtained by both techniques with $\nu = 0$ and $n = 1$, respectively. The other traces show that both methods efficiently suppress noise. We observe that the waveform distortion is smaller in the PWS than in the n -th root traces as spurious arrivals (open circles) seem to be generated by this last method. Comparison with the linear stack shows that these arrivals are in fact part of one wavelet. Note that such artifacts are well-known and might be recognized in, for instance, *Kanasewich et al.* [1973] and *Richards and Wicks* [1990].

Although PWS and the n -th root stack perform almost equally well on our data we prefer to apply PWS for the detection of weak but coherent signals. PWS seems to suffer less from waveform distortions and spurious phases which can be larger than the coherent signal. It further permits a separation into the linear stack and its phase coherency, the phase stack.

3.5 Another Application: Detection of Weak *P840s* Phases

Lastly we illustrate how PWS helped us to detect a coherent weak phase which is not predicted by standard Earth models. We selected data of three more events with hypocenters underneath North-West Argentina (1991 June 23, 26.8°S 63.35°W, 558 km, $m_b = 6.4$), the Bonin Island region (1991 May 3, 28.08°N 139.59°E, 433 km, $m_b = 6$), and Peru (1991 July 6, 13.11°S 72.19°W, 105 km, $m_b = 6.2$). The events were recorded at 9, 4, and 5 broadband receivers of the NARS-NL array, respectively. Data were processed similar to the recordings from the Peru-Brazil event. Figure 3.8 shows the linear stacks (3.8a,c) and the PWS's (3.8b,d) of the radial (solid lines) and vertical components (dotted lines) of the Argentina and Bonin Island event. The Argentina event (Figure 3.8a,b) has an epicentral distance of $\sim 100^\circ$ to the reference station used for data alignment. Consequently, the first arrival is a core diffracted *P*-wave. The epicentral distance of the Bonin Island earthquake is 90° . The first arrivals are the *P* and *PcP* phase. Striking is the clear observation of radially polarized signals 80 s after the first arrivals. They are marked with filled circles in the PWS's in Figure 3.8b,d. After recognizing them on the PWS's they are also identified on the linear stacks where they are marked with open circles. This phase is also present in the stacks of the Peru-Brazil event (from Figure 3.5 however at higher frequencies) and for the Peru event.

The interpretation could be either a *P*-to-*S* conversion from a discontinuity at a depth of approximately 840 km (*P840s*) or a *Pp220s* phase which experiences one surface reflection and a reflection-conversion at 220 km depth. Both phases arrive at about the same time and are indistinguishable by slowness using the NARS-NL data per event. Possible *Pp220s* phases are observed for the North American craton by *Bostock* [1996]. However, comparing the differential travel time from the Argentina event and the Peru or Peru-Brazil event (these three events have almost the same back azimuths) one finds a negative differential slowness as is predicted for the *P840s* phase. There are two other points in favor of a *P840s* rather

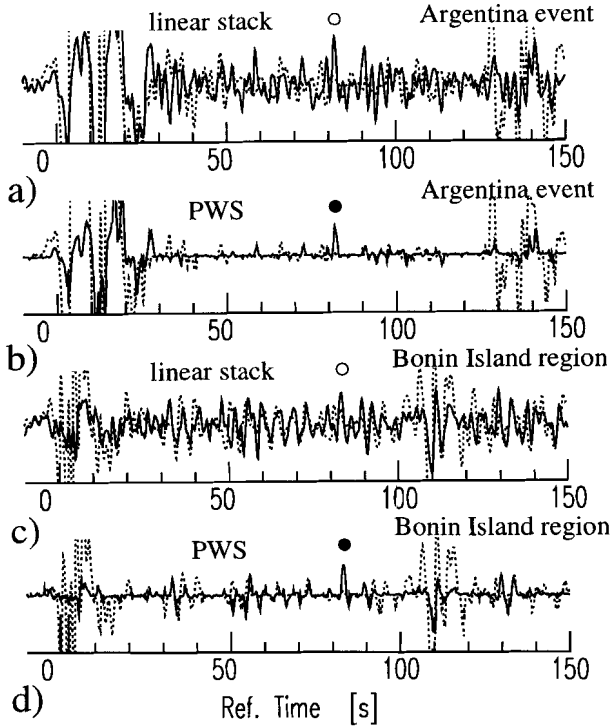


Figure 3.8. Linear stack for Argentina event (a) and Bonin Island event (c). b) and d) contain the corresponding PWS's. The Z and R-components are presented with dotted and solid lines, respectively. The data are band-passed between 0.05 and 0.6 Hz. Filled circles point to the clear P840s arrival in the PWS, while open circles mark the same phase in the linear stack.

than a $Pp220s$ phase: (1) A $Pp220s$ phase experiences one more reflection and two extra passages through the upper most mantle than a $P840s$ phase would do. We therefore do not expect that a $Pp220s$ phase is coherent at high frequencies as will be shown below. (2) A $Pp220s$ phase has multiplicity 5 which means there are four other phases with same travel time and slowness. These are $Ps220p$, $p220sP$, $P220sp220p$, and $p220ps220P$. One would expect a hint of these phases on the PWS of the vertical component. Altogether we favor $P840s$ rather than $Pp220s$.

In Figure 3.9 we manually aligned the stacked P_{diff} and P phases on the Z-components (dashed lines) and the $P840s$ phases on the R-components (solid lines) to obtain the best waveform coherency between both phases. To achieve this the vertical traces had to be multiplied by -1 and shifted by 79s (3.9a) and 79.5s (3.9b and c), respectively. Striking is the coherency between both phases at high frequencies. This means that little waveform

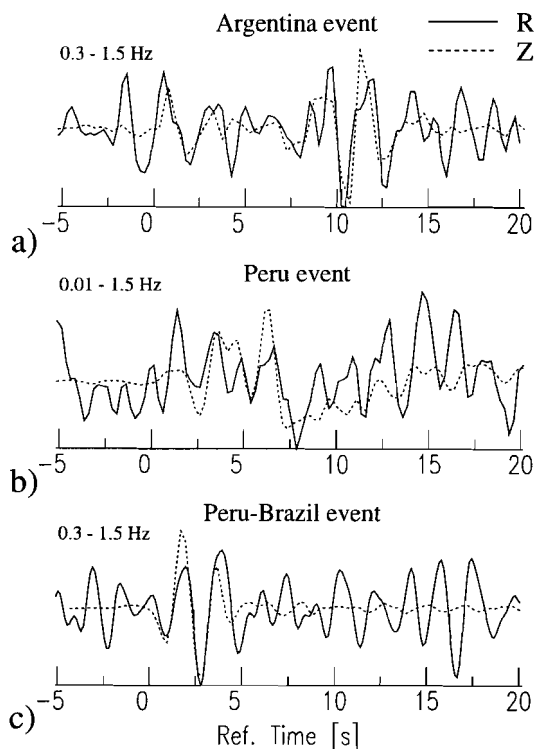


Figure 3.9. Stacked waveforms with P_{diff} (a) and P (b and c) on the Z-components (dashed lines) and $P840s$ on the R-components (solid lines). Dashed traces are normalized, multiplied by -1 , and shifted by 79s (a) and 79.5s (b and c), respectively.

distortion occurred at the high frequencies and a sharp 840 km discontinuity can be inferred (Richards 1972; Paulssen 1988). For instance a 4 km thick linear transition zone at about 840 km depth yields a transmission coefficient which decrease at 1 Hz to about 80% and at 1.5 Hz to about 60% of the transmission coefficient at zero frequency. Increasing the transition zone would increase the frequency dependence and waveform distortion. Note that the polarity of the $P840s$ phase is opposite to that of the first arrival. This would imply a small S -velocity decrease at about 840 km. First evidence for $P840s$ phases has been presented by Paulssen [1988]. She performed linear stacks of 48 events with different azimuths (mainly coming from the Japan region) recorded at individual NARS stations and illustrated a clear signal on the radial component. Shearer [1990] reports to observe a hint of a $Pp840p$ phase in his global data stacks. Such a phase has a multiplicity two, this means it can be a near source- or near receiver-site reflection. In a 1-D earth both arrive at the same time and sum to double amplitude. Poupinet [1974] requires a strong S -velocity gradient at

850 km depth in order to model a $PL(S)$ coupled wave observed at 40° epicentral distance. There is no global evidence for a 840 km discontinuity and we lack more information in order to explain its nature. Its study is not the purpose of this note.

3.6 Discussion and Conclusions

We developed a non-linear stacking technique for signal enhancing through incoherent noise reduction. The results are stacked traces which are cleaned from incoherent noise. This enables the detection of weak signals, even for a small amount of data.

Similar to PWS, phase weighted cross-correlations can be designed and used for signal recognition or arrival time picking. The phase stack can further be used to weight the misfit function between synthetic and stacked waveform data. Its advantage would be that one avoids fitting large amplitude noise better than weak but coherent portions of the waveform. In this chapter we restricted ourselves to PWS and illustrated its applicability. No quantitative investigation to the merits of PWS was performed, but the presented examples justify its use for the detection of weak phases. For instance the P -to- S conversions in Figures 3.5, 3.8, and 3.9 were not detectable in the linear stacks but they were in the PWS's.

The advantages compared to other non-linear stacking techniques are two-fold: 1) The phase weighted stack can be separated into a phase stack and a linear stack. This enables a better control of the physics behind the non-linear process. The phase stack is an amplitude-unbiased coherency measure. 2) Waveform distortion of coherent signals is expected to be minimal since these signals should be stationary in phase over the entire waveform. Consequently, waveform distortion does not depend on amplitudes but on the coherency of the components of the stack. Due to the coherency weight the stack is more sensitive to time offsets and allows therefore a more accurate slowness determination. In other words phase weighted slant stacks can improve the time and slowness resolution of weak and coherent phases.

In this chapter we found confirming evidence for a discontinuity at about 840 km. This discontinuity is detected from events with different azimuth and seems to be sharp at least locally beneath the Netherlands. More observations and a more detailed study of the 840 km discontinuity are required to explain its nature but this is not object of this chapter.

Chapter 4

Asymmetrically Reflected PP and SS Precursors: 1. Observations

Abstract. Since more than 30 years asymmetrically reflected *PP* precursors are observed at epicentral distances ranging between 80° and 120° . Slowness and travel time constrain their ray paths to have bounce points at about 15° to 30° distance from the receiver or source. Their existence has been explained by the presence of small scale heterogeneities in the lithosphere, the presence of dipping interfaces, or upper mantle reverberations and conversions. We show asymmetrically reflected *PP* and *SS* precursors observed for different regions and different event-station azimuths. It is shown that these arrivals cannot be explained by the existing generation mechanisms. In chapter 5 we propose a new mechanism which can generate asymmetrically reflected precursors in a realistic one-dimensional (1-D) Earth. Here we focus on the characteristics of the asymmetrically reflected precursors to *PP* and *SS*. We compare observational and theoretical results which confirm that these precursors are likely be explained by the new generation mechanism.

A slightly changed version of this chapter is submitted for publication as: Schimmel, M. & H. Paulssen, Asymmetrically reflected PP and SS precursors: 1. Observations, *submitted to J. Geophys. Res.*, 1997.

4.1 Introduction

Since more than 30 years symmetrically and asymmetrically reflected phases are observed in the P -wave coda of seismic recordings for distances ranging between 80° and 120° . These phases appear before the PP -phase and are therefore referred to as PP precursors. The symmetrically reflected precursors are known as PdP phases and have their reflection point at depth d midway between source and receiver. First observations of PdP phases are reported by *Nguyen-Hai* [1963], *Bolt et al.* [1968], and *Bolt* [1970]. These symmetrically reflected precursors are recognized by their travel time and their slowness which is slightly smaller than the slowness of PP . Besides these symmetrically reflected phases, precursors with similar travel time but slowness values close to the values for P or P_{diff} phases are reported (e.g. *Wright and Muirhead* [1969]). Their slowness constrains the precursors to have an asymmetrical ray path. So far, there are three categories of explanations:

(1) *Wright and Muirhead* [1969], and *Wright* [1972] explain the observation of asymmetrically reflected precursors by underside reflections at a 4° - 15° dipping interface at about 20° distance from the source or receiver. Such phases would be visible due to the high amplitude P -waves which are caused by upper mantle travel time triplications. With the reflection at a dipping interface Snell's law is obeyed and such precursors are thus stationary phases. Recently *Weber and Wicks* [1996] report the observation of similar phases at the German Regional Seismic Network (GRSN) which they use to map the boundary of a subducting slab.

(2) The ubiquity, duration and amplitude of the precursor wave train however, caused *King et al.* [1975] and *Cleary et al.* [1975] to take small scale random irregularities in the crust and uppermost mantle into consideration. They explain the amplitude characteristic of precursory wave trains at frequencies ranging between 0.6 Hz and 3 Hz by scattering of high amplitude P -waves. According to *King et al.* [1975] and *Cleary et al.* [1975] the scattering region is about 100 km thick and characterized by a correlation length of 10 km and root mean square values of $\sim 1\%$. More recently *Kato and Hirahara* [1991] used PP precursor arrival times collected by the International Seismological Center (ISC) to perform a frequency analysis. They concluded that most of the precursors must have a scattering origin.

(3) The scattering hypothesis does not explain the observed spatial coherency present at low frequencies (*Ward* [1978], *Husebye and Madariaga* [1970]). *Ward* [1978] suggests that S -to- P conversion-reflections and/or conversions at mantle discontinuities are a fundamental and global contributor to the P -wave coda. These conversion-reflections are enhanced relative to the phases with purely P path due to the general dominance of S -motion over P -motion from their double couple sources. According to *Ward* [1978] they explain the so-called asymmetrically reflected precursors. *Husebye and Madariaga* [1970] came to a similar conclusion after rejecting inner core reflections and higher modes of diffracted P -waves as a possible mechanism.

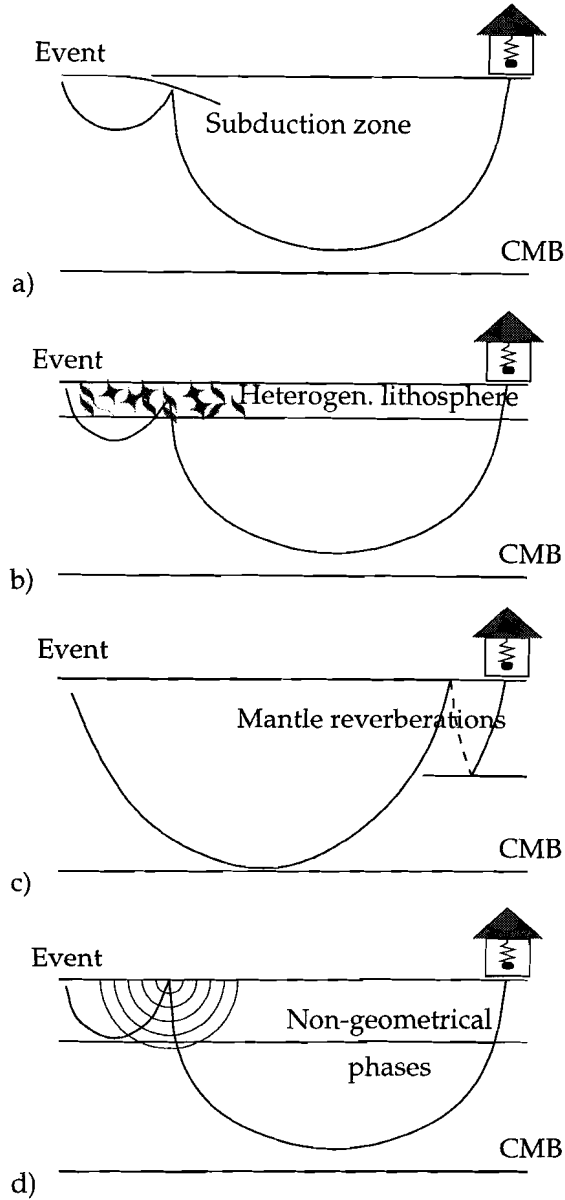


Figure 4.1. Cartoons of possible explanations for asymmetrically reflected precursors: a) reflection at dipping interface, b) scattering at a heterogeneous lithosphere, c) mantle reverberations including P- and S-waves, d) non-stationary phases which this chapter addresses.

In Figure 4.1a-c we summarize these three possible mechanisms which explain the *PP* precursors with an asymmetrical ray path. However, they do not explain the observations that will be presented in this chapter. Figure 4.1d illustrates the mechanism that we are going to propose. It explains the asymmetrically reflected precursors as non-geometrical phases which can be generated even without the presence of lateral heterogeneities. We present the observations and explanations of these precursors in two chapters. This chapter shows observations of *PP* and *SS* precursors and discusses them with respect to the existing and the newly proposed generation mechanisms. The details of the proposed generation mechanism are presented in chapter 5. The comparison of theoretical and observational results confirms that the asymmetrically reflected precursors are likely explained by our proposed generation mechanism. Thus, it seems that these phases are a fundamental contributor to coda waves.

4.2 Data and Observations

4.2.1 Data Acquisition

In order to investigate the coherence of *PP* and *SS* precursors we seek for record sections per event. The broadband data used were collected by the Incorporated Research Institutions for Seismology (IRIS) and accessed through their Fast Archive Recovery Method (FARM). In addition we used data from the German Regional Seismic Network (GRSN). We inspected record sections from randomly selected events with magnitude $m_b > 6$, and a large station density between 80° and 120° distance. We seek for phases which are not directly related to the *P* (or *P_{diff}*) and *S* (or *S_{diff}*) arrivals but which appear in their coda. Consequently, we favored record sections from events with rather large *PP/P* (*SS/S*) amplitude ratio. This should diminish the effect of reverberations which are directly related to the first arrival and which might obscure phases with different slowness such as the asymmetrically reflected precursors. All record sections show precursory energy before the *PP* and *SS* arrivals. We studied these precursors when they appeared as clear or coherent arrivals to enable an unambiguous identification. Here we show the record sections from two events to point to the characteristics of the asymmetrically reflected precursors.

4.2.2 PP Precursors

Figures 4.2 and 4.3 show the record sections and slant stacks for two shallow events at the Marianas and Philippines. Their source parameters are taken from the monthly Preliminary Determination of Epicenters (PDE). The event at the Marianas occurred on August 8th, 1993 at 12.98°N and 144.80°E at 59 km depth with magnitude $m_b = 7.1$. The Philippines event took place on May 5th, 1995 at 12.63°N and 125.30°E at 16 km depth with magnitude $m_b = 6.2$. In the following we show record sections and slant stacks which contain travel

time curves and symbols which mark the predicted travel times and slownesses of different arrivals for model ak135 (Kennett *et al.*, 1995). *PB410P*, *PC410P*, *PB660P*, *PC660P* and *PZ760P* label the asymmetrically reflected precursors such as predicted by our generation mechanism. They will be discussed at a later stage.

The Record Sections

The seismograms of Figures 4.2a and 4.3a show the coda of core diffracted *P*-waves including the *PP* phases. The seismograms of Figure 4.2a are unfiltered and clearly demonstrate the presence of *PP* precursors which start about 60 s before *PP*. The recordings at distances larger than 102° are from stations located in Germany (GRSN) with the exception of the recordings from SPA (South Pole, Antarctica) and CCM (Cathedral Caves, Missouri, U.S.A.). Note that all these seismograms show similar precursory wave trains which can be traced to recordings from KONO (Kongsberg, Norway), ANTO (Ankara, Turkey), and ANMO (Albuquerque, New Mexico, U.S.A.) at smaller distance.

In Figure 4.3a we show band-passed (0.01 - 0.1 Hz) seismograms which were recorded in California by an IRIS/IDA station (PFO) and TERRAScope stations (all the others). On this array data we recognize weak arrivals by their coherency. The precursors are indeed coherent and seem to start at about -100 s with the slope of the dashed travel time curve at that time. The first weak arrival is followed by precursors which are larger in amplitude. Similarly to the Marianas event of Figure 4.2a the unfiltered seismograms from the Philippines event show a large amplitude precursory wave train which begins at about 60–70 s before the *PP* phase. Note that the precursors seem to build up a wave train which ends before the *PP* arrival. In other words there seems to be a gap between *PP* and the precursory wave train.

The Slowness

We aligned the traces with respect to the P_{diff} phase (Figure 4.2b) and the *PP* phase (Figure 4.3b) to carry out slant stacks. We used phase weighted stacks (PWS) for differential slowness (see chapter 3 for details) with respect to P_{diff} and *PP*, respectively. PWS employs complex trace analysis to weight every sample of the linear stack with its phase coherency. This technique cleans the stacks from incoherent noise and has been successfully applied to detect weak but coherent mantle reverberations and conversions. The amplitudes of the PWS envelopes are contoured in Figures 4.2b and 4.3b. The theoretical slowness and travel time of important upper mantle reverberations and symmetrically reflected precursors (*P410P* and *P660P*) are marked by filled circles. Their phase names are explained and illustrated by Shearer [1990]. The upper mantle reverberations such as *Pp410p* and *Ps410p* are diffracted and have therefore the same slowness as P_{diff} (Figures 4.2b and 4.3b). Both slant stacks show a gap in time between the precursors and *PP*. The slowness of the

Marianas, 1993 Aug. 8, 12.98N, 144.80E, 59 km, unflt.

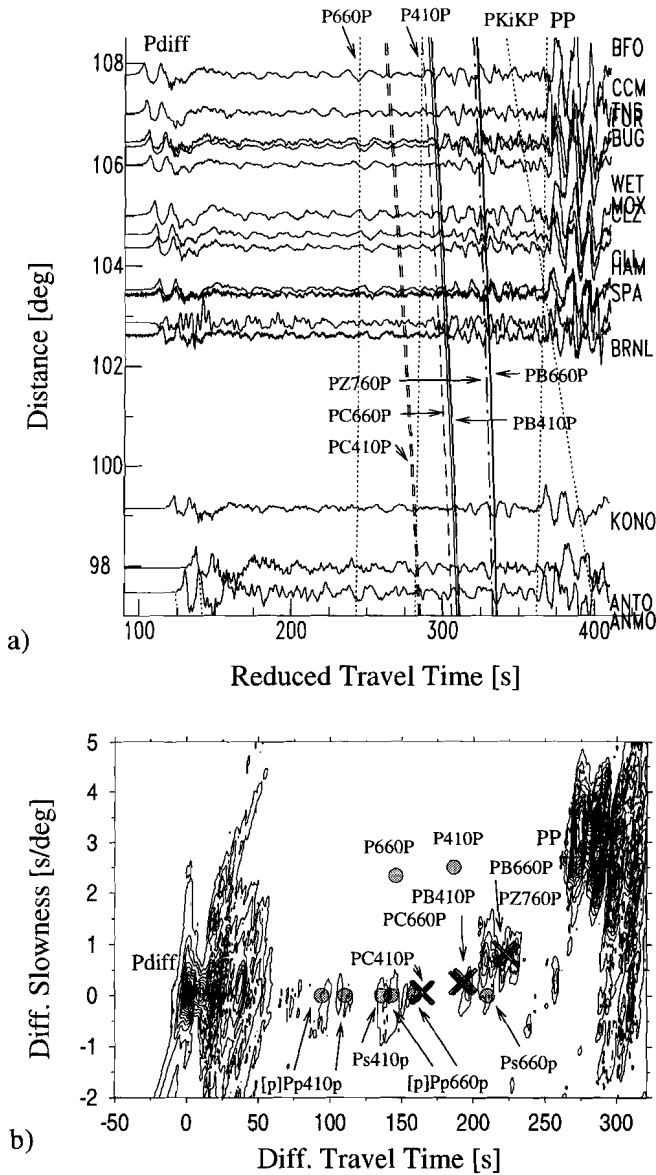


Figure 4.2. a) Unfiltered vertical component broadband recordings obtained from IRIS and GRSN. The stations are from different regions with different back azimuths to the event at the Marianas. Travel time curves correspond to predicted geometrical arrivals (dotted) and non-geometrical (dashed or solid) precursors. b) Contour plot of the envelopes of phase weighted stacks per slowness for the data from a). Phases with zero differential slowness are diffracted at the core. Crosses mark predicted non-geometrical precursors.

Philippines, 1995 May 5, 12.63N, 125.30E, 16 km, 0.01 - 0.1 Hz

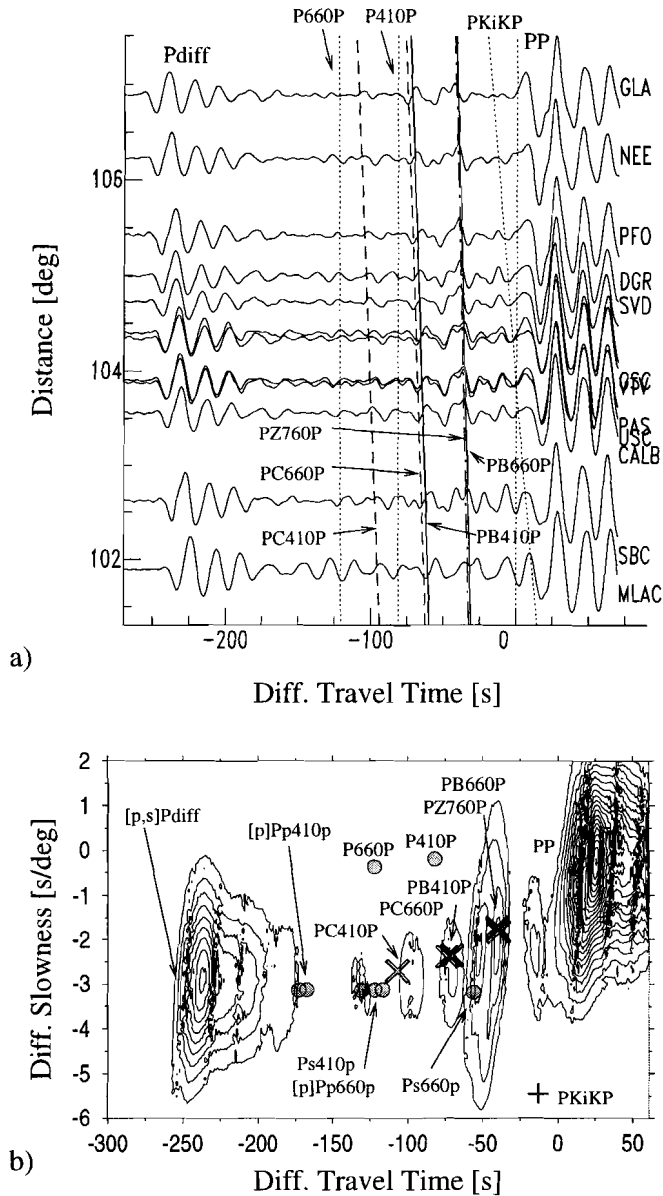


Figure 4.3. a) Band-passed (0.01 - 0.1 Hz) broadband recordings from stations in California for an event at the Philippines. b) Envelopes of phase weighted slant stack for the data from Figure 4.3a. Differential slowness is with respect to the PP phase.

precursors increases with time but remains far too low to mark a symmetrically reflected precursor such as *P410P*. Furthermore, the slowness is too large to explain the precursors as upper mantle reverberations.

Coherency and Ubiquity

The record sections and PWS's clearly reveal the presence of coherent seismic phases 100 s to 30 s before *PP*. Figure 4.2a already shows that similar precursors can be observed for different regions. Here we select for a comparison two unfiltered records which are from the stations BFO (Germany) and CCM (U.S.A.) for the event at the Marianas. The records were aligned with respect to the P_{diff} phase and shifted for a differential slowness of 0.4 s/deg. 0.4 s/deg is about the mean slowness of the precursory wave train (Figure 4.2b) and is applied to correct for the travel time move out of the precursors. The traces are shown in Figure 4.4. The epicentral distance and event azimuth are 107.8° and 331° for BFO (solid line), and 107.0° and 43° for CCM (dotted line). Both traces show a precursory wave train from about 1040 s to 1100 s. The onset of these wave trains are remarkably coherent. The length of the wave train and its amplitude compared to the surrounding coda show further similarities.

In Figure 4.5 we compare a record from BFO for the Marianas event with a record from GLA (U.S.A.) for the event at the Philippines. The epicentral distance and azimuth to station GLA are 106.9° and 49.6° , respectively. We can not expect waveform coherency since different events are used. Nevertheless, Figure 4.5 shows similar onset, length (1040–1100 s), and amplitudes of the unfiltered precursory wave trains for both events with different wave paths and stations. The traces from BFO and GLA are representative for the record sections from Figures 4.2 and 4.3 and consequently permit the conclusion that we are dealing here with the same type of phases. Together with Figure 4.2 it reinforces that there is no azimuthal or regional dependence in terms of precursor presence or absence.

At this point we can already exclude the explanation of a dipping reflector such as the boundary of a subducting slab. Such a scenario would yield the presence of precursors depending on the event-slab-station configuration. This is obviously not the case and is also confirmed by other record sections. Further, we can likely exclude that volumetric scatterers in the lithosphere and crust cause these arrivals. In such case we would expect to observe these precursors more intermittently and with less coherency in the shown record sections.

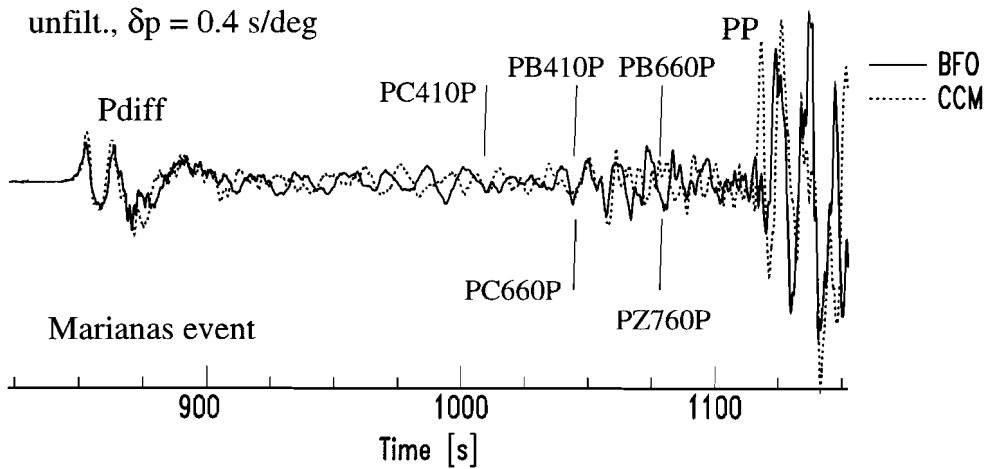


Figure 4.4. Traces from BFO (Black Forest Observatory, Germany) and CCM (Cathedral Caves, U.S.A.) are shifted with respect to the P_{diff} phase for slowness 0.4 s/deg. The traces are unfiltered. Note the coherent waveforms at about 1050 s and the similarity of the precursory wave train.

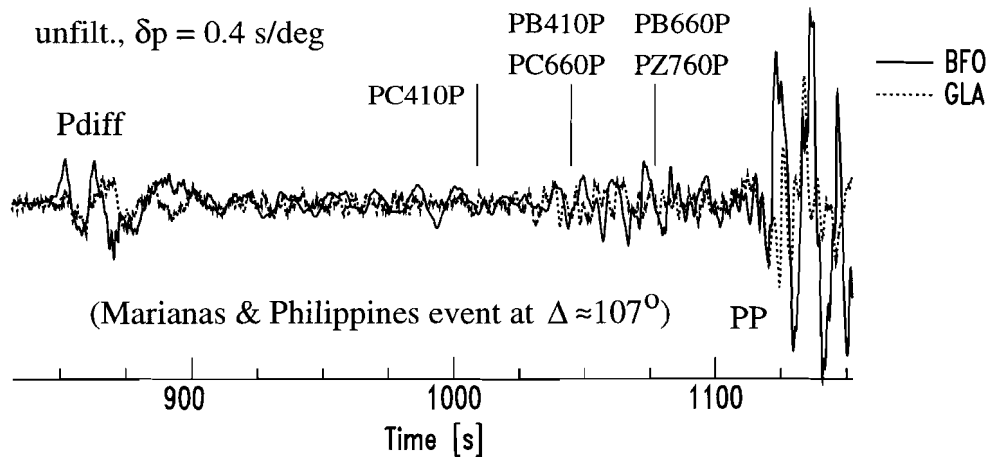


Figure 4.5. Traces from BFO (Black Forest Observatory, Germany) and GLA (Glamis, U.S.A.) are recordings from the Marianas and the Philippines event, respectively. The seismograms are unfiltered and shifted with respect to the P_{diff} phase for slowness 0.4 s/deg. Note that both records show a strong precursory wave train from about 1040 s to 1100 s.

4.2.3 SS Precursors

Here we consider transverse polarized seismograms which we obtained after rotating the horizontal components with respect to the great circle arc through source and receiver. We employ the same events as for the previous section. *SB410S*, *SC410S*, *SB660S*, *SC660S*, and *SZ660S* label the predicted asymmetrical precursors. We discuss them at a later stage.

The Record Sections

Figures 4.6a and 4.7a show the *S*-wave coda on the transverse components including the *SS* arrivals. The use of transverse components should simplify the search for *SS* precursors since a minimum of *P*-to-*S* converted phases is expected on these components. The data from Figure 4.6 are band-passed between 0.01 Hz and 0.07 Hz. Looking at the record from HRV (Harvard, Massachusetts, U.S.A.) we observe a ~ 70 s long precursory wave train which starts at -150 s. At slightly smaller distances a similar wave train is observed at RPN (Rapa Nui, Easter Island, Chile) and BFO (Schiltach, Germany). The later part of the precursory wave train can be easily traced back to smaller distances along the dashed and solid travel time curves. At the distance range from 85° to 92° a coherent long period wave train is visible at -50 s. It looks as if the precursory wave train at larger distances develops out of this coherent arrival. There is again a gap in time between the precursors and the *SS* phase at large distances. The *S*-wave coda seems to get less complicated with increasing distance. This can be explained by the more and more separated phases due to the different apparent velocities.

The record section of Figure 4.7 is band-passed between 0.01 Hz and 0.5 Hz. One clear arrival between the two solid travel time curves is visible. Note that all stations are located in the U.S.A. with exception of PAB (San Pablo, Spain), ESK (Eskdalemuir, Scotland, U.K.), and BORG (Borgarnes, Iceland).

The Slowness

Figures 4.6b and 4.7b show the contoured envelopes of the PWS (see corresponding section for *PP*) performed at different slownesses. For the slant stack from Figure 4.6b we used only the seismograms recorded at epicentral distances larger than 93° . This is done because the stacks are performed along straight travel time curves which approximate the true travel time curve within a small distance range only and secondly because the coda becomes more complicated with decreasing distances.

Both figures show one clear arrival or precursory cluster at about -70 s and around -3.5 s/deg. The slowness is too large to be a mantle reverberation and too small for a symmetrically reflected phase. *SS* precursors like *PKKS*, *PS*, *PPS* and *PSS* might contaminate the transverse components. In spite of considering this possibility we did not succeed in finding a phase which explains the precursors. All the core phases have slowness values which

Marianas, 1993 Aug 8, 12.98N, 144.80E, 59 km, 0.01 - 0.07 Hz

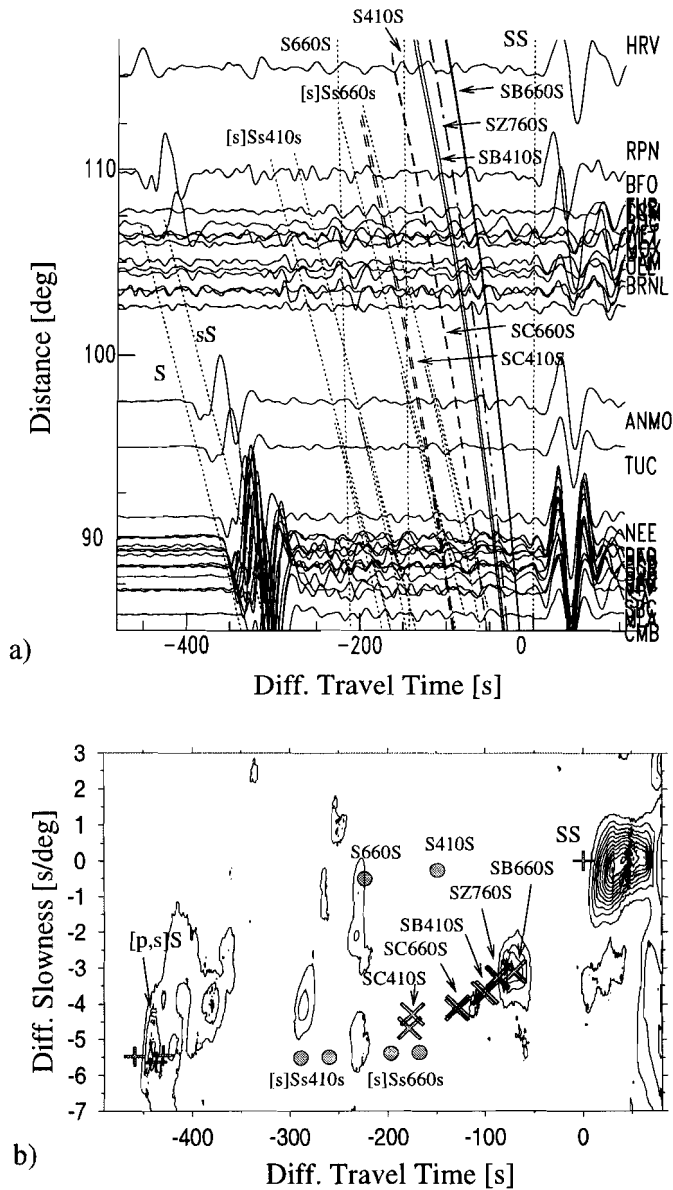


Figure 4.6. a) S-wave coda on band-passed (0.01 - 0.1 Hz) transverse recordings for the event from Figure 4.2. b) Phase weighted slant stacks of traces with distances greater than 93° .

Philippines, 1995 May 5, 12.63N, 125.20E, 16 km, 0.01 - 0.5 Hz

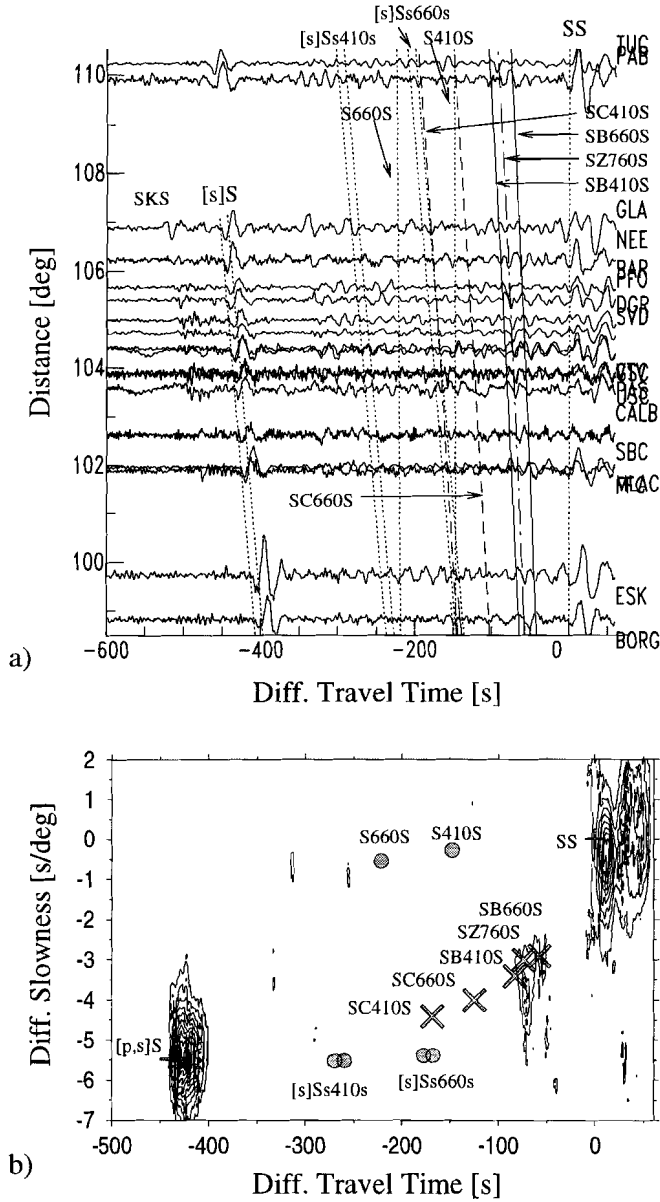


Figure 4.7. a) S-wave coda on band-passed (0.01 - 0.5 Hz) transverse recordings for the event from Figure 4.3. b) Corresponding phase weighted slant stacks.

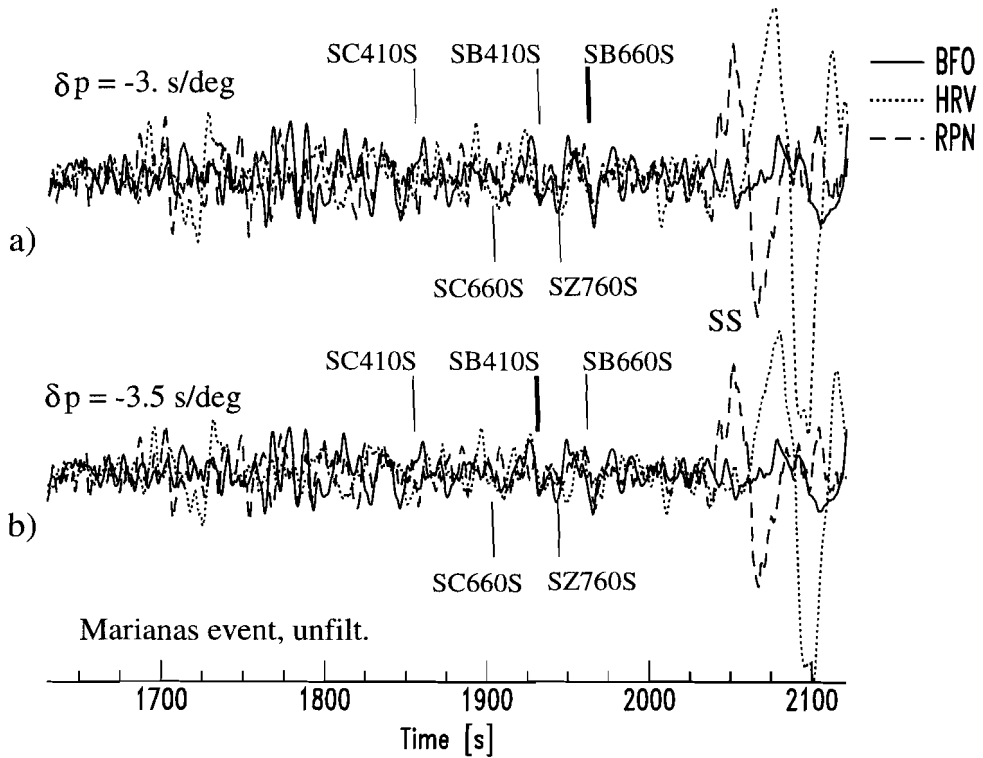


Figure 4.8. Traces from BFO (Black Forest Observatory, Germany), HRV (Harvard, U.S.A.) and RPN (Rapa Nui, Chile) are shifted with respect to SS on BFO for -3.0 s/deg (a) and -3.5 s/deg (b). The seismograms are unfiltered and show the precursors at about 1925 s–1975 s. a) SB660S is coherent on all three stations. b) SB410S is coherent on all three stations.

are far too small from those observed for the asymmetrically reflected precursors. PSS is a prominent phase which is coming closest in slowness and travel time to the precursors reported here. However, it arrives at 105° distance about -135 s earlier than the SS arrival with differential slowness -4.6 s/deg. It does not match the coherent precursors at about -70 s.

Coherency and Ubiquity

In Figure 4.8 we show three unfiltered records for the Marianas event. The corresponding stations are BFO (Germany), HRV (U.S.A.), and RPN (Easter Islands) with event distances and azimuths of 107.8° & 331° , 115.5° & 29° , and 109.8° & 114° , respectively. The traces are shifted for a differential slowness of -3.0 s/deg (4.8a) and -3.5 s/deg (4.8b) with

respect to the *SS* phase to obtain coherency of the precursory arrivals. Figure 4.8 shows the coherency of the precursory wave train between 1925 s (4.8b) and 1975 s (4.8a). Note that the slowness for the *SS* precursor wave train shows a similar behavior as that for the *PP* precursor wave train. The slowness increases for progressing travel time for both wave trains.

Although the waves sample very different regions these precursors seem to be remarkable coherent. Three-dimensional (3-D) structure such as scatterers and/or dipping interfaces are unlikely to cause such coherent arrivals.

4.3 Constraints on Precursor Generation

The previous section showed coherent *PP* and *SS* precursors which were recorded at different regions for different azimuths. Dipping reflectors (Figure 4.1a) and scattering at a heterogeneous lithosphere (Figure 4.1b) are therefore likely excluded to generate these precursors. Furthermore the obtained slowness values are far too small to constrain a symmetrical ray path and too large to explain the precursors as upper mantle reverberations (Figure 4.1c). This is the motivation to seek for an alternative scenario which can explain the observations.

4.3.1 Precursor Generation and Terminology

The generation of these precursors is discussed in detail in chapter 5. There we show that these precursors can be explained as non-geometrical arrivals which can be generated when a wave field has strong amplitude fluctuations along the Earth's surface. In a 1-D Earth strong amplitude fluctuations occur at the travel time reversals of triplications. The cartoon of Figure 4.9 pictures the generation of phases at the *B* and *C* points of a travel time triplication.

We calculate the travel time and slowness for phases which are generated by triplications of major upper mantle discontinuities, i.e. the 410-km and 660-km discontinuity. The results will be compared to the data. Note that we refer with slowness not to the ray parameter but to the slope of the travel time curve ($\partial T / \partial \Delta$).

In the following we use the terminology *Bd* and *Cd* to label the travel time reversals caused by a discontinuity at depth *d* (Figure 4.9). This notation has the advantage that it is unambiguous and easy to interpret. For instance *B410* corresponds to the ray which just turns above the 410-km discontinuity. *C410* corresponds to the critically reflected phase, or, alternatively the first ray which turns just below the discontinuity. The asymmetrically reflected phases which have one leg corresponding to these points are labeled *PBdP* or *PCdP* for *PP* precursors (Figure 4.9) or *SBdS* or *SCdS* for *SS* precursors. Consequently, *SC660S*

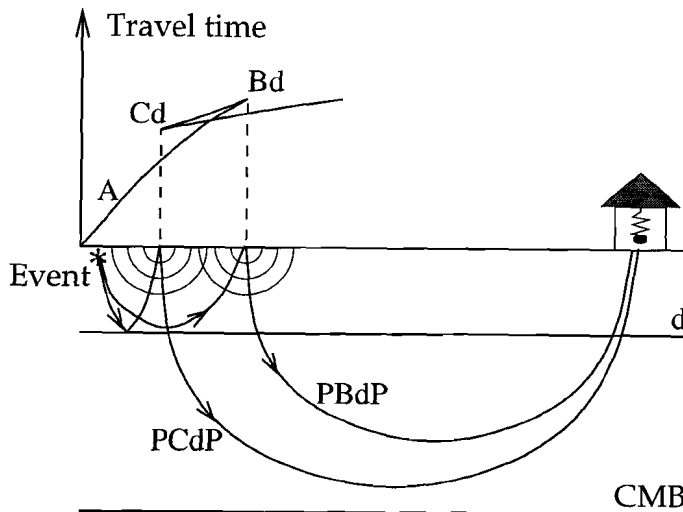


Figure 4.9. Cartoon showing a travel time triPLICATION caused by a discontinuity at depth d and generation of non-geometrical precursors (PBdP and PCdP) at the travel time reversals B_d and C_d.

corresponds to the asymmetrically reflected S phase caused by the amplitude fluctuation as a function of distance (or slowness) at C660.

Most Earth models have a decrease in velocity gradient at about 760 km depth. Such a discontinuity does not lead to a travel time triPLICATION, but causes amplitude fluctuations as a function of distance which can generate PP or SS precursors. Z760 is used to assign non-geometrical phases which are caused by this change in gradient. They are here included for completeness and will mostly be discussed in chapter 5.

4.3.2 Travel Time and Slowness

We compute the travel time and slowness of these non-geometrical phases and compare them to the observed precursors. Model ak135 (Kennett *et al.*, 1995) has been used as Earth model. The results are indicated in Figures 4.2 - 4.8. The record sections and slant stacks show that the coherent precursors coincide well with the predicted travel times and slownesses. PC410P, SC410S and SC660S are difficult to observe. The seismograms from Figure 4.3 show a coherent PC410P phase although much smaller than the other precursors. Such phase can only be detected by its coherency across an array of stations. The start of the larger amplitude precursory wave trains to the PP phase coincides with the PB410P and PC660P arrivals. These phases can not be resolved separately. However, the S -wave triPLICATION differs from the P -wave triPLICATIONs in such way that SC660S and SB410S do not interfere. In the S -wave coda SC660S is difficult to observe. One might therefore expect

that *PC660P* is small as well and that *PB410P* governs the onset of the precursory wave trains in the *P*-wave coda. In chapter 5 it is shown that it is indeed expected that *C* point phases are smaller in amplitude than *B* point phases. Thus the asymmetrically reflected precursors are dominated by phases which are generated at the *B* points of a travel time triplication.

The slant stacks show that the observed slowness increases within the wave train with progressing time as predicted (see crosses in Figures 4.2b, 4.3b). The observation of slowness increase has been reported by *Cleary et al.* [1975] for *PP* precursors. Figures 4.8a and b show that the slowness migrates similarly for *S*-waves. In Figure 4.8b *SB410S* is coherent at the predicted slowness and travel time, and in Figure 4.8a *SB660S* is. This similarity between *SS* and *PP* precursors as well as the correctly explained slowness and travel time supports that our observations with different wave types are related to each other.

Most Earth models predict a *PZ760P* and *SZ760S* phase. Such phases would interfere with the *PB660P* and *SB660S* arrivals, respectively. Consequently, no evidence for or against such phase (or change in gradient) can be given. It should be clear that other mantle discontinuities also might contribute to the precursory wave train with asymmetrically reflected precursors. Variations in the properties of the discontinuities will lead to incoherent precursors which we will not detect by our phase weighted stack.

4.4 Discussion

We observe asymmetrically reflected *PP* and *SS* precursors and show that their characteristics are similar to *PP* and *SS* precursors. Their travel time and slowness is explained by phases which are generated at the *B*- and *C*-points of the travel time triplications which correspond to the 410-km and 660-km discontinuity. The *B*-point phases have larger amplitudes than the *C*-point phases and consequently dominate the precursory wave trains.

The observation of asymmetrically reflected precursors is facilitated at the core shadow due to the fading out of the diffracted *P*- and *S*-waves and their related reverberations. Furthermore, it helps when the arrivals are more separated in time by their different apparent velocities. The presence of the core limits the asymmetrically reflected phases caused by upper mantle discontinuities to distances smaller roughly 120° . Indeed we best observed our phases in the 100° to 120° distance range. The observation of these precursors seems to be further controlled by the source mechanism. A source which radiates a large portion of energy into the upper mantle and less energy into the lowermost mantle will facilitate the identification of these phases. Under mentioned conditions the precursors seem to be a fundamental contributor to *P* and *S* coda waves. In the presented record sections they clearly govern the *PP* and *SS* precursory signal at the core shadow. At smaller distances other phases obscure their presence; together they build up a complicated coda.

Up to now asymmetrically reflected *PP* precursors have been observed and interpreted differently. Possible mechanisms (scattering, dipping reflector, mantle reverberations) are schematically sketched in Figure 4.1. The data presented here show coherent *PP* and *SS* precursors for different bounce point regions. This is difficult to explain by the scattering hypothesis (King *et al.*, 1975; Cleary *et al.*, 1975) and the reflection at a dipping interface (Wright and Muirhead, 1969; Wright, 1972; Weber and Wicks, 1996). In fact the recordings from the GRSN stations in Figure 4.2a have been interpreted as a reflection from a distant subduction zone (at Japan about 20° from the event at the Marianas) by Weber and Wicks [1996] but the more global record section from Figure 4.2a (and Figures 4.4, 4.5) favors an alternative scenario. The GRSN data may surely be affected by the subduction zone at the bounce point (Japan), but the traces from station SPA (Antarctica) and CCM (U.S.A) in Figure 4.2a indicate that globally coherent effects dominate the *PP* precursory wave train. The *S*-wave record section (Figure 4.6a) for same event as well as the record sections of other events such as those shown in Figures 4.3a and 4.7a strengthen our hypothesis. Conversions and/or reflections at the boundary of a slab can indeed strongly contribute to the *P*-wave coda within the core shadow as was shown by Souriau [1988] for a case study of Chilean earthquakes. These phases were visible for a small range of event-station azimuths only. They appear too early and with slowness values which are too small to be explained by our generation mechanism.

The mantle reverberations suggested by Husebye and Madariaga [1970] and Ward [1978] are without any doubt also contributors to the *P*- and *S*-wave coda (within the core shadow). For instance the slant stack of Figure 4.2 shows clearly the presence of diffracted mantle reverberations such as $[p]Pp410p$, $Ps410p$, and $[p]Pp660p$. They can be seen in the data where they have the same slope (slowness) as P_{diff} , they may interfere with possible $P660P$ arrivals. The slowness values of what we call asymmetrically reflected precursors are systematically too large to be explained by reverberations at prominent mantle discontinuities. Higher order reverberations are rejected since they have much smaller amplitudes due to the repeatedly experienced low conversion/reflection coefficients. Further, the *SS* precursors on the transverse components can not be explained by radially polarized *P*-to-*S* conversions. A possible contamination would have relative small amplitudes and a slowness which is too small and not so coherent in amplitude.

The variety of phases which are present in the coda of *P* or *S* show that convincing interpretations rely on the combination of slowness, travel time and spatial coherency. Wajeman [1988], Petersen *et al.* [1993], Estabrook and Kind [1996] among many others identify symmetrically reflected *PP* or *SS* precursors such as $P660P$ and $S660S$ by their correct slowness. The ISC data set contains a relative large number of *PP* precursors at epicentral distances ranging from 90° to 115° . Because these data have the travel time information only, there are many ways to explain them. Kato and Hirahara [1991] investigated these precursors by their distribution as function of lead time and distance. The

travel time curves of our predicted asymmetrically reflected precursors match their clouds of reported precursors well.

Although we show positive observations and stacks, these precursors do not show up in the global stacks such as performed by *Shearer* [1991] for *PP* and *SS* or *Estabrook and Kind* [1996] for *PP*. It is difficult to trace back the cause of this due to their prestack processing. Seismograms like those shown in Figure 4.3a would be discarded by *Shearer* [1991] due to his signal-to-noise (S/N) threshold. *Shearer* [1996] presents an *SS* stack which basically differs from *Shearer* [1991] by using oceanic bounce points only and a normalization which favors the observation of *SdS* phases. A hint of asymmetrically reflected precursors is visible in his Plate 1.

Estabrook and Kind [1996] apply a source equalization by deconvolving the *PP* waveform prior stacking. For instance different thickness of the crust at the bounce point reflects into a different waveform (*Paulssen and Stutzmann*, 1996; *Shearer*, 1996) and consequently source equalization. This could decrease the waveform coherency of asymmetrically reflected precursors and lead to a less efficient stack.

The sensitivity of *PP* (*SS*) phases and precursors to changes in source depth and -radiation, and 1-D and/or 3-D structure seems to differ significantly which means that event-stacks with *PP* (or *SS*) alignment further could lead to incoherent summation of asymmetrical precursors.

4.5 Conclusions

We show asymmetrically reflected *PP* and *SS* precursors which seem to be independent of azimuth and region. The *PP* and *SS* precursory wave trains experience a similar slowness migration with time. Their ubiquity, coherence, slowness and travel time are not explained by underside reflections at dipping interfaces, random scattering at a heterogeneous lithosphere, or geometrical mantle reverberations. Slowness and travel time are well explained by phases which are generated at the *B*- and *C*-points of the upper mantle travel time triplications. The following chapter shows that these phases are non-geometrical phases which can even be generated in a 1-D Earth. This explains the observed ubiquity and coherence. The strong *PP* and *SS* precursors are consistently well predicted with travel time and slowness for phases which are generated at the *Bd* points. The *C*-point arrivals are weak and difficult to observe.

The observation of clear precursors is favored at the core shadow where other coda waves are weakened due to diffractions at the core. Similarly the core limits the observation of these precursors to an epicentral distance of about 120° . It seems that these precursors are fundamental contributors of *P*- and *S*-coda waves. Together with other phases such as scattered waves, reflections at dipping interfaces, mantle reverberations, and symmetrically reflected precursors they produce a complex coda between *P* and *PP* (*S* and *SS*). Conse-

quently, the interpretation of other precursors such as *PdP* and *SdS* type phases must rely on their coherency and slowness measurements. The observation of asymmetrically reflected precursors may be used for global investigations of upper mantle discontinuities.

Chapter 5

Asymmetrically Reflected PP and SS Precursors: 2. A Mechanism to Generate Non-Stationary Arrivals

Abstract. A study of the characteristics and generation of asymmetrically reflected precursors to *PP* and *SS* is presented in two chapters of this thesis. The previous chapter (4) presents observations of asymmetrically reflected precursors which are difficult to explain by previously proposed mechanisms and which motivate the proposition of a new mechanism. We suggest that the *PP* and *SS* precursory wave trains are predominantly generated by fluctuations in the amplitude and phase of the wave field due to the upper mantle triplications. The generation occurs when this wave field interacts with the Earth's surface to generate the second leg of a *PP* or *SS* arrival. The precursors are non-geometrical arrivals, and Huygens' principle and a Kirchhoff-Helmholtz related theory are used to stepwise picture their generation. Synthetic seismograms are calculated which only qualitatively can be interpreted due to the high frequency approximation of the ray theory used and due to the omission of reflected waves and head waves. The proposed mechanism only requires a depth dependent (1-D) velocity profile and can therefore explain the ubiquity and coherency of the precursors. The theoretical travel times and slownesses coincide with those measured values for *PP* and *SS* precursors in chapter 4. The presence of effects of lateral heterogeneities is not excluded and these can even strengthen the precursors. These non-geometrical arrivals thus seem to be a fundamental contributor to coda waves. To our knowledge the non-geometrical arrivals proposed here have been overlooked up till now.

A slightly changed version of this chapter is submitted for publication as: Schimmel, M. & H. Paulssen, Asymmetrically reflected PP and SS precursors: 2. A mechanism to generate non-stationary arrivals, *submitted to J. Geophys. Res.*, 1997.

5.1 Introduction

This chapter studies the characteristics and generation of asymmetrically reflected *PP* and *SS* precursors. The observational aspects such as slowness, coherency and ubiquity are presented in chapter 4. Asymmetrically reflected precursors to *PP* (*Wright and Muirhead*, 1969; *Husebye and Madariaga*, 1970; *Wright*, 1972; *Cleary et al.*, 1975; *King et al.*, 1975; *Ward*, 1978; *Kato and Hirahara*, 1991; *Weber and Wicks*, 1996, among others) are known since long time and have led to different explanations. Conversely, *SS* precursors are reported only recently (chapter 4 of this thesis). In the previous chapter we show that they can be observed similarly to *PP* precursors at distances ranging from 80° to 120° . *PP* and *SS* precursor wave trains have slowness values which increase with progressing time and which constrain an asymmetrical ray path. The precursors seem to be ubiquitous, i.e. no azimuthal or regional dependence is found. They can even be coherent at different stations with very different azimuth.

So far the asymmetrically reflected arrivals were explained by underside reflections at dipping interfaces (4° - 15°) at about 20° distance from the source or receiver (*Wright and Muirhead*, 1969; *Wright*, 1972; *Weber and Wicks*, 1996), by mantle conversions and reverberations (*Husebye and Madariaga*, 1970; *Ward*, 1978) or by scattering at small scale (~ 10 km) heterogeneities in the uppermost mantle and crust (*Cleary et al.*, 1975; *King et al.*, 1975; *Kato and Hirahara*, 1991). *Cleary et al.* [1975] and *King et al.* [1975] show that the scattering mechanism can explain the ubiquity, slowness, and envelope of high-frequency precursory wave trains. However, at lower frequencies coherent precursors are reported which are difficult to explain by random scattering. Mantle reverberations and conversions explain coherency and ubiquity, but not the slowness of precursors which are observed up to distances of 120° . Conversely, reflections at dipping interfaces can explain the slowness but not the ubiquity. This motivates to find a more satisfying explanation of the presence of asymmetrical precursors.

Here we propose a new generation mechanism which can explain the observations. It will be explained and discussed on the base of Huygens' principle. This principle asserts that points which are disturbed by an incoming wave act as a new set of radiating sources. It implies that the wave disturbance spreads out through every possible path building up a new wave. This can result in geometrical (stationary) and non-geometrical (non-stationary) arrivals even within a one-dimensional (1-D) Earth. Ray amplitudes are used to picture their generation and to calculate synthetic seismograms with a Kirchhoff-Helmholtz related theory after *Frazer and Sen* [1985] and *Frazer* [1987]. Some aspects of this theory are discussed in an appendix. Throughout this chapter we use the term slowness not to refer to the ray parameter but to the slope ($\partial T/\partial \Delta$) of the travel time distance ($T - \Delta$) curve. The ray parameter generally differs from the derivative ($\partial T/\partial \Delta$).

5.2 Theory and Explanation

A Kirchhoff-Helmholtz -related method after *Frazer and Sen* [1985] and *Frazer* [1987] was used to interpret the *PP* and *SS* precursors. This method combines Huygens' principle and ray theory (see Appendix on page 85). The idea is that asymmetrically reflected *PP* (and *SS*) precursors may be modeled by a series of Huygens' sources at the free surface which are generated by primary *P*-waves (*S*-waves) and which contribute to the *PP* (*SS*) wave field at the receiver. Geometrical optics is applied to approximate wave propagation from the event to the surface and from each generated elementary source to the receiver. This method is well suited for our purpose since it follows Huygens' principle which allows to include non-geometrical phenomena such as diffractions. The method has been already successfully applied to model underside reflected *PdP*-type arrivals by *Neele and Snieder* [1992], and *Neele et al.* [1997]. The latter paper clearly shows the importance of using a method which considers the whole saddle shaped *PP* (or *SS*) Fresnel zone to synthesize *PP* or *SS* type arrivals rather than one geometrical ray. We use the single fold representation (*Frazer and Sen*, 1985) which means that a single integration is performed. In this case the surface of integration is the Earth surface. Figure 5.1 schematically sketches the approach.

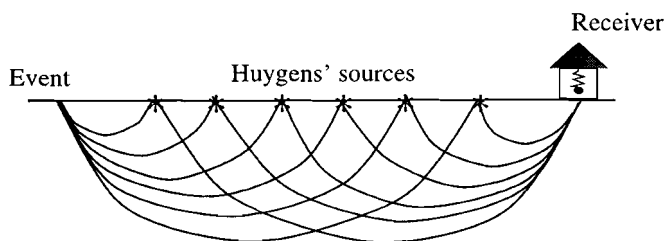


Figure 5.1. This cartoon pictures the approach which is used to model and understand the generation of *PP* (*SS*) type arrivals. All the rays with bounce point at the Earth surface contribute to the displacement field at the receiver.

Note that the surface of integration can not arbitrarily be chosen when non-geometrical phenomena are investigated (see Appendix). The models used in this chapter ensure that no caustics occur on the surface of integration, i.e. they prevent that the integration becomes singular. A drawback of the Kirchhoff-Helmholtz related method is the use of ray geometrical amplitudes which are frequency independent and accurate at high frequencies only. Therefore our synthetics are only used for qualitative comparisons.

To understand our interpretation of the asymmetrically reflected precursors we start with Huygens' principle and introduce geometrical and non-geometrical arrivals. Due to the direct connection with the stationary phase method we call these arrivals also stationary and non-stationary arrivals.

5.2.1 Stationary and Non-Stationary Arrivals

Most well-known arrivals propagate from source to receiver along paths that are extremal in travel time, i.e. the travel time is stationary for perturbations in the ray trajectory. In other words the ray path is determined by the places where the elementary waves, such as proposed by Huygens' principle, interfere constructively. This is Fermat's principle. Snell's law of reflection and refraction is, for instance, a result of this principle. Arrivals obeying Fermat's rule throughout the whole ray path are thus called stationary. The so-called method of stationary phase (e.g. *Bleistein* [1984]) follows the same principle to approximate the integration of complex functions with slowly varying amplitude functions and with phase functions which contain at least one stationary point. The stationary point is where the first derivative of the phase function becomes zero and at this point complete constructive interference occurs. This can be pictured by considering the summation of complex numbers as the summation of vectors which are defined in a complex plane by a phase and amplitude. The vectors with same or similar phase sum up constructively. Further away from the stationary point the integrand gets more and more oscillatory. Consequently, the integration over those regions cancels whenever the amplitude function is smooth. Thus the gross contribution to the integration comes from the points at and around the stationary point. The wave analogy is that this stationary solution corresponds to the ray following Fermat's principle and its first two-dimensional (2-D) Fresnel zone at the bounce point. The smooth amplitude function guarantees that there are no contributions from remote points to the integration. On the other hand a delta pulse superimposed on the smooth amplitude function far away from the stationary point will also give a contribution to the integration since the points at the vicinity can not achieve the destructive interference of the delta pulse. In this case we have a stationary and, say, a non-stationary contribution of the integrand.

In Figure 5.2 we consider the integration

$$u(\omega) = \int_{-\infty}^{\infty} A(x)e^{i\phi(\omega,x)} dx \quad (5.1)$$

with hypothetical amplitude $A(x)$ (Figure 5.2a) and phase $\phi(\omega, x)$ at a high and low angular frequency ω (Figures 5.2b and c). Due to the 2π -periodicity of the harmonic function $\exp i\phi(\omega, x)$ the phase function is wrapped between π and $-\pi$. We have constructive interference at the stationary point x_0 , but we also have a net contribution to the integrand due to the abrupt amplitude fluctuations at x_1 and x_2 . At high frequencies (Figure 5.2b) there are no contributions from the region between x_1 and x_2 due to the highly oscillating phase function and constant amplitude. Conversely, at low frequencies (Figure 5.2c) the entire region from x_1 to x_2 will influence the integration since the phase function does not permit complete destructive interference. This contribution will increase the smaller the phase variation becomes. We like to add that the same principles show that non-stationary contributions are expected for discontinuities in the phase functions.

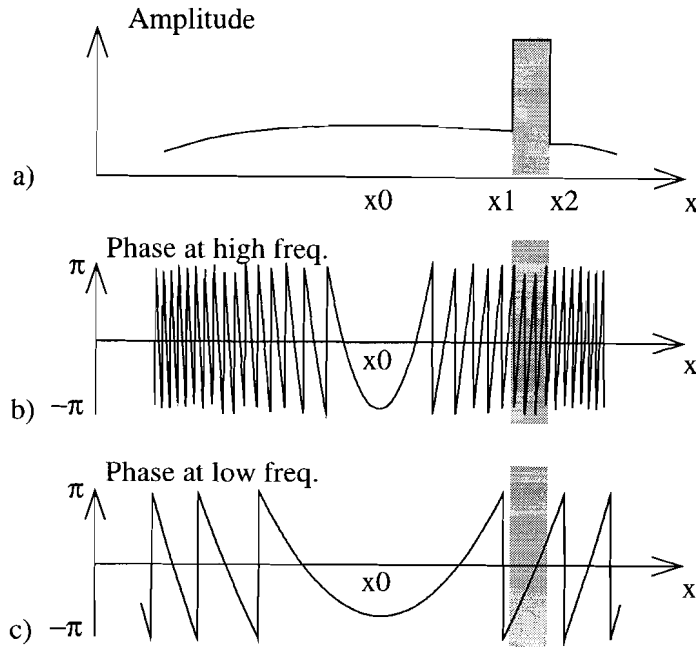


Figure 5.2. Hypothetical amplitude (a) and phase function at high (b) and low (c) frequency as function of x . x_0 marks the stationary point and x_1 and x_2 the locations of rapid amplitude fluctuation.

The calculation of the *PP* (*SS*) wave field following the configuration of Figure 5.1 leads to a similar integral as equation 5.1 where the right hand side is multiplied by $i\omega$ (see equation (A.3) in the appendix). The factor $i\omega$ counteracts the increasing contribution of amplitude fluctuations, such as shown in Figure 5.2a, at decreasing frequency. In the Kirchhoff-Helmholtz approach the integrand of equation (5.1) ($A(x) \exp i\phi(\omega, x)$) corresponds to the rays depicted in Figure 5.1 where x is the bounce point position at the Earth's surface. The amplitude $A(x)$ contains the geometrical spreading of the rays from the source to the bounce point, from the receiver to the bounce point, and a generalized reflection coefficient which connects the rays from the receiver and source at the bounce point. The phase function is obtained by multiplying the travel time of each ray with the angular frequency ω . The stationary point x_0 corresponds to the bounce point of the geometrical ray. Strong amplitude fluctuations, such as shown in Figure 5.2a, contribute to the displacement field at the receiver. In this example the non-stationary arrivals would have an asymmetrical ray path corresponding to the bounce points at x_1 and x_2 . Strong amplitude fluctuations can be caused by heterogeneities along the ray path. However, in the following we show that these non-stationary arrivals can even be generated within a spherically symmetric Earth.

5.2.2 Travel Time Tripletions

In a realistic 1-D Earth, discontinuities in velocity or velocity gradient are obvious sources of strong variations in the amplitude functions. These are places where travel time tripletions may develop. First we discuss the amplitude and travel time tripletion of the direct P -wave (S -wave) arrivals and then show their consequences for PP (SS) type arrivals. We make use of ray geometric amplitudes which only approximate the true amplitudes at high frequencies. However, our purpose here is to outline the principles and these are not expected to change for low frequencies.

In Figure 5.3 we schematically show four examples of velocity-depth profiles $v(z)$, their corresponding slowness-distance ($p - \Delta$) curves, and the derivatives $\partial\Delta/\partial p$ as a function of slowness. The wave amplitude predicted by ray theory is proportional to $(\partial\Delta/\partial p)^{-0.5}$. Consequently, caustics are obtained for $\partial\Delta/\partial p = 0$. Travel time tripletions occur for the profiles shown in Figure 5.3a-c. We see that caustics are not present for every velocity profile. For instance no caustic develops for the velocity profile of Figure 5.3c. However, due to kinks in the ($p - \Delta$) curve the derivatives $\partial\Delta/\partial p$ and consequently the ray amplitudes are discontinuous. The velocity-depth profile of Figure 5.3d shows a discontinuity in the velocity gradient. The gradient decreases which causes less rays to turn. No tripletion develops and the ray which turns precisely at the interface between the two layers with different velocity gradient has zero amplitude (*Chapman, 1971*). This is visible in the derivative $\partial\Delta/\partial p$ which goes towards $-\infty$ (Figure 5.3d) for the corresponding slowness. The four examples of Figure 5.3 show amplitude fluctuations which – following the argumentation of previous section – should result in the occurrence of non-stationary arrivals.

We use the terminology Bd , Cd and Zd to label the positions on a travel time or amplitude curve which are caused by a discontinuity at depth d . Bd and Cd are used for the travel time reversals of tripletions (see upper part of Figure 5.4) and Zd is used for a point which corresponds to a decrease in velocity gradient without creating a travel time tripletion (Figure 5.3d). This notation is unambiguous and easy to interpret. For instance $B410$ and $C410$ correspond to the rays which just turn above and below the 410-km discontinuity, respectively.

The lower left part of Figure 5.4 schematically shows the generation of non-stationary and stationary arrivals for rays which turn between 410 km and 660 km depth. Huygens' waves which are generated at the Earth surface between points which correspond to $C410$ and $B660$ on the travel time curve build up a stationary reflected wave front. The amplitude curve as function of reflection point at the free surface changes rapidly at $C410$ and $B660$. Precritical reflections are omitted in the cartoon of Figure 5.4. They approach the critical point $C410$ ($C660$) from smaller epicentral distances with amplitudes which are extremal at the C -points. In addition the phase function at $C410$ and $B660$ is discontinuous with respect to the critically reflected arrivals which experience a phase shift of $\frac{\pi}{2}$. The generated

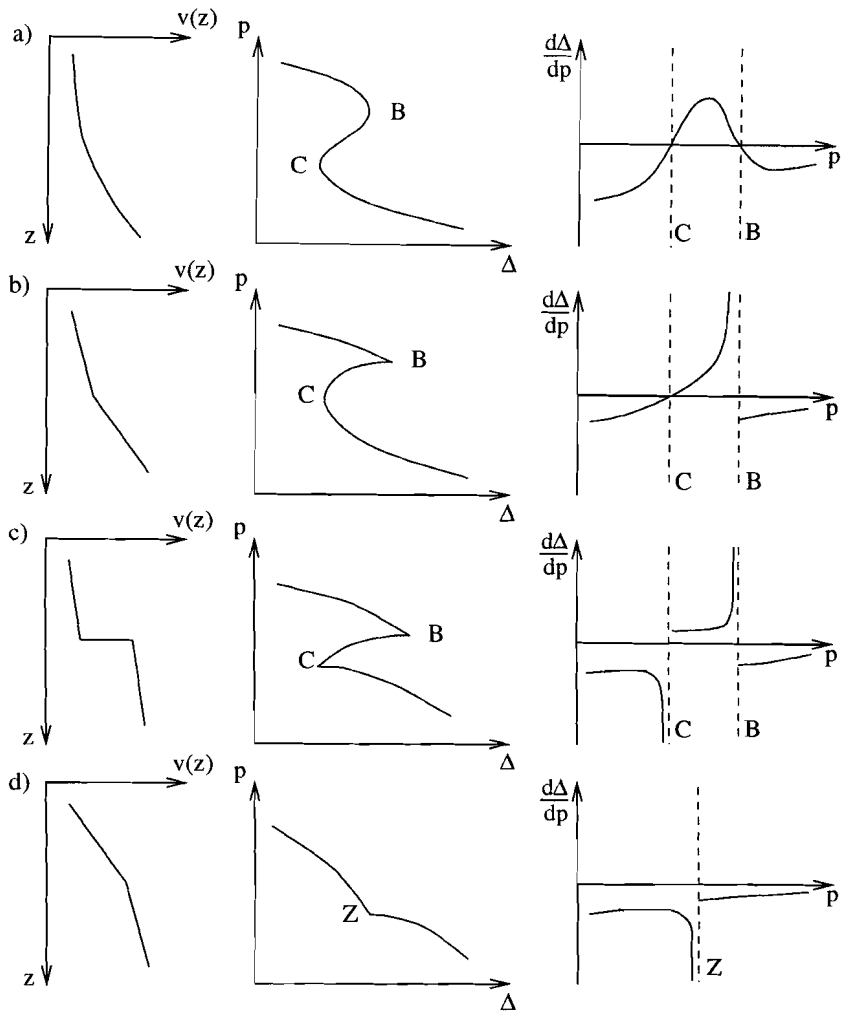


Figure 5.3. Four velocity-depth profiles (left column) with corresponding slowness-distance curve (middle column) and derivatives $\partial\Delta/\partial p$ as function of slowness (right column). Cartoons are freely sketched after Aki and Richards [1980] and Bullen and Bolt [1985]. B and C refer to the right and left reversals in the travel time triplication. Z is used when no triplication develops.

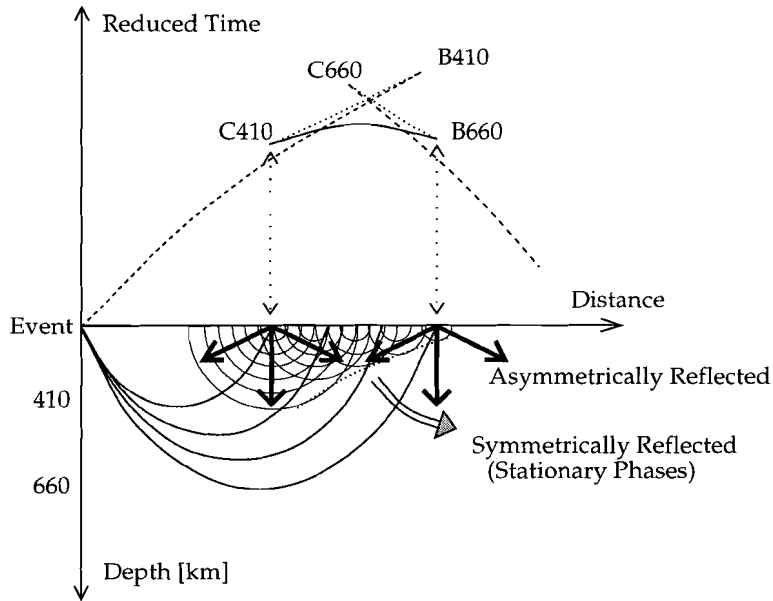


Figure 5.4. Travel time triplication caused by the 410-km and 660-km discontinuity. Solid curve corresponds to rays which turn between both discontinuities. They generate the secondary sources which are schematically sketched. The wave field develops symmetrically and asymmetrically reflected arrivals.

non-stationary arrivals resemble diffractions as they would occur at the edge of a spatially limited reflector. However, the 'diffractions' discussed here are not due to lateral variations in the medium. In the following section it is shown what the consequences for the *PP* and *SS* wave field are.

5.2.3 Amplitude Functions for *PP* and *SS* Type Arrivals in a Spherically Symmetrical Earth

Following Huygens' principle *PP* (*SS*) arrivals can be obtained by adding the contributions of the waves generated at the Earth's surface by the primary *P*-wave (*S*-wave) arrivals. Figure 5.5c schematically shows rays in a model which has discontinuities in velocity at 410 km and 660 km depth. These rays are grouped into three classes of *PP*-type rays which are indicated by different line styles. The solid curves have two turning points below the 660-km discontinuity. The dashed curves represent waves which turn once between the 410-km and 660-km discontinuity and once below the 660-km discontinuity. Lastly, the dotted curves have one turning point above the 410-km and one below the 660-km discontinuity.

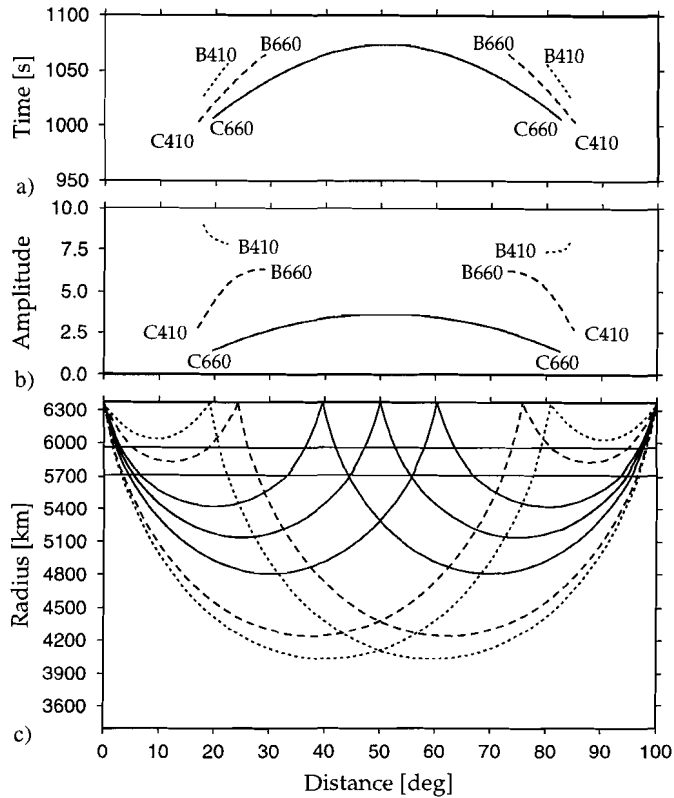


Figure 5.5. a) Travel time and b) amplitude of *PP*-type rays as function of bounce point position along the minor arc between source and receiver. c) Representative rays which build up the *PP* arrival. The line style relates the different curves to each other. Dashed and dotted travel time curves in a) are shifted by 20 s and 40 s, respectively. Reflected waves and head waves are omitted.

Only turning rays below 250 km depth are included, i.e. the rays reflected from the upper mantle discontinuities are omitted. Figures 5.5a,b show the corresponding travel time and amplitude as function of bounce point position of rays similar to those depicted in Figure 5.5c. The curves with different line style relate to each other. For visual reasons 20 s and 40 s have been added in Figure 5.5a to the travel time branches with dashed and dotted line style, respectively.

Note that the travel time is maximum in the direction between source and receiver for the geometrical *PP* (*SS*) ray. In Figure 5.5c it is the ray with bounce point at 50°. Rays with bounce points in the vicinity of the geometrical bounce points are required to describe the wave field at finite frequencies as these all contribute to the *PP* (*SS*) waveform and their importance is shown by Neele *et al.* [1997]. The strength of each contribution to the

PP arrival at the receiver is calculated by taking into account the amplitude of the direct *P*-wave from the source to the bounce point at the Earth surface, the generalized reflection coefficient (Frazer and Sen, [1985]; Frazer, [1987]), and the geometrical spreading of the ray between bounce point and receiver. This gives the amplitude function which is shown in Figure 5.5b and which is utilized throughout this section.

The start and end points of the travel time and amplitude curves are labeled according to the travel time triplication at the source- or receiver-side. Including the *BC*-branches would yield continuous travel time curves, however, the amplitude and phase function remain discontinuous or rough as shown in previous section. The amplitude function does not vary smoothly at the *Bd* and *Cd* points which implies that the integrand does not integrate to zero, yielding the proposed non-stationary arrivals. We will later show that our observations are related to these phenomena.

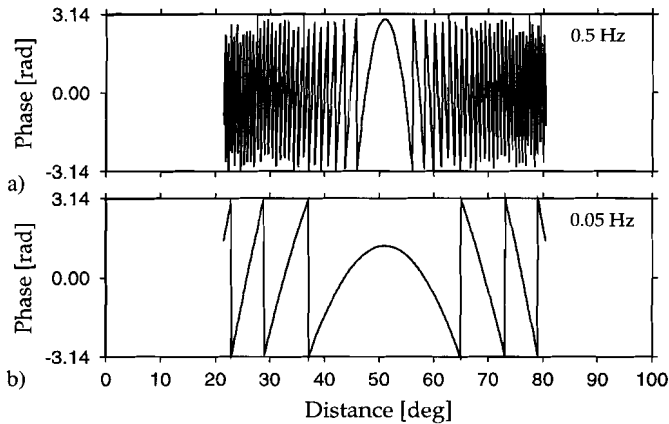


Figure 5.6. The phase of *PP*-type rays as function of bounce point along the minor arc between source and receiver at a) 0.5 Hz, b) 0.05 Hz for rays which turn below 660 km depth.

In Figure 5.6 we show the phase as function of bounce point position for rays turning in the lower mantle (solid curves in Figure 5.5) at two different frequencies. At both frequencies the stationary arrival is predicted for the geometrical *PP* ray with bounce point at 50° . At 0.05 Hz (Figure 5.6b) the wavelength of the oscillating phase is almost 10° . This permits the generation of non-stationary arrivals due to amplitude fluctuations similar as for Figure 5.2c. The amplitude fluctuations can be much smoother for low frequencies than required for high frequencies to generate non-stationary arrivals. At decreasing frequencies the wavelength of the oscillating phase function increases and there are even no oscillations at very low frequencies. In fact we can not anymore separate stationary and non-stationary solutions at very low frequencies.

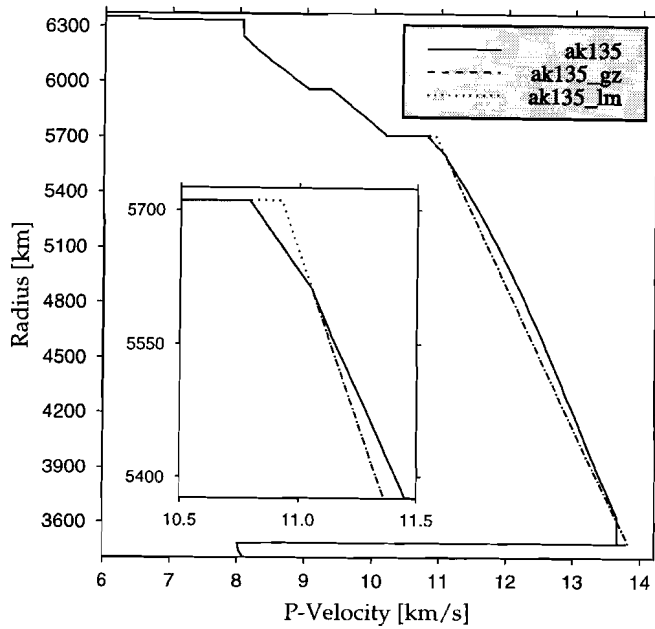


Figure 5.7. *P*-velocity profile of model ak135 (Kennett *et al.*, 1995) and two simplified models with one (ak135_lm) or two (ak135_gz) layers of constant velocity gradient in the lower mantle.

The calculations for Figure 5.5 are performed in a simplified model of ak135 (Kennett *et al.*, 1995) named ak135_lm (see Figure 5.7). It has a constant velocity gradient below 660 km depth. However, many Earth models contain a pronounced change in *P* and *S* velocity gradient at approximately 760 km depth such as the *P*-velocity profile of ak135 (Kennett *et al.*, 1995) shown in Figure 5.7. Model ak135_gz (Figure 5.7) was constructed to investigate the influence of such discontinuity. It has two layers of constant velocity gradient below 660 km depth with a discontinuous velocity gradient at 760 km. In Figure 5.8 we compare the amplitude functions for rays which turn below 660 km in the models ak135_lm (dashed curve) and ak135_gz (solid curve). In the comparison we see the effect of the gradient change at 760 km depth. *Z760* is used to label the strong amplitude variation caused by the gradient change at 760 km. In fact at *Z760* the *PP* (*SS*) ray geometrical amplitude function is expected to have zero amplitude. This is because the ray turning precisely at the interface between the two layers with different velocity gradient has zero amplitude (see Figure 5.3d or Chapman [1971]). Discrete sampling of the surface integration causes the amplitude at *Z760* to deviate from zero.

Up to now we have only considered contributions from bounce points between source and receiver. However, there are also contributions from bounce points out of this direction.

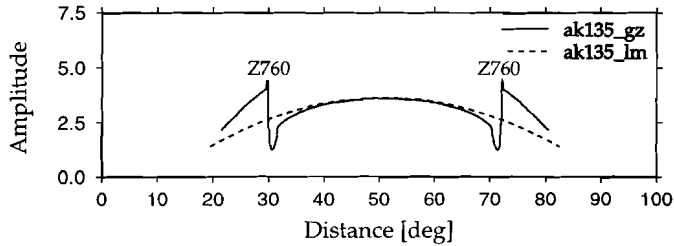


Figure 5.8. Amplitude of PP-type rays as function of bounce point along the minor arc between source and receiver for the two simplified models from Figure 5.7. Considered are rays which turn below the 660-km discontinuity. Z760 marks the amplitude fluctuation which is caused by the discontinuity in 760 km depth in model ak135_gz. Discrete sampling of rays is the reason why the amplitude does not reach zero at Z760.

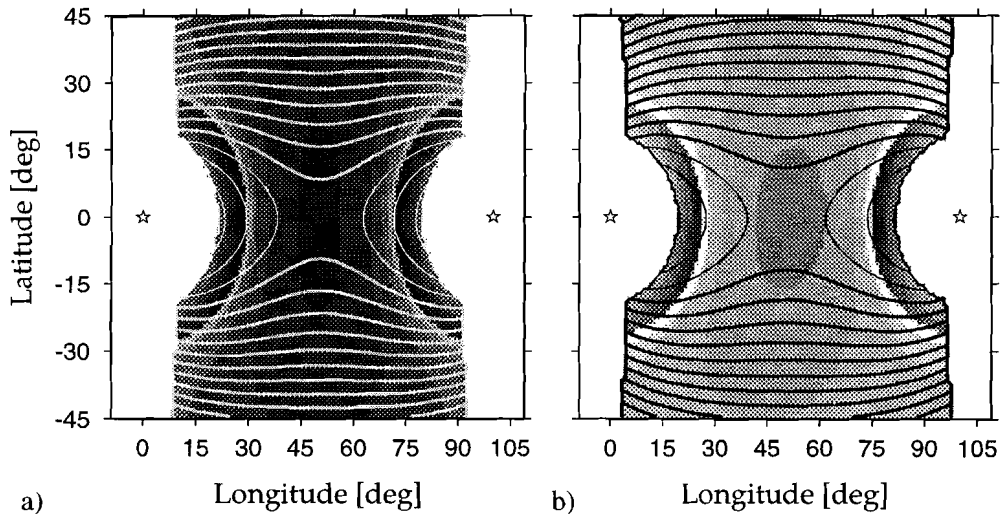


Figure 5.9. Contoured amplitudes (grey tones) and travel times (lines) as function of bounce points for PP- (a) and SS-type (b) rays for model ak135. Black correspond to maximum amplitude. Stars mark source and receiver position. Model used is ak135. All rays turn below the 660-km discontinuity. The thick lines contour travel times which are larger than the travel time of the geometrical arrival.

In Figure 5.9 we show the contribution of the amplitudes (grey tones) and travel times (black or white lines) of the *PP* arrival (5.9a) and *SS* arrival (5.9b) as a function of bounce point position at the Earth's surface. Only the contributions from rays turning in the lower mantle are depicted in this figure for a model with a gradient at 760 km depth. The travel time curves show the well-known saddle shape: maximum in the direction between source and receiver, and minimum in the direction perpendicular to that. Thick lines mark the travel time contours which are larger than the travel time of the geometrical arrival.

The circular shaped edges of the contoured surface (Figure 5.9) at the station and receiver correspond to rays which turn just below the 660-km discontinuity. They correspond to the *C660* points as shown in Figure 5.5a and b for the minor arc between source and station. The effect of the change in gradient at 760 km depth appears as the circular change from high to low amplitudes at a distance of about 30° from source and receiver. The change in gradient at 760 km in ak135 is larger for *S*-waves than for *P*-waves which results in a larger amplitude fluctuation for *S*-waves (see Figure 5.9). Consequently, we expect that precursors caused by the 760 km discontinuity are larger for *S* than *P* waves.

Integration of all the contributions will give the *PP* (*SS*) arrival and the non-stationary arrivals. At high frequencies one can split the integration into a sum of integrations over separate regions where no destructive interference is achieved. Take for instance the circular change from high to low amplitudes due to the gradient change at 760 km depth (Figure 5.9). The integration over this region has a stationary solution with the stationary point where the travel time curve becomes minimal. This happens at the intersection with the minor arc through source and receiver. This is the reason why these asymmetrically reflected arrivals are precursors to *PP* (*SS*). The precursors which were non-stationary arrivals for bounce points along the great circle arc become stationary due to the contributions of the additional dimension. In fact one might call these non-geometrical minimum travel time arrivals.

5.2.4 Synthetic Modeling of Stationary and Non-Stationary Arrivals

Until now we only considered the amplitude and travel time of each ray which contributes to the total wave field at the receiver. Now we can calculate the wave field by the summation over all rays. The Kirchhoff-Helmholtz theory after *Frazer and Sen* [1985] and *Frazer* [1987] is the back-bone of this integration where the Earth's surface is taken as the surface of integration. The integration (equation (A.3) in appendix) is realized by the summation over all rays without any special treatment such as tapering of the amplitudes at the *B*- and *C*-points. Note that the contributions of reflected waves and head waves at the discontinuities are omitted. This and the frequency independent ray amplitudes lead to inexact seismograms. Nevertheless, we do not refrain from calculating seismograms since it completes the principles of the generation which are presented here. Due to the omission of the reflections, the generation of *B*- and *C*-point arrivals resembles the generation of 'cut-off' arrivals which appear in many approaches when the integrations over slowness or

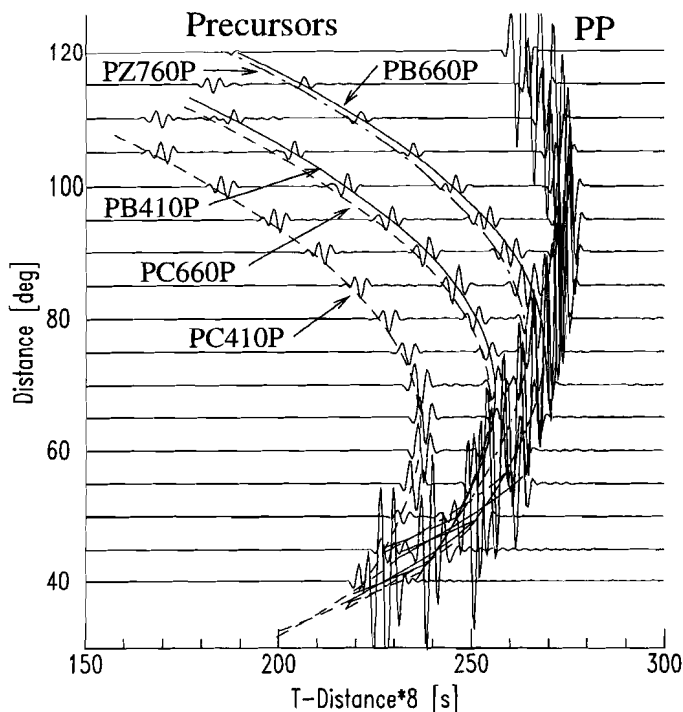


Figure 5.10. Synthetic record sections for asymmetrically reflected precursors to PP at frequencies smaller than 0.6 Hz. Only geometrical rays turning between 250 km depth and the core mantle boundary are considered.

frequency are abruptly truncated. In the previous section we have shown that the amplitude as a function of distance is discontinuous at Bd and Cd . Consequently, including ray geometrical BC -branches may change the amplitudes but not the resemblance with ‘cut-off’ arrivals. In nature this happens more smoothly and our approach needs to be adapted to describe this properly.

Figure 5.10 shows the record section we obtained for PP and its precursors. For SS and its precursors (not shown) a similar record section is obtained. The dashed travel time curve corresponds to the Cd and the solid travel time curve to the Bd contributions. The dashed-dotted travel time curve shows the arrival times of the precursors which are caused by the gradient change at 760 km ($Z760$). Note that the contributions of the different Bd , Cd , and Zd points can interfere.

In chapter 4 we introduced a terminology to name these asymmetrically reflected precursors. Thereafter $PB410P$ labels a P arrival which is generated by a P -wave which corresponds to the $B410$ point. Similarly $SZ760S$ is the S arrival which corresponds to the

Z760 point. Slowness and travel time of these asymmetrically reflected precursors explain remarkably well the observations (see chapter 4 for details).

In the record sections of chapter 4 it is shown that the *B*-point arrivals (*PB410P*, *PB660P*, *SB410S*, and *SB660S*) have amplitudes which are larger than the amplitudes of the *C*-point arrivals (*PC410P*, *PC660P*, *SC410S*, and *SC660S*). This observation suggests that the amplitude fluctuations are stronger at the *B*-points than at the *C*-points. This can be explained by the presence of precritical reflections and head waves with critical points which coincide with the *C*-points and which taper the amplitude (and phase) fluctuations. Note that our synthetics do not incorporate the total wave field. This explains why the *C*-point arrivals are not weaker than the *B*-point arrivals in the synthetics of Figure 5.10.

5.3 Discussion

In chapter 4 it is shown that the asymmetrically reflected *PP* and *SS* precursors are consistently well predicted with travel time and slowness for phases which are generated at the travel time reversals of the triplications for the 410-km and 660-km discontinuities. The corresponding generation mechanism which is explained in the previous sections does not require lateral heterogeneities. This explains the observed ubiquity and coherency for recordings from different azimuths and regions (chapter 4).

We applied a Kirchhoff-Helmholtz related theory after *Frazer and Sen* [1985] and *Frazer* [1987] in a simple and comprehensible fashion which enabled us to understand the principles of the generation of asymmetrically reflected precursors. However, our approach is not suited for quantitative statements since it suffers from two main problems: the frequency independent ray amplitudes and the omission of reflected waves and head waves. Consequently, we have to keep in mind that amplitudes and waveforms of the synthetics will change when these wave phenomena are correctly modeled.

5.3.1 Frequency-Dependent Amplitude Functions and Omitted Reflections

Ray theory is not valid at caustics and critical points. We avoid them by considering upper mantle discontinuities (Figures 5.3c and d) which do not lead to caustics and by omitting the reflected wave field. Finite frequencies lead to smooth amplitude curves in the vicinity of caustics and critical points (*Červený and Zahradník*, 1972). Consequently, our success in predicting the phases seems to be caused by the long wavelength of the oscillating phase functions at finite frequencies (see Figure 5.6b). Note that for instance at 0.05 Hz (period of 20 s) the wavelength of the phase function (Figure 5.6b) is approximately 10^9 which is in the order of the distance between the geometrical positions of the *Bd*- and *Cd*-points. In other words the observation of asymmetrical precursors at finite frequencies suggests that the amplitude functions from the triplications are not smooth enough to achieve destructive

interference far away from the PP (SS) geometrical reflection points. This roughness is probably increased by the fact that the maximum amplitudes connected with the left reversal (Cd) of the travel time curve and the right reversal (Bd) move towards each other for decreasing frequencies (Červený and Zahradník, 1972). Besides frequency dependent amplitude fluctuations, frequency dependent phase fluctuations occur due to the critically reflected phases from the BC -branches.

5.3.2 Amplitudes of B- and C-Point Phases

Head wave amplitudes decrease with increasing distance and are at large distance proportional to $(\text{epicentral distance})^{-2}$ (Brekhovskikh, 1980). Their effect on the PP (SS) waveform are expected to be negligible. However, reflections and head waves at the discontinuity have their critical distance which corresponds to the C -points in the travel time curve. We expect that they smoothen the fluctuations at the C -points which decrease the amplitudes of the corresponding C -point arrivals. Conversely, the travel time at the B -points becomes extremal (maximal), since there is no geometrical phase which emerges at point B . The phase functions, however, are discontinuous in the ray geometrical approach due to the phase shift of $\frac{\pi}{2}$ for the critically reflected arrivals on the BC -branch. Consequently, phase and amplitude fluctuations occur at the B -points and can not be smoothed by the presence of other phases. It is shown by Hill [1974] that the phase difference of $\frac{\pi}{2}$ decreases towards zero with decreasing frequency. In nature at finite frequencies one might expect that the discontinuous phase change is realized by a continuous phase change. In such situation the phase becomes stationary which further increases the B -point phases by constructive interference. This also implies that the B -point phases are mini-max phases: maximum due to contributions in the source receiver direction and minimum in the direction perpendicular to that. We did not perform a waveform analysis, however in chapter 4 it is shown that the slowness and travel time of the large amplitude precursors to PP and SS correspond to the predicted B -point arrivals. C -point phases, when observed, have small amplitudes compared to the B -point phases.

5.3.3 Influence of Heterogeneities

Inherent to our approach we can not prove that a 1-D Earth is indeed sufficient to explain the observed precursor amplitudes. The presence of heterogeneities (for instance surface topography or varying thickness of the crust) will reshape the amplitude functions. This could lead to locally rough amplitude functions, especially close to the points of travel time reversals, and would thus increase these asymmetrical precursors.

Note that we can distinguish between heterogeneities which themselves can cause strong amplitude fluctuations and heterogeneities which mostly modify the surface position of non-stationary points which are caused by the 1-D Earth structure. For instance variations in

depth and thickness of the 410-km discontinuity will change the frequency dependent position and amplitude fluctuation of the *B410*- and *C410*-point. This causes a complicated travel time and amplitude function with non-stationary points which are not anymore arranged along smooth circular shaped curves around source and station at the Earth's surface (see Figure 5.9 as example without lateral heterogeneities). These irregularities will lead to contributions with different travel times. The corresponding arrivals interfere with those from other discontinuities and build up a more complicated precursory wave train. In this case the generation is still dominated by the depth-dependent velocity structure. Conversely lateral heterogeneities at the bounce points can generate precursors by increasing the amplitude fluctuations. Such heterogeneities could also scatter the wave field to the receiver. However, correlation lengths of about 10 km such as proposed by *Cleary et al.* [1975] and *King et al.* [1975] to explain the high frequency precursors are too small to scatter the low frequency wave field. Thus different types of heterogeneities can cause similarly complicated precursory wave trains.

The global character of our observations suggest that the generation by a radially symmetric (1-D) velocity profile provides at least a strong contribution to the *PP* (*SS*) precursors. This is further supported by the consistent observation of strong *B*-point phases for *PP* and *SS*. If the precursors are more dominantly generated by the heterogeneities of the Earth then we would expect to observe more intermittent *B*- and *C*-point phases, i.e. we should also observe weak *B*- and strong *C*-point arrivals. However, this is not inferred from our record sections in chapter 4. Surely the precursors are influenced by heterogeneities and further investigation is required to separate their contributions from those of a 1-D Earth structure. This is an important issue since a complex coda might be interpreted in terms of lateral heterogeneities whereas it could also support our notion that these asymmetrically reflected precursors are fundamental contributors to *PP* and *SS* precursory wave trains.

5.3.4 760-km Discontinuity?

Many Earth models show a steep velocity gradient layer (about 100 km thick) immediately below the 660-km discontinuity. PREM (*Dziewonski and Anderson*, 1981) and ak135 (*Kennett et al.*, 1995) are examples of 1-D Earth models which contain such velocity gradient layer. *Shearer* [1996] shows evidence for such a steep velocity gradient by fitting *S660S* waveform data. The steep velocity gradient below 660 km depth is possibly explained by the gradual transformation of garnet into perovskite near the base of the transition zone which would extend over several tens of kilometers (*Jeanloz and Thompson*, 1983; *Vacher et al.*, 1997). Such a change in velocity gradient causes a strong amplitude fluctuation (Figures 5.8 and 5.9) and should lead to strong precursors. In principle we could investigate these *PZ760P* and *SZ760S* phases to constrain presence or nature of such gradual transformation. However, we can not give a seismological evidence for the presence or absence of this discontinuity since *PB660P* (*SB660S*) and *PZ760P* (*SZ760S*) arrive with similar travel time.

If the 660-km discontinuity consists only of a discontinuity in the Lamé parameter μ as suggested by *Estabrook and Kind* [1996] then *PB660P* would be weakened. For this situation we might be able to conclude that we observe *PZ760P*.

5.4 Conclusions

We show that asymmetrically reflected precursors to *PP* and *SS* are related to the abrupt changes in velocity or velocity gradient in the upper mantle. These discontinuities cause strong amplitude and phase fluctuations of the wave field which as consequence can generate non-geometrically (or non-stationary) phases whenever the wave field interacts with a discontinuity. The proposed generation mechanism correctly predicts the travel time and slowness of the globally observed asymmetrically reflected *PP* and *SS* precursors. It also accounts for the observation of relative strong amplitude *B*-point and weak *C*-point phases. Furthermore, the generation by the depth dependent Earth's structure explains the observed ubiquity and coherence. It also implies that this generation mechanism is a fundamental contributor to the *PP* and *SS* precursors. Lateral heterogeneities might similarly contribute to the precursory wave trains but we expect their nature to be less coherent in amplitude, travel time and waveform. Our more qualitative approach permits no decision about whether a 1-D medium is indeed sufficient to explain the observable amplitudes. However, the observations clearly suggest that the generation by a 1-D Earth provides at least a strong contribution. A different approach should be used for more quantitative investigations. If heterogeneities need to be incorporated then the interpretation of the precursors in order to constrain the heterogeneities becomes highly non-unique.

Appendix

Kirchhoff-Helmholtz Reflection Seismograms and Choice of Integration Surface

The Kirchhoff-Helmholtz theory has been introduced by Helmholtz and Kirchhoff at the end of the 19th-century to solve wave propagation problems. Since then their theory has been applied to many problems and is treated in several text books. The purpose of this appendix is to show some aspects of this theory which are related to our application in chapter 5. First we discuss the Kirchhoff-Helmholtz theory in connection with the applied method to calculate synthetic seismograms and then we focus on the choice of the integration surface in Kirchhoff-Helmholtz related theories.

The Kirchhoff-Helmholtz integral is based on Green's theorem and obtained with the time domain wave equation (e.g. *Aki and Richards*, 1980) or the Helmholtz equation (e.g. *Jackson*, 1975; *Frazer and Sen*, 1985) which is the wave equation in the frequency domain. A general version of the Kirchhoff-Helmholtz integral for a scalar field $\psi(\mathbf{x}_r)$ which satisfies the scalar Helmholtz equation inside a volume V with surface ∂V and normal $\hat{\mathbf{n}}$ is given in equation (A.1) (e.g. *Jackson*, 1975)

$$\psi(\mathbf{x}_r) = \oint_{\partial V} [\psi(\mathbf{x})\hat{\mathbf{n}} \cdot \nabla G(\mathbf{x}_r, \mathbf{x}) - G(\mathbf{x}_r, \mathbf{x})\hat{\mathbf{n}} \cdot \nabla \psi(\mathbf{x})] dS \quad (\text{A.1})$$

$G(\mathbf{x}_r, \mathbf{x})$ is the Green's function which is a solution of the wave equation for the medium inside the volume for a point source at \mathbf{x}_r and \mathbf{x} on the surface ∂V . The equation (A.1) is derived without approximations and tells us that the field $\psi(\mathbf{x}_r)$ within the volume V is completely determined by a combination of the field $\psi(\mathbf{x})$ and its normal derivative $\hat{\mathbf{n}} \cdot \nabla \psi(\mathbf{x})$ on the surface ∂V . The sources of the field $\psi(\mathbf{x})$ are outside the volume V . Note that we are free in choosing the volume, i.e. the integration surface, as long as the field ψ is defined in its interior. We are also free in the choice of the boundary conditions for the Green's function on the integration surface. This permits different representations of equation (A.1) which describe the same situation.

Similar to equation (A.1) *Frazer and Sen* [1985] present a Kirchhoff-Helmholtz integral for elastic waves (their eq. 5):

$$\hat{\mathbf{a}}_2 \cdot \mathbf{u}_1(\mathbf{x}_2) = \oint_{\partial V} \hat{\mathbf{n}} \cdot (\boldsymbol{\tau}_1 \cdot \mathbf{u}_2 - \boldsymbol{\tau}_2 \cdot \mathbf{u}_1) dS \quad (\text{A.2})$$

$\mathbf{u}_1(\mathbf{x}_2)$ is the displacement vector at the receiver position for motion which is measured in the direction $\hat{\mathbf{a}}_2$. ∂V is the surface of a closed volume which contains the receiver position \mathbf{x}_2 in its interior. $\boldsymbol{\tau}_1, \mathbf{u}_1$ are the stress tensor and displacement vector due to the

source which is outside the volume V and τ_2 , and \mathbf{u}_2 are the stress tensor and displacement vector due to a fictitious source within V at the receiver position \mathbf{x}_2 , respectively. This equation is exact and is, similar as equation (A.1), a theoretical expression of Huygens' principle. The wave field generates Huygens' secondary sources on an integration surface which completely determines the wave field at any point inside the volume enclosed by the chosen integration surface.

In order to apply Huygens' principle an infinite number of secondary sources distributed over the whole medium must be used. Since energy propagates along trajectories which follow Fermat's principle the wave propagation can be approximated by ray theory as long as ray theory is valid. Kirchoff-Helmholtz-related methods often connect ray theory and Huygens' elementary waves which are allowed to be generated on one or more surfaces. *Frazer and Sen* [1985] use geometrical optics to approximate the wave propagation between real or fictitious source and integration surface to derive a theory for Kirchoff-Helmholtz reflection seismograms. The use of geometrical optics and plane wave reflection coefficients enable a simplification of equation (A.2) to an equation of the form:

$$\mathbf{u}_1(\mathbf{x}_2, \omega) = i\omega \int_{\Sigma(\mathbf{x})} \mathbf{u}_1(\mathbf{x}) \cdot \mathbf{R}_{12} \cdot \mathbf{u}_2(\mathbf{x}) d\Sigma(\mathbf{x}) \quad (\text{A.3})$$

(after eq. 30 in *Frazer and Sen* [1985] and separation of $i\omega$ from their \mathbf{R}_{12}). The closed surface integration is replaced by the integration over a surface $\Sigma(\mathbf{x})$ which usually is chosen to coincide with a material discontinuity. This is justified when one assumes that the surface $\Sigma(\mathbf{x})$ is closed at large distances where the contributions to the integration are negligible. \mathbf{u}_1 and \mathbf{u}_2 on the right hand side of equation (A.3) describe the geometrical waves from the source and the receiver position to the surface $\Sigma(\mathbf{x})$. They contain the ray amplitude and travel time and are connected at $\Sigma(\mathbf{x})$ by the interaction term \mathbf{R}_{12} . This interaction term incorporates plane wave reflection or transmission coefficients. ω is the circular frequency and acts as a filter. In the time domain $i\omega\mathbf{u}$ translates to the time derivative $\partial\mathbf{u}/\partial t$ which means one has to know the time derivative of the field at the surface.

Equation (A.3) is used to calculate synthetic reflection seismograms. Rays need to be traced to and from the surface $\Sigma(\mathbf{x})$. However, inherent to this approximation non-geometrical phenomena such as the illumination of shadows by diffracted waves can only be studied when the position of this integration surface is correctly chosen. Figure A.1 shows an example where this surface can not take an arbitrary position. A spatially limited reflector causes edge diffractions which illuminate the geometrical shadow. The dashed line marks the surface of integration. In Figure A.1a the diffraction point (edge of the reflector) coincides with a secondary Huygens' source on the surface. In Figure A.1b it does not. For both configurations a diffracted arrival (solid ray in Figure A.1) will be found. However only the first configuration describes the true nature. The non-stationary arrivals proposed in chapter 5 belong to the non-geometrical phenomena and similarly require the correct choice for the integration surface in this ray geometrical Kirchoff-Helmholtz approach.

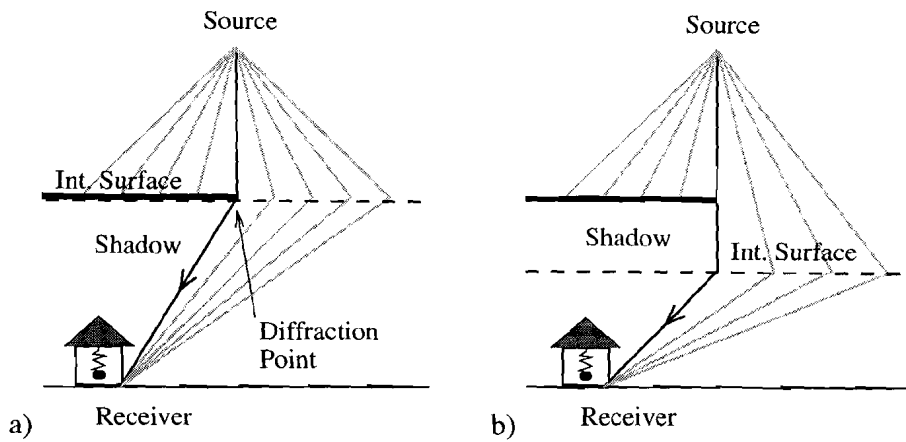


Figure A.1. Representation of an edge diffraction at a spatially limited reflector with a Kirchoff-Helmholtz-related method which uses ray theory to propagate waves to and from the integration surface. The dashed line marks the surface of integration. a) Correct position of integration surface. b) Wrong position of integration surface.

References

- Aki, K., and P.G. Richards, Quantitative seismology, Vol. 1, W.H. Freeman and Co., San Francisco, 1980.
- Bataille, K., R.S. Wu, and S.M. Flatte, Inhomogeneities near the core-mantle boundary evidenced from scattered waves: a review, *Pure Appl. Geophys.*, 132, 151-173, 1990.
- Benz, H.M., and J.E. Vidale, Sharpness of upper-mantle discontinuities determined from high-frequency reflections, *Nature*, 365, 147-150, 1993.
- Bina, C.R., and G. Helffrich, Phase transition Clapeyron slopes and transition zone seismic discontinuity topography, *J. Geophys. Res.*, 99, 15,853-15,860, 1994.
- Bleistein, N., Mathematical methods for wave phenomena, Academic Press, Orlando, 1984.
- Bolt, B.A., *PdP* and *PKiKP* waves and diffracted *PcP* waves, *Geophys. J. R. Astron. Soc.*, 20, 367-382, 1970.
- Bolt, B.A., M. O'Neill, and A. Qamar, Seismic waves near 110° : Is structure in core or upper mantle responsible, *Geophys. J. R. Astron. Soc.*, 16, 475-487, 1968.
- Bostock, M.G., A seismic image of the upper mantle beneath the North American craton, *Geophys. Res. Lett.*, 23, 1593-1596, 1996.
- Bracewell, R.N., The Fourier transform and its applications: New York, McGraw-Hill Book Co., Inc., 268-271, 1965.
- Brekhovskikh, L.M., Applied mathematics and mechanics: Waves in layered media, Academic Press, New York, 1980.
- Bullen, K.E., An Earth model based on a compressibility pressure hypothesis and the Earth's interior, *Mon. Not. R. Astron. Soc. Geophys. Suppl.*, 6, 50-59, 1950.
- Bullen, K.E., and B.A. Bolt, An introduction to the theory of seismology, Cambridge University Press, Fourth Edition, 1985.
- Červený, V., The amplitude-distance curves for waves reflected at a plane interface for different frequency ranges, *Geophys. J. R. Astron. Soc.*, 13, 187-196, 1967.
- Červený, V., and J. Zahradník, Amplitude-distance curves of seismic body waves in the neighbourhood of critical points and caustics - a comparison, *Z. Geophys.*, 38, 499-516, 1972.
- Chapman, C.H., On the computation of seismic ray travel times and amplitudes, *Bull. Seismol. Soc. Am.*, 61, 1267-1274, 1971.
- Cleary, J.R., D.W. King, and R.A.W. Haddon, *P*-wave scattering in the Earth's crust and upper mantle, *Geophys. J. R. Astron. Soc.* 43, 861-872, 1975.
- Cormier, V.F., Some problems with *S*, *SKS* and *ScS* observations and implications for the structure of the base of the mantle and the outer core, *J. Geophys.*, 57, 14-22, 1985.
- Creager, K.C., and T.H. Jordan, Slab penetration into the lower mantle beneath the Mariana and other island arcs of the Northwest Pacific, *J. Geophys. Res.*, 91, 3573-3589, 1986.

- Doornbos, D.J., and N.J. Vlaar, Regions of seismic wave scattering in the Earth's mantle and precursors to PKP, *Nature Phys. Sci.*, *243*, 58-61, 1973.
- Doornbos, D.J., and J.C. Mondt, *P* and *S* waves diffracted around the core and the velocity structure at the base of the mantle, *Geophys. J. R. Astron. Soc.*, *57*, 381-395, 1979.
- Doornbos, D.J., S. Spiliopoulos and F.D. Stacey, Seismological properties of D'' and the structure of a thermal boundary layer, *Phys. Earth Planet. Inter.*, *41*, 225-239, 1986.
- Dziewonski, A.M., Mapping the lower mantle: Determination of lateral heterogeneity in *P* velocity up to degree and order 6, *J. Geophys. Res.*, *89*, 5929-5952, 1984.
- Dziewonski, A.M., and D.L. Anderson, Preliminary reference Earth model, *Phys. Earth Planet. Inter.*, *25*, 297-356, 1981.
- Estabrook, C.H., and R. Kind, The nature of the 660-km upper mantle seismic discontinuity from precursors to *PP*, *submitted to Science*, 1996.
- Frazer, L.N., Synthetic seismograms using multifold path integrals - 1. Theory, *Geophys. J. R. Astron. Soc.*, *88*, 621-646, 1987.
- Frazer, L.N., and M.K. Sen, Kirchhoff-Helmholtz reflection seismograms in a laterally inhomogeneous multi-layered elastic medium - 1. Theory, *Geophys. J. R. Astron. Soc.*, *80*, 121-147, 1985.
- Gaherty, J.B., and T. Lay, Investigation of laterally heterogeneous shear velocity structure in D'' beneath Eurasia, *J. Geophys. Res.*, *97*, 417-436, 1992.
- Garnero, E., D. Helmberger, and S.P. Grand, Preliminary evidence for a lower mantle shear wave velocity discontinuity beneath the central Pacific, *Phys. Earth Planet. Inter.*, *79*, 335-347, 1993.
- Gelchinsky, B., E. Landa, and V. Shtivelman, Algorithms of phase and group correlation, *Geophys.*, *50*, 596-608, 1985.
- Gubbins, D., Core-mantle interactions, *Tectonophysics*, *187*, 385-391, 1991.
- Gubbins, D., Portable broadband seismology: results from an experiment in New Zealand, *Seismic modelling of Earth structure*, E. Boschi, G. Ekström, and A. Morelli (eds.), Editrice Compositori, 305-398, 1996.
- Haddon, R.A.W., and G.G.R. Buchbinder, *S* wave scattering by 3-D heterogeneities at the base of the mantle, *Geophys. Res. Lett.*, *14*, 891-894, 1987.
- Helffrich, G.R., and C.R. Bina, Frequency dependence of the visibility and depth of mantle seismic discontinuities, *Geophys. Res. Lett.*, *21*, 2613-2616, 1994.
- Helffrich, G.R., and B.J. Wood, 410 km discontinuity sharpness and the form of the $\alpha - \beta$ phase diagram: resolution of apparent seismic contradictions, *Geophys. J. Int.*, *126*, 7-12, 1996.
- Hill, D.P., Phase shift and pulse distortion in body waves due to internal caustics, *Bull. Seismol. Soc. Am.*, *64*, 1733-1742, 1974.
- Husebye, E., and R. Madariaga, The origin of precursors to core waves, *Bull. Seismol. Soc. Am.*, *60*, 939-952, 1970.

- Jackson, J.D., Classical electrodynamics, second edition, John Wiley & Sons, 1975.
- Jeanloz, R., and A.B. Thompson, Phase transitions and mantle discontinuities, *Rev. Geophys. Space Phys.*, 21, 51-74, 1983.
- Kanasewich, E.R., C.D. Hemmings and T. Alpaslan, N-th root stack nonlinear multichannel filter, *Geophys.*, 38, 327-338, 1973.
- Kato, M., and K. Hirahara, Precursory arrivals to PP, *Geophys. J. Int.*, 106, 551-557, 1991.
- Kawakatsu H., and F. Niu., Seismic evidence for a 920-km discontinuity in the mantle, *Nature*, 371, 301-305, 1994.
- Kennett, B.L.N., E.R. Engdahl and R. Buland, Constraints on seismic velocities in the Earth from travel times, *Geophys. J. Int.*, 122, 108-124, 1995.
- Kendall, J.M., and P.M. Shearer, Lateral variations in D" thickness from long-period shear wave data, *J. Geophys. Res.*, 99, 11,575-11,590, 1994.
- Kendall, J.M., and P.G. Silver, Constraints from seismic anisotropy on the nature of the lowermost mantle, *Nature*, 381, 409-412, 1996.
- King, D.W., R.A.W. Haddon, and E.S. Husebye, Precursors to PP, *Phys. Earth Planet. Inter.*, 10, 103-127, 1975.
- Kingma, K.J., R.E. Cohen, R.J. Hemley and H.K. Mao, Transformation of stishovite to a denser phase at lower-mantle pressures, *Nature*, 374, 243-245, 1995.
- Kong, S.M., R.A. Phinney and K. Roy-Chowdhury, A nonlinear signal detector for enhancement of noisy seismic record sections, *Geophys.*, 50, 539-550, 1985.
- Kravtsov, Y.A., Rays and caustics as physical objects, in *Progress in Optics 26*, edited by E. Wolf, pp.229-348, Elsevier Science, New York, 1988.
- Krüger, F., M. Weber, F. Scherbaum and J. Schlittenhardt, Double beam analysis of anomalies in the core-mantle boundary region, *Geophys. Res. Lett.*, 20, 1475-1478, 1993.
- Laske, G. and G. Masters, Constraints on global phase velocity maps from polarization data, *J. Geophys. Res.*, 101, 16,059-16,075, 1996.
- Lay, T., Structure of the core-mantle transition zone: A chemical and thermal boundary layer, *Eos Trans. AGU*, 70, 49, 1989.
- Lay, T., and D. Helmberger, A lower mantle S wave triplication and the shear velocity structure of D", *Geophys. J. R. Astron. Soc.*, 75, 799-837, 1983.
- Lay, T., and C.J. Young, Analysis of seismic SV waves in the core's penumbra, *Geophys. Res. Lett.*, 18, 1373-1376, 1991.
- Loper, D.E., and T. Lay, The core-mantle boundary region, *J. Geophys. Res.*, 100, 6397-6420, 1995.
- Mitchell, B., and D. Helmberger, Shear velocities at the base of the mantle from observations of S and ScS, *J. Geophys. Res.*, 78, 6009-6020, 1973.
- Montagner, J.P., Can seismology tell us anything about convection in the mantle?, *Rev. Geophys.*, 32, 115-137, 1994.

- Muirhead, K.J., Eliminating false alarms when detecting seismic events automatically, *Nature*, 217, 533-534, 1968.
- Nataf, H-C., and S. Houard, Seismic discontinuities at the top of D": A world-wide feature?, *Geophys. Res. Lett.*, 20, 2371-2374, 1993.
- Neele, F., Sharp 400-km discontinuity from short-period *P* reflections, *Geophys. Res. Lett.*, 23, 419-422, 1996.
- Neele, F., and R. Snieder, Are long-period body wave coda caused by lateral inhomogeneity?, *Geophys. J. Int.*, 107, 131-153, 1991.
- Neele, F., and R. Snieder, Topography of the 400 km discontinuity from observations of long period *P400P* phases, *Geophys. J. Int.*, 109, 670-682, 1992.
- Neele F., H. de Regt, and J. VanDecar, Gross errors in discontinuity topography from underside reflection data, *in press*, *Geophys. J. Int.*, 1997.
- Neidell, N.S., and M.T. Taner, Semblance and other coherency measures for multichannel data, *Geophys.*, 36, 482-497, 1971.
- Neuberg, J., and J. Wahr, Detailed investigation of a spot on the core-mantle boundary using digital *PcP* data, *Phys. Earth Planet. Inter.*, 68, 132-143, 1991.
- Nguyen-Hai, Propagation des ondes longitudinales dans le noyau terrestre, *Ann. Géophys.*, 19, 285-346, 1963.
- Nolet, G. Partitioned waveform inversion and 2D structure under the NARS array, *J. Geophys. Res.*, 95, 8499-8512, 1990.
- Nolet, G., S.P. Grand, and B.L.N. Kennett, Seismic heterogeneity in the upper mantle, *J. Geophys. Res.*, 99, 23,753-23,766, 1994.
- Olbertz, D.C., and U. Hansen, Dynamically supported topography at the Earth's surface and the core-mantle-boundary: Influences by a depth-dependent thermal expansivity and a chemical boundary layer, *Flow and creep in the solar system: Observations, Modeling and Theory*, D.B. Stone and S.K. Runcorn (eds.), Kluwer Academic Publishers, 197-206, 1993.
- Paulssen, H., Lateral heterogeneity of Europe's upper mantle as inferred from modelling of broad-band body waves, *Geophys. J. R. Astron. Soc.*, 91, 171-199, 1987.
- Paulssen, H., Evidence for a sharp 670-km discontinuity as inferred from *P* to *S* converted waves, *J. Geophys. Res.*, 93, 10489-10500, 1988.
- Paulssen, H., S. Van der Lee and G. Nolet, The NARS-Netherlands Project, *IRIS Newsletter*, 9 (4), 1-2, 1990.
- Paulssen, H., and E. Stutzmann, On *PP-P* differential travel time measurements, *Geophys. Res. Lett.*, 23, 1833-1836, 1996.
- Petersen, N., J. Gossler, R. Kind, K. Stammler, and L. Vinnik, Precursors to *SS* and structure of transition zone of the North-Western Pacific, *Geophys. Res. Lett.*, 20, 281-284, 1993.
- Poupinet, G., *PL (S)* a 40° et la discontinuité de vitesse de *S* à 850 km de profondeur, *Ann. de Géophys.*, 30, 127-139, 1974.

- Ranalli, G., Seismic tomography and mineral physics, *Seismic modelling of Earth structure*, E. Boschi, G. Ekström, and A. Morelli (eds.), Editrice Compositori, 443-461, 1996.
- Revenaugh, J., and T.H. Jordan, A study of mantle layering beneath the western Pacific, *J. Geophys. Res.*, *94*, 5787-5813, 1989.
- Revenaugh, J., and T.H. Jordan, Mantle layering from ScS Reverberations, 4, The lower mantle and core-mantle boundary,
- Richards, M.A., and C.W. Wicks, Jr, *S-P* conversions from the transition zone beneath Tonga and the nature of the 670 km discontinuity, *Geophys. J. Int.*, *101*, 1-35, 1990.
- Richards, P.G., Seismic waves reflected from velocity gradient anomalies within the Earth upper mantle, *Z. Geophys.*, *38*, 517-527, 1972.
- Rydelek, P.A., and I.S. Sacks, Testing the completeness of earthquake catalogues and the hypothesis of self-similarity, *Nature*, *337*, 251-253, 1989.
- Scherbaum, F., F. Krüger, and M. Weber, Double beam imaging: Mapping lower mantle heterogeneities using combinations of source and receiver arrays, *J. Geophys. Res.*, *102*, 507-522, 1997.
- Schlittenhardt, J., J. Schweitzer, and G. Müller, Evidence against a discontinuity at the top of the D", *Geophys. J. R. Astron. Soc.*, *81*, 295-306, 1985.
- Shearer, P.M., Seismic imaging of upper-mantle structure with new evidence for a 520-km discontinuity, *Nature*, *344*, 121-126, 1990.
- Shearer, P.M., Constraints on upper mantle discontinuities from observations of long-period reflected and converted phases, *J. Geophys. Res.*, *96*, 18147-18182, 1991.
- Shearer, P.M., Transition zone velocity gradients and the 520-km discontinuity, *J. Geophys. Res.*, *101*, 3053-3066, 1996.
- Snieder, R., Surface wave inversions on a regional scale, *Seismic modelling of Earth structure*, E. Boschi, G. Ekström, and A. Morelli (eds.), Editrice Compositori, 149-181, 1996.
- Souriau, A., *P*-coda at distances 80°-120° and structure beneath subduction zones: Example of Chile, *Geophys. Res. Lett.*, *15*, 1479-1482, 1988.
- Stoffa, P.L., P. Buhl, J.B. Diebold and F. Wenzel, Direct mapping of seismic data to the domain of intercept time and ray parameter – A plane-wave decomposition, *Geophys.*, *46*, 255-267, 1981.
- Taner, M.T., and F. Koehler, Velocity spectra-digital derivation and applications of velocity functions, *Geophys.*, *84*, 859-881, 1969.
- Taner, M.T., F. Koehler, and R.E. Sheriff, Complex seismic trace analysis, *Geophys.*, *44*, 1041-1063, 1979.
- Vacher, P., A. Mocquet, and C. Sotin, Computation of seismic profiles from mineral physics: The importance of the non olivine components for explaining the 660 km depth discontinuity, *Phys. Earth Planet. Inter.*, *accepted*, 1997.

- Van der Hilst, R.D., Complex morphology of subducted lithosphere in the mantle beneath the Tonga trench, *Nature*, 374, 154-157, 1995.
- Van der Hilst, R.D., E.R. Engdahl, W. Spakman, G. Nolet, Tomographic imaging of subducted lithosphere below northwest Pacific island arcs, *Nature*, 353, 37-43, 1991.
- Van der Lee, S., H. Paulssen, and G. Nolet, Variability of *P660s* phases as a consequence of topography of the 660 km discontinuity, *Phys. Earth Planet. Inter.*, 86, 147-164, 1994.
- Wajeman, N., Detection of underside *P* reflections at mantle discontinuities by stacking broadband data, *Geophys. Res. Lett.*, 15, 669-672, 1988.
- Ward, S.N., Long-period reflected and converted upper-mantle phases, *Bull. Seismol. Soc. Am.*, 68, 133-153, 1978.
- Weber, M., *P* and *S* wave reflections from anomalies in the lowermost mantle, *Geophys. J. Int.*, 115, 183-210, 1993.
- Weber, M., and J.P. Davis, Evidence for a laterally variable lower structure from *P*- and *S*-waves, *Geophys. J. Int.*, 102, 231-255, 1990.
- Weber, M., and C.W. Wicks, Reflections from a distant subduction zone, *Geophys. Res. Lett.*, 23, 1453-1456, 1996.
- Weichert, D.H., Reduced false alarm rates in seismic array detection by non-linear beamforming, *Geophys. Res. Lett.*, 2, 121-123, 1975.
- Wielandt, E., Propagation and structural interpretation of non-plane waves, *Geophys. J. Int.*, 113, 45-53, 1993.
- Woodhouse, J.H., H.J. van Heijst, and J. Trampert, Mantle modelling using surface wave overtone measurements and other data sets, abstract, *EOS*, 77, 482, 1996.
- Wright, C., Array studies of seismic waves arriving between *P* and *PP* in the distance range 90° to 115°, *Bull. Seismol. Soc. Am.*, 62, 385-400, 1972.
- Wright, C., and K.J. Muirhead, Longitudinal waves from the Novaya Zemlya nuclear explosion of October 27, 1966, recorded at the Warramunga seismic array, *J. Geophys. Res.*, 74, 2034-2048, 1969.
- Wright, C., K.J. Muirhead, and A.E. Dixon, The *P* wave velocity structure near the base of the mantle, *J. Geophys. Res.*, 90, 623-634, 1985.
- Wyssession, M.E., Continents of the core, *Nature*, 381, 373-374, 1996.
- Wyssession, M.E., L. Bartko, and J. Wilson, Mapping the lowermost mantle using core-reflected shear waves, *J. Geophys. Res.*, 99, 13,667-13,684, 1994.
- Young, C.J., and T. Lay, The core-mantle boundary, *Annu. Rev. Earth Planet. Sci.*, 15, 25-46, 1987.
- Young, C.J., and T. Lay, Multiple phase analysis of the shear velocity structure in the D'' region beneath Alaska, *J. Geophys. Res.*, 95, 17,385-17,402, 1990.
- Zürn, W. and P.A. Rydelek, Revisiting the phasor-walkout method for detailed investigation of harmonic signals in time series, *Surv. Geophys.*, 15, 409-431, 1994.

Summary in English

This thesis intends to advance our understanding of secondary broad band body wave arrivals caused by mantle structure, the wave propagation phenomena behind them, and the corresponding constraints on Earth structure. These items are intimately related to each other and their understanding promises to increase the constraints and resolution of the fine structure of the Earth.

The research of this thesis is presented in four chapters and comprises evidence of steeply reflected and focused arrivals from the D" region, a new coherency measure and stacking technique to detect weak but coherent signals, and the observation and explanation of non-geometrical *PP* and *SS* precursors caused by amplitude and phase fluctuations in the wave field.

In chapter 2 of this thesis we present evidence for precursors to the *ScS* and *sScS* phases observed at epicentral distances smaller than 30° . The coherency, frequency dependence, slowness, polarity, polarization, intermittency and the occasionally large amplitudes of the precursors are discussed for a subsidiary data set from a station in New Zealand. Many explanations can be rejected and we conclude that a reflector with topography 180 km above the core-mantle boundary underneath the Kermadec-Tonga region causes these precursors. We test the possibility of focusing and calculate synthetic seismograms based on a three-dimensional Kirchhoff-Helmholtz related theory. We can constrain the topography scale lengths and amplitudes to be about 1200-1600 km and 30-50 km, respectively. The frequency dependent character of the data can be explained by the frequency dependent size of the focusing zone, the frequency dependent sampling of the structure and/or the frequency dependent reflection coefficient. Inherent to these ambiguities we refrain from presenting the "best" model. The limited data set permits no conclusions about the global properties of this discontinuity.

The work of chapter 3 is motivated by the often ambiguous detection of weak but coherent arrivals in ordinary, linear data stacks. We present a new coherency measure and stacking technique which are based on complex trace analysis. An amplitude unbiased coherency measure is designed based on the instantaneous phase which is used to weight the samples of the linear stack. This procedure cleans the linear stack from incoherent noise. The result is called phase weighted stack (PWS) and can easily be extended to be applied in different environments. Synthetic and real data are used to compare the proposed technique with other measures that are often used. The amplitude unbiased coherency measure is clearly superior to the other measures when phase coherent signals with varying amplitudes are to be detected. PWS enables the identification of weak mantle conversions which have not been detected in linear stacks. As another merit, the travel time and slowness may be measured more accurately.

In chapters 4 and 5 a study of the characteristics and generation of asymmetrically reflected precursors to *PP* and *SS* is presented. They are observed at epicentral distances ranging between 80° and 120° . These precursors have travel time and slowness values which constrain their ray path to have bounce points at about 15° to 30° distance from the receiver or source. Asymmetrically reflected *PP* precursors have been known for more than 30 years and have led to different explanations. Chapter 4 presents also *SS* precursors and shows that *PP* and *SS* precursors have the same characteristics. They are related to each other by the same generation mechanism. Especially their coherency and ubiquity can not be explained by the previously proposed generation mechanisms. It is further shown that the measured slowness and travel time is well explained by waves which are generated at the Earth's surface for points which correspond to the travel time reversals of the upper mantle triplications. A new mechanism which can explain the observations is proposed in chapter 5. Its principles are stepwise pictured with the help of Huygens' principle. The strong changes in velocity and velocity gradient in the upper mantle cause triplications and strong amplitude fluctuations of the wave field at the Earth's surface. The precursors are caused by these strong amplitude fluctuations and resemble those of edge and point diffracted waves. If the fluctuations are strong enough no lateral heterogeneities are required. This can explain the ubiquity and coherency shown in chapter 4. Synthetic seismograms are calculated, however, inherent to applied simplifications we can not exclude whether lateral heterogeneities are required to strengthen the precursors to explain the observed amplitudes.

Within 4 chapters of this thesis are studies presented on secondary body wave arrivals. It is shown that these phases are not at all secondary in the sense that they carry very useful information about the fine structure of the Earth. Only due to the variability in their appearance in seismograms are they still difficult to handle especially in routinely used processing and inversion schemes. It is a challenge to better detect these observable features, to understand the cause of these wave phenomena and to better constrain the Earth's structure.

Summary in Dutch (Samenvatting in het Nederlands)

De fijne structuur van de aarde veroorzaakt verschillende golfvoortplantingsfenomenen die men meestal als secundaire ruimtegolfsignalen in seismogrammen waarneemt. Veel van deze signalen worden nog steeds niet begrepen hoewel ze waardevolle informatie bevatten over de structuur van de aarde. Het doel van dit proefschrift is het vergroten van het begrip van deze signalen en de golfvoortplantingsfenomenen, om hiermee meer inzicht te krijgen in de structuur van de mantel. Het in dit proefschrift behandelde onderzoek wordt in vier hoofdstukken uiteengezet. Het behandelt steil gereflecteerde en gefocuseerde signalen van de D"-laag, een nieuwe 'stacking' techniek met coherentiebepaling om zwakke maar coherente signalen waar te nemen, en de waarneming en verklaring van niet-geometrische *PP*- en *SS*-voorlopers veroorzaakt door amplitude- en fasefluctuaties in het golfveld.

In het tweede hoofdstuk van dit proefschrift wordt het bestaan van voorlopers van de *ScS* en de *sScS* fases, die worden waargenomen bij epicentrale afstanden kleiner dan 30° , behandeld. De coherentie, frequentie-afhankelijkheid, 'slowness', polariteit, polarisatie, het inconsistent voorkomen, en de soms hoge amplitudes van deze voorlopers worden besproken voor een dataset van een meetstation in Nieuw-Zeeland. Vele gangbare verklaringen voor de besproken fenomenen kunnen verworpen worden. Er wordt vastgesteld dat een reflector die zich 180 km boven de kernmantelgrens bevindt onder het Kermadec-Tonga gebied deze voorlopers veroorzaakt. De mogelijkheid van focusering wordt getest en de synthetische seismogrammen, gebaseerd op een driedimensionale Kirchhoff-Helmholtz-gerelateerde theorie, worden berekend. De lengteschaal van de topografie wordt bepaald op 1200-1600 km en de bijbehorende amplitude op 30-50 km. Het frequentie-afhankelijke karakter van de data kan verklaard worden door de frequentie-afhankelijke grootte van het brandpunt, de frequentie-afhankelijke bemonstering van de structuur en/of de frequentie-afhankelijke reflectiecoëfficiënt. Vanwege gebrek aan een eenduidige verklaring zal er niet een 'beste' model gepresenteerd worden. Het is tevens niet mogelijk uitspraken te doen over deze discontinuïteit op een globale schaal vanwege het beperkte karakter van de dataset.

Het werk van hoofdstuk 3 is gemotiveerd door de vaak onzekere waarneming van zwakke, maar coherente signalen in gewone, lineaire data 'stacks'. Er wordt een nieuwe methode ter bepaling van de coherentie besproken en een bijbehorende 'stacking' techniek gebruikmakend van tijdreeksanalyse in het complexe domein. Er is een maat ontwikkeld voor de coherentie die gebaseerd is op de instantane fase, en die onafhankelijk is van de amplitude. Deze wordt gebruikt om de datapunten van de lineaire 'stack' te wegen. Deze procedure verwijdert ongecorrleerde ruis uit de lineaire stack. Het resultaat wordt 'phase weighted stack' (PWS) genoemd en de methode kan eenvoudig uitgebreid worden voor toepassingen in andere omgevingen. Zowel synthetische als bestaande data worden gebruikt om de voorgestelde techniek te vergelijken met andere vaak gebruikte technieken. Het blijkt dat de amplitude-onafhankelijke coherentie maat duidelijk superieur

is ten opzichte van andere maatstaven wanneer fase-coherente signalen met afwisselende amplitudes waargenomen worden. De PWS-methode maakt de identificatie mogelijk van zwakke mantelconversies die niet waargenomen zijn in de lineaire 'stacks'. Een ander voordeel van de methode is dat de looptijd en 'slowness' nauwkeuriger gemeten kunnen worden.

In hoofdstuk 4 en 5 wordt een studie van de karakteristieken en het ontstaan van asymmetrisch gereflecteerde voorlopers van *PP* en *SS* fasen besproken. Deze voorlopers zijn waargenomen op epicentrale afstanden die variëren van 80° tot 120° , en de looptijd- en 'slowness'-waarden bepalen dat hun stralenpaden reflectiepunten moeten hebben op een afstand van 15° tot 30° van de bron of ontvanger. Asymmetrisch gereflecteerde *PP*-voorlopers zijn al meer dan 30 jaar bekend en er zijn verschillende verklaringen voor. In hoofdstuk 4 worden ook *SS*-voorlopers besproken, en het blijkt dat *PP*- en *SS*-voorlopers dezelfde karakteristieken hebben. Ze zijn aan elkaar gerelateerd door hetzelfde ontstaansmechanisme. Vooral de coherentie en veelvuldige waarneming kan niet verklaard worden door de gangbare ideeën. Verder wordt aangetoond dat de gemeten 'slowness' en looptijd goed te verklaren zijn door golven die ontstaan aan het aardoppervlak op punten die overeenkomen met de looptijdkeerpunten van de bovenmantel-triplicaties. In hoofdstuk 5 wordt een nieuw mechanisme voorgesteld dat de waarnemingen kan verklaren. De principes van dit mechanisme worden stapsgewijs beschreven met behulp van het principe van Huygens. De sterke veranderingen in snelheid en snelheidsgradiënt in de bovenmantel veroorzaken triplicaties en sterke amplitudefluctuaties van het golfveld aan het aardoppervlak. Het ontstaan van voorlopers wordt veroorzaakt door deze sterke amplitudefluctuaties en lijken op het ontstaan van hoek- en puntgediffracteerde golven. Wanneer de fluctuaties sterk genoeg zijn, dan zijn er geen laterale heterogeniteiten nodig. Dit kan de veelvuldige waarneming en coherentie uit hoofdstuk 4 verklaren. Synthetische seismogrammen worden berekend. Inherent aan toegepaste simplificaties echter, kan niet uitgesloten worden dat laterale heterogeniteiten nodig zijn om de voorlopers te versterken om de waargenomen amplitudes te verklaren.

In dit proefschrift worden studies besproken van secundaire ruimtegolfsignalen. Het blijkt echter dat deze golfsignalen in het geheel niet secundair zijn voor de informatie die ze verschaffen over de fijnere structuur van de aarde. Louter door de variabiliteit van het voorkomen in seismogrammen zijn ze moeilijk waarneembaar met routinematige verwerkings- en inversieschema's en daardoor als secundair aangeduid. Het is een uitdaging de kenmerken van deze waarneembare voorlopers beter te bepalen, alsmede de fenomenen te begrijpen die de golven veroorzaken om daarmee de kennis van de fijne structuur van de aarde te verbeteren.

Acknowledgements

It was a great privilege and challenge for me to do research at the Geophysics Department in Utrecht. During these four years I learned many new things and gained valuable experience. I would like to express my gratitude to all the people who somehow contributed to this joyful period, unfortunately not all can be mentioned here.

My first thank goes to my parents who have always supported me. I appreciate their great efforts and sacrifices creating an environment that allowed me to do a doctorate.

Special thanks go to my co-promotor Hanneke Paulssen and promotor Roel Snieder. Hanneke Paulssen guided my research and I am very grateful for the way she did it. I appreciate very much the freedom I had while never feeling alone. She taught me a lot and I thank her for her friendship, her continuous support and confidence in my work, her encouraging and valuable discussions, and making readable all my English writing. I am indebted to Roel Snieder for offering me the opportunity to do my PhD in the seismology group, for the trust in me that he expressed even before I started at Utrecht, and for his interest, helpful discussions and support all times.

Further, I would like to acknowledge my colleagues and the staff of the Geophysics Department for their friendship and for the nice working atmosphere. Especially in the beginning I benefited from my colleagues and office mates Dolors Alsina, Harm Dorren, Tijn Passier, Everhard Muzert, and Henk Marquering, all of whom helped me to get integrated into my new working environment. I am grateful to Axel Röhm, Filip Neele, Anthony Lomax, Eléonore Stutzmann, Paul Colin, Jay Pulliam, Laura Jones, Andrew Curtis, Jeannot Trampert, Kabir Roy-Chowdhury, and Ulrich Hansen for lending an ear and for helpful discussions whenever I knocked at their doors. I am thankful to Wim Spakman for placing his computer at my disposal to perform some of the calculations from chapter 5, to Theo van Zessen and Joop Hoofd for their help with computer related problems, and to Bernadine Vet for her assistance with bureaucratic items.

I am grateful for the critical reading and constructive comments on a manuscript over anomalous ScS precursors by Jay Pulliam, Ruedi Widmer, and Walter Zürn. An extended study is presented in chapter 2 and I acknowledge the critical reviews and discussions with Laura Jones, Anthony Lomax, Michael Weber, and the *Journal of Geophysical Research*-referees Christopher Young, Ed Ganero, and Michael Wyssession.

Thanks go also to Bart Overbeck for translating the summary into Dutch. Further, I would like to express my appreciation to Dolors Condom for her extensive searches through *De rerum natura*, *Naturalis historia*, *Tusculanae*, ... and for providing me with a great selection of quotations of famous philosophers of antiquity.

The study presented in this thesis is based on the seismic recordings of many stations around the globe. I am very grateful to the station operators and the staff of IRIS-DMC, GRSN, NARS-NL, GEOSCOPE, and ODC for their efforts to provide easily accessible, high quality data.

Shell and NWO partly supported my attendance at the AGU-meeting in San Francisco (in 1996), and the Mathematical Geophysics Meeting in Santa Fe (in 1996). The rest and my attendance at other meetings were financed by Utrecht University. I benefited from these meetings and greatly acknowledge this financial support. I am also very grateful to Eléonore Stutzmann for inviting me to give a talk at the IPG-Paris and to discuss with the people there. Thanks go also to Marcelo Assumpção. He gave me the opportunity to visit the IAG in São Paulo and to present my results on ScS precursors there.

In the last year I tanked a lot of energy during the *rodas de capoeira* and I am very thankful to the participants for the really wonderful games and great atmosphere.

I am also very grateful to my friends from Karlsruhe and Catalunya for the unfortunately few but great moments which we spend together and moral support from the distance.

Finally, I want to thank Márcia for all her love, understanding, and support. She was always prepared to help and to make sacrifices, and she broadened my horizons and views to many new things.

Pusilla res mundus est, nisi in illo quod quaerat omnis mundus habeat.

Seneca, Naturales questiones VII, 68/69 A.D.

Curriculum Vitae

- September 5th, 1966 Born in Hannover (Germany) as first son of Rosario Bellapart i Franquesa and Erhard Schimmel.
- June 1986 Abitur at the Grotefeld Gymnasium in Hann. Münden, Germany.
- 1986 - 1992 Study of Geophysics at the University Fridericiana of Karlsruhe, Germany.
- 1989 - 1992 Research and field assistant at the Geophys. Institute in Karlsruhe (Germany).
- 1992/93 Temporal field assistant at the Institute of Earth Sciences Jaume Almera (CSIC), Barcelona (Spain).
- 1993 - 1997 Research assistant (AIO) at the Department of Theoretical Geophysics, Utrecht University, The Netherlands.